**Post-CHF Heat Transfer Experiments and Modeling at Subcooled and Low-quality Conditions**

by

Qingqing Liu

A dissertation submitted in partial fulfillment
of the requirements for the degree of
Doctor of Philosophy
(Nuclear Engineering and Radiological Sciences)
in the University of Michigan
2020

Doctoral Committee:

Professor Xiaodong Sun, Chair
Mr. Joseph Kelly, U.S. Nuclear Regulatory Commission
Professor Annalisa Manera
Associate Research Scientist Dr. Victor Petrov
Professor Kevin Pipe

Qingqing Liu

qingqliu@umich.edu

ORCID iD:  0000-0002-0122-1222

## Dedication

*This dissertation is dedicated to my parents and wife who encouraged me to pursue my dreams and finish my dissertation.*

## Acknowledgements

This research was funded by the U.S. Nuclear Regulatory Commission (NRC). I owe a debt of gratitude to many people for the memorable graduate experience. The professional environment facilitates my PhD study and research and encourages my future academic pursuits.

First, I cannot have enough good words to express my deepest gratitude and respect to my advisor, Professor Xiaodong Sun, for his bottomless knowledge and tremendous patience in guiding me all the way through the finish line. He always makes great efforts to advise me on my project and revise reports and papers. I am also very thankful to Professor Richard N. Christensen for his warm-hearted encouragements and brilliant suggestions during my early research at the Ohio State University.

My heartfelt thanks to my committee members: Mr. Joseph Kelly, Professor Annalisa Manera, Dr. Victor Petrov, and Professor Kevin Pipe. My sincere appreciation to Mr. Joseph Kelly for his technical support and guidance for my research. I learn a lot from him about the post-CHF experiments and modeling. Professor Annalisa Manera is very kind to provide lab space for the test facility construction. Dr. Victor Petrov provides invaluable suggestions when I encounter issues and challenges during the test facility construction and helps me with the X-ray radiography system testing. Professor Kevin Pipe provides me with valuable feedback on my research work. In addition, I would like to thank Prof. Martha Matuszak for her comments on my research during

the prospectus exam. It has been a true pleasure and an honor knowing and learning from them and their support has functioned as the cornerstone for me to carry on.

I would like to thank all my friends and colleagues at the University of Michigan and the Ohio State University. I would like to thank my lab mates, Mr. Hanxing Sun, Dr. Shanbin Shi, Dr. Qiuping Lv, Dr. Minghui Chen, Dr. Yang Liu, Dr. Adam Burak, Mr. Sheng Zhang, Mr. Chengqi Wang, Mr. Xiaoqin Zhang, Dr. Xiao Wu, Dr. Hsun-Chia Lin, Dr. David Arcilesi, Dr. Limin Wang, and Mr. Yutaro Umehara. In addition, my sincere thanks and appreciation to Mr. Julio Diaz for helping me test the X-ray radiography system. It brings me a lot of pleasure to work with Mr. Diaz.

Finally, special thanks to my wife, Fanzhe Yang, and my newborn baby, Eric Tong Liu, who stand by me and lift my spirit, and my parents for their continued support and love throughout this period.

## Table of Contents

## List of Figures

## List of Tables

## Nomenclature

| | |
|---|---|
| $A$ | cross-sectional area of a flow channel, $m^2$ |
| $C$ | constant |
| $c_p$ | specific heat capacity at constant pressure, J/kg-K |
| $D$ | hydraulic diameter, m |
| $D_c$ | liquid-core diameter, m |
| $E$ | weld joint efficiency |
| $F$ | interfacial friction factor |
| $G$ | gravitational acceleration, $m/s^2$ |
| $G$ | mass flux, $kg/m^2$-s |
| $h_c$ | convective heat transfer coefficient, $W/m^2$-K |
| $h_t$ | total heat transfer coefficient, $W/m^2$-K |
| $h_{i-l,\infty}$ | heat transfer coefficient from the vapor-liquid interface to the liquid in the fully-developed IAFB regime, $W/m^2$-K |

$h_{i-l}^{*}$ modified heat transfer coefficient at the axial location $z$ from the vapor-liquid interface to the liquid, W/m$^2$-K

$h$ specific enthalpy, kJ/kg

$H'_{fg}$ enthalpy difference between the vapor at its arithmetic average temperature and liquid at the saturation temperature, kJ/kg

$I_0$ source intensity, #/cm$^2$-s

$I(\alpha)$ intensity at void fraction $a$, #/cm$^2$-s

$k$ thermal conductivity, W/m-K

$La$ Laplace number

$\dot{m}$ mass flow rate, kg/s

$N_{sub}$ subcooling number

$Nu$ liquid-side Nusselt number

$p$ pressure, Pa

$P$ perimeter, m

$P_{DC}$ heating power to the test section, W

Pr Prandtl number

$q''$ heat flux, W/m$^2$

$\dot{q}_v$ internal heat source in the test section wall, W/m$^3$

$\dot{Q}_{loss}$ heat losses from the test section to the ambient, W

$\mathrm{Re}$ Reynolds number

$\mathrm{Re}_{\mathrm{i}}$ modified gas Reynolds number

$S$ maximum allowable stress, psi

$t$ time, s

$t_m$ minimum required wall thickness, mm

$T$ temperature, K

$V$ velocity, m/s

$\bar{V}$ area-averaged velocity, m/s

$\mathrm{We}$ Weber number

$x$ flow quality

$\Delta\rho$ density difference between the liquid and vapor, kg/m$^3$

$\Delta T_s$ wall superheat, K

$\Delta T_{sub}$ liquid subcooling, K

*Greek Symbols*

$\alpha$ void fraction

$\Gamma$ vapor generation rate per interfacial area concentration, kg/m$^2$-s

$\Gamma'''$ vapor generation rate per unit volume, kg/m$^3$-s

$\delta$ vapor film thickness, m

$\delta^*$ non-dimensional vapor film thickness

$\varepsilon$ emissivity

$\lambda$ a heat transfer enhancement factor due to disturbances to the vapor-liquid interfaces

$\lambda_c$ critical wavelength of the Taylor-Helmholtz instability

$\lambda_{fv}$ a factor accounting for the interfacial disturbances and turbulence at the vapor-liquid interface

$\mu$ dynamic viscosity, kg/m-s

$\mu_f$ linear attenuation coefficient of water, $cm^{-1}$

$\mu_g$ linear attenuation coefficient of steam, $cm^{-1}$

$\mu_{ins}$ linear attenuation coefficient of thermal insulation, $cm^{-1}$

$\mu_w$ linear attenuation coefficient of a tube wall, $cm^{-1}$

$\rho$ density, $kg/m^3$

$\sigma$ surface tension between the liquid and vapor, $kg/s^2$

$\sigma_\alpha$ standard deviation of void fraction

$\tau$ shear stress, $kg/m\text{-}s^2$

*Subscripts*

c liquid core

| | |
|---|---|
| i | Vapor-liquid interface |
| l | liquid phase |
| li | liquid-side interfacial |
| mix | mixture of vapor and liquid |
| rad | radiation |
| sat | saturation |
| v | vapor phase |
| w | wall surface |
| wv | wall to vapor |

## Abstract

During postulated large break loss of coolant accidents (LB-LOCAs) in a water-cooled nuclear reactor, the reactor is expected to shut down but the fuel cladding temperature would still increase due to the release of the stored energy in the fuel and decay energy of fission products. To prevent the cladding from overheating, the Emergency Core Cooling System will start up to inject makeup water into the reactor core, during which post-critical heat flux (post-CHF) flow regimes could dominate the heat transfer from the cladding to the coolant. The heat transfer characteristics in the post-CHF flow regimes are important for reactor design and safety.

In this research, a Post-CHF Heat Transfer (PCHT) test facility was designed and constructed to perform high-pressure (up to 1,000 psi or 6.8 MPa) post-CHF heat transfer experiments at high mass fluxes (up to 2,000 kg/m$^2$-s) with large inlet subcooling values (up to 50 ºC). A COMSOL multiphysics model was developed to inform the test section design. All the instrumentation in the test facility to measure the temperature, pressure, pressure differential, flow rate, void fraction, and flow topology have been tested to ensure their functionality. Shakedown tests have been performed in the test facility, including hydrostatic leak test, pressure control test, subcooled boiling test, hot patch test, gamma densitometer test, and X-ray radiography system test.

Reflooding and dry patch tests have been performed to study the wall heat transfer characteristics in the post-CHF flow regimes. In the reflooding tests, the quench curve indicates that the wall

temperature has a rapid decrease in the quenched region, during which the heat (stored energy) release from the test section plays a significant role in the total wall heat flux to the fluid. Based on the convective heat transfer coefficient profile, it is believed that inverted annular film boiling (IAFB) regime exists right downstream of the quench front. In the dry patch tests, the convective heat transfer coefficient for the dry patches is larger than those calculated by three heat transfer correlations for IAFB in the literature, especially for conditions of relatively low wall superheats, which indicates that the motion of the dry patch along the heated surface enhances the heat transfer.

In addition to the experimental study, some closure models in the two-fluid model for the IAFB regime are benchmarked and improved. A correlation for the liquid-side Nusselt number is developed based on a parametric study performed in this research. A laminar vapor film model and nine existing correlations for the interfacial friction factor are evaluated based on the IAFB experimental data. The comparisons suggest that the interfacial friction factor in the smooth IAFB region is primarily dependent on the gas Reynold number and vapor film thickness and that in the wavy IAFB region, it is dominantly affected by the interfacial waves. To predict the flow regime transition from IAFB to ISFB, a correlation for the critical Weber number is proposed as a function of two non-dimensional parameters, i.e., the Reynolds number and subcooling number.

In summary, this research presents a number of original contributions to the field. The PCHT test facility with its unique test capabilities brings many benefits to the community and can assist in further nuclear reactor safety improvement. The improved post-CHF closure models could be used in reactor system analysis to improve the IAFB modeling.

# Chapter 1 Introduction

## 1.1 Background

During postulated large break loss of coolant accidents (LB-LOCAs) in water-cooled nuclear reactors, the reactor will shut down automatically but the temperature of the fuel cladding will increase rapidly due to the release of the stored heat and fission product decay heat in the fuel rods and insufficient coolant in the reactor core. Figure 1.1 shows a schematic of a LB-LOCA. The water level in the reactor core decreases and the fuel rods are partially uncovered due to the piping break in the cooling system, which causes the fuel rods temperature to increase rapidly. To prevent the reactor core from overheating, the Emergency Core Cooling Systems (ECCS) starts up to inject coolant into the reactor core to reflood the reactor core, during which the post critical heat flux (CHF) flow regimes dominate the heat transfer mechanisms. In the post-CHF flow regimes, vapor instead of liquid covers the heated surface, causing poor heat transfer and high wall temperature due to the low thermal conductivity of vapor. Post-CHF flow regimes can also occur during a loss-of-regulation accident (LORA) when the reactor power accidentally increases and in some other applications, such as cryogenic applications, metallurgical processing, and conventional boilers.

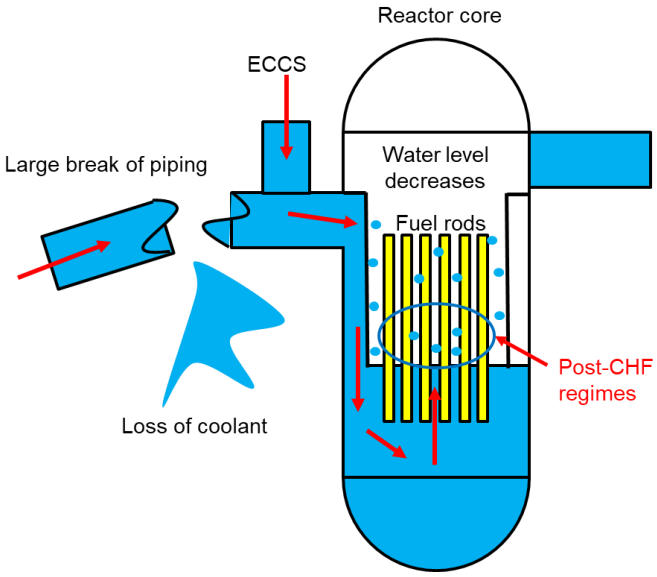


Figure 1.1 Schematic of a LB-LOCA

Due to the high subcooling of the injected water and high fuel cladding temperatures, inverted annular film boiling (IAFB) could occur at the so-called quench front, downstream of which a thin vapor film covers the heated surface (Groeneveld, 1975). In the IAFB regime, a continuous subcooled liquid core is in the central region of the flow channel and is separated by the vapor film from the heated wall. Heat is mainly transferred from the heated surface to the vapor film by heat conduction when the void fraction is low, and the vapor film flow is in laminar flow. A small fraction of the heat goes to superheat the vapor film while the remaining heat crosses the vapor film and reaches the vapor-liquid interface. Because the subcooling of the liquid core is high near the quench front, a small fraction of the heat reaching the interface via convective and radiative heat transfer vaporizes the liquid, while most of the heat transfers to the liquid core to reduce its subcooling (Kelly, 2015). As the liquid subcooling decreases, the vapor generated at the vapor-liquid interface thickens the vapor film and makes the interface wavy. The waviness of the vapor-liquid interface could enhance the turbulence of the vapor film. The IAFB regime can exist till the

void fraction exceeds about 60% (U.S. NRC, 2010). As the void fraction increases and the liquid core disintegrates, the flow transitions to the inverted slug film boiling (ISFB) for flows of low mass fluxes or agitated inverted annular film boiling (AIAFB) for flows of high mass fluxes (Takenaka et al., 1989; Hammouda et al., 1996), where convection becomes the dominant heat transfer mode from the heated wall to the vapor film (Hammouda et al., 1996). Both the ISFB and AIAFB regimes represent transitions from the IAFB to dispersed flow film boiling (DFFB) regimes. When the void fraction exceeds about 90%, all the liquid will exist in the form of entrained droplets due to breakup of the liquid slugs, and this regime is known as DFFB.

Since the peak cladding temperature is usually encountered in the post-CHF regimes during LOCAs and strongly depends on the thermal hydraulics of the IAFB, ISFB, and DFFB, it is important to model these film boiling flows to predict the wall temperature. To accurately predict the wall temperature and void fraction in the post-CHF regimes, the two-fluid model (Analytis and Yadigaroglu, 1987; Hammouda et al., 1997; U.S. NRC, 2010), which is well suited for weakly coupled two-phase flow problems, is selected to model IAFB ISFB/AIAFB and DFFB regimes due to the existence of thermal non-equilibrium conditions in these regimes. In the IAFB regime, heat transfer from the heated wall to the mixture of water and vapor primarily includes two contributors, i.e., conductive heat transfer from the wall to the vapor film and radiative heat transfer from the wall to the liquid (Kelly, 2015). Thermal radiation from the wall to the vapor is neglected (U.S. NRC, 2010) since the vapor film in the IAFB regime is thin and its emissivity is small (Spore et al., 1981). Existing correlations for the wall heat transfer coefficient in the literature were developed based on the saturation temperature instead of the local vapor temperature (Analytis and Yadigaroglu, 1987; Groeneveld et al., 2003) and limited work was performed on the heat

transfer from the vapor to the vapor-liquid interface and from the interface to the liquid core due to lack of experimental data of the void fraction and liquid/vapor temperature, especially at high-pressure and high-flow conditions. Most of the existing heat transfer correlations are empirical or semi-empirical in nature. Physics-based closure relations, including the wall heat transfer and friction, and interfacial heat transfer and drag, are important for improvement of the modeling and simulation of these regimes. The interaction between two phases dominates the vapor generation rate and superheat, associated with extremely complicated characteristics. This presents a major challenge for the estimation of heat transfer because of very limited knowledge on the interfacial transfer processes. In addition, flow regime transition criteria from IAFB to ISFB and from ISFB to DFFB are also required for the closure of the two-fluid model for post-CHF analysis.

## 1.2 Post-CHF Flow Regimes at Subcooled and Low-quality Conditions

CHF indicates a sudden reduction of the heat transfer coefficient between a heated wall surface and the fluid that cools the wall, downstream of which the flow enters post-CHF flow regimes and may cause degradation or even failure of the heated wall. There are two major mechanisms for the onset of the CHF: dryout of liquid film that contacts the heated wall at high-quality flow conditions and departure from nucleate boiling (DNB) at subcooled or low-quality flow conditions. In the post-dryout region, the flow regime is DFFB; while in the post-DNB region, the flow regime is IAFB just downstream of the CHF location and then transitions to DFFB through a transition regime, i.e., ISFB for flows of low mass fluxes or AIAFB for flows of high mass fluxes (Takenaka et al., 1989 and 1990; Hammouda et al., 1996). In a LB-LOCA in light water reactors, post-DNB flow regimes may occur when subcooled water is injected into the reactor core and contacts with

the high-temperature fuel claddings. This dissertation focuses on the post-CHF flow regimes at subcooled and low-quality conditions, i.e., resulting from the DNB mechanism, and therefore the term post-CHF refers to post-DNB.

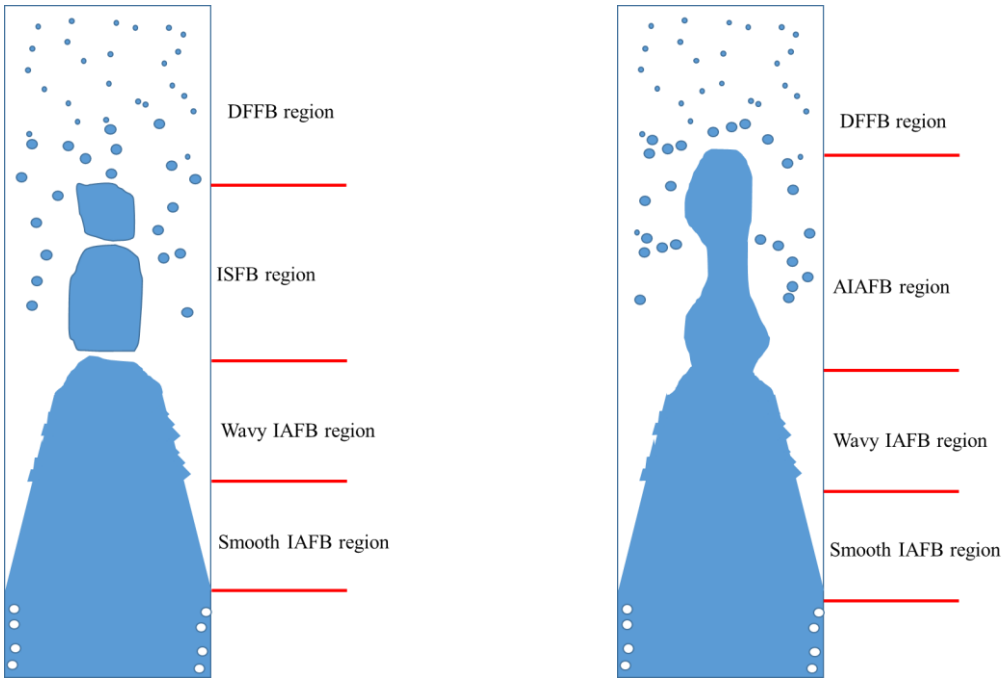


(a) For low mass fluxes (b) For high mass fluxes

Figure 1.2 Flow regime transitions in the post-CHF flow regimes

Figure 1.2 shows the flow regime transitions in the post-CHF regimes for low and high mass flux conditions. Based on the hydrodynamic behavior of the post-CHF flow regimes, Obot and Ishii (1988) divided the post-CHF flow into four basic flow regimes, i.e., smooth and stable region, rough wavy regime, agitated regime (transition flow between inverted annular and dispersed droplet flows), and dispersed ligament/droplet regime. At subcooled flow conditions, IAFB regime exists just downstream of the CHF location and is characterized by a continuous liquid core with a vapor film covering the heated surface. The vapor film is initially a thin layer covering the heated

wall and evaporation occurs at the interface between the subcooled liquid core and the vapor film. The interface is smooth and stable, and significant thermal non-equilibrium exists between these two phases. This region is referred as the smooth IAFB regime. As the vapor velocity and film thickness increase, at a certain point, the vapor-liquid interface becomes wavy and unstable due to the increased vapor generation and reduced liquid subcooling. This region is referred to the wavy IAFB regime. Downstream of the wavy IAFB, the flow regime transitions to the ISFB for flows of low mass fluxes or AIAFB for flows of high mass fluxes, where violent disturbances occur at the vapor-liquid interface and small droplets are entrained from the liquid core. In the ISFB regime, most of the liquid is in the form of liquid slugs in the central region of the flow channel (Hammouda et al., 1996). In the AIAFB regime, the interfacial waves become very irregular and transform to large amplitude or rolling waves (Obot and Ishii, 1988). Both ISFB and AIAFB are considered as a transition regime between the IAFB and DFFB regimes, but their heat transfer characteristics are different due to different flow patterns (Takenaka et al., 1990). In the DFFB regime, liquid droplets of various sizes are formed from the liquid slugs. The vapor phase moves, in average, at a higher velocity than the liquid droplets and the droplets reduce in size due to evaporation and disintegration.

## 1.3 Literature Review

### 1.3.1 Previous post-CHF experiments

Some researchers performed reflooding experiments with water in temperature-controlled systems to study the post-CHF heat transfer characteristics, in which the test sections were first heated to

be above the rewetting temperatures before subcooled water was introduced to quench the test sections progressively. During the reflooding experiments, the wall surface temperature history at a position follows a curve as shown in Figure 1.3. After liquid water is injected into a test section, the wall temperature initially decreases slowly since the flow is in post-CHF flow regimes, which is characterized by poor heat transfer, until there is a sudden reduction of the wall temperature. This process is commonly referred as quenching. Quenching is the rapid cooling of a hot solid surface resulting from enhanced heat transfer conditions and does not necessitate liquid-solid contact, while rewetting implies direct liquid-solid contact and the establishment of a liquid-solid-vapor triple interface (Gunnerson and Yackle, 1981). In the quench front, the heat is removed by axial heat conduction from the hot surface to the cold surface and transition/nucleate boiling from the heated surface to the fluid (Sawan and Carbon, 1975). The quench temperature is defined as the cladding temperature at the onset of rapid cooling, where a significant increase in surface heat transfer and/or axial conduction has occurred. The rewetting temperature is usually lower than the quenching temperature, which denotes a return to transition boiling or nucleate boiling that is characterized by a lager heat transfer coefficient. Before the wall is quenched, the flow is in post-CHF regimes. For high flow or high inlet subcoolings, the flow is IAFB regime just downstream of the quench front, which is a DNB-type CHF, and DFFB regime for low flow or low inlet subcoolings, which is a dryout-type boiling crisis. Axial heat conduction plays an important role during the quenching process. The quench front moves at an approximately constant velocity for a specific condition, which is lower than the reflooding velocity.

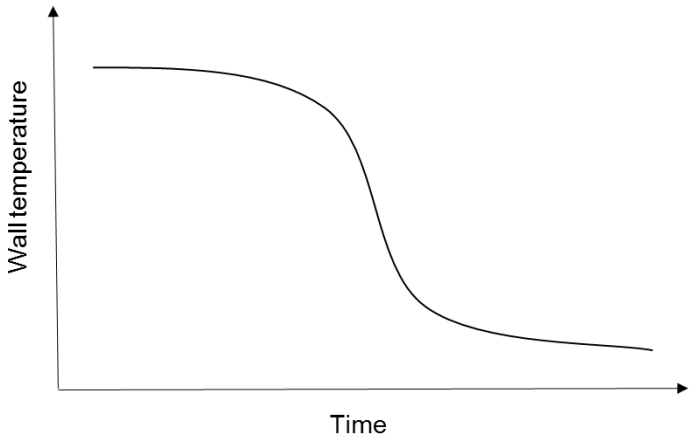


Figure 1.3 Quench curve during reflooding process

A large number of experimental programs have been conducted to investigate heat transfer mechanisms and flow patterns during the reflooding phase of the LOCAs, with a test section of a single tube (Yu, 1978), single rod (Howard et al., 1975; Barnea et al., 1994), or rod bundle (Cadek et al., 1971; Mohanta et al., 2015). Goodman and Elias (1978) observed four regimes, nucleate boiling near the quench front, IAFB regime, ISFB regime, and single phase vapor regime, downstream of the quench front in a 2,000-mm long quartz tube during reflooding experiments with water as the working fluid.

Although a lot of experimental work were performed to study the post-CHF heat transfer characteristics during reflooding, the experimental data are transient data by nature and significant uncertainties are introduced due to the quench front heat release. To benchmark/improve/develop closure models for post-CHF regimes, steady-state experimental data are required in the post-CHF regimes. Before the so-called hot patch technique was developed and widely applied, cryogenic fluids were usually used to perform low-quality and subcooled film boiling experiments in heat flux-controlled systems. This technique was however not applicable to subcooled water since the

high CHF values in water experiments would damage the heated walls (Groeneveld and Gardiner, 1978). This is especially true for subcooled water where the heat flux at CHF is very high. Experiments to perform IAFB tests with water as the working fluid are nearly impossible using a conventional heat flux-controlled system.

To perform steady-state post-CHF experiments with water as the working fluid especially at subcooled and low-quality conditions, Groeneveld (1974) first applied an indirectly heated hot patch technique to achieve quasi-steady-state film boiling. Then in 1984, Chen and Li (1984) proposed a directly heated hot patch technique for their film boiling experimental investigation. The schematic of the hot patch technique is shown in Figure 1.4. The indirectly heated hot patch is a copper block with high thermal inertia and a separate power is included for the hot patch. In the directly heated hot patch technique, the wall thickness of the tubular test section is reduced over a short length at both ends to increase the electrical resistance of the tube at the reduced thickness section. This produces a higher heat flux at the notch location for the same electric current applied to the test section. In both of these two techniques, high heat fluxes are adopted for the hot patch, just upstream of the film boiling section, to form the dry patch in the hot patch, stabilize the quench front, and form a steady-state film boiling phenomenon right downstream of the quench front. The dry patch in the hot patch propagates to the downstream of the hot patch so that steady-state film boiling is achieved in the test section. The function of the hot patch is to prevent the quench front from propagation along the test section and rewetting of the heated tube wall for steady-state film boiling experiments. With this technique, the heat flux values required in the test section are relatively low, which can avoid overheating the test section. With the hot

patch, the film boiling can be formed in the test section with the wall heat flux below the CHF values.

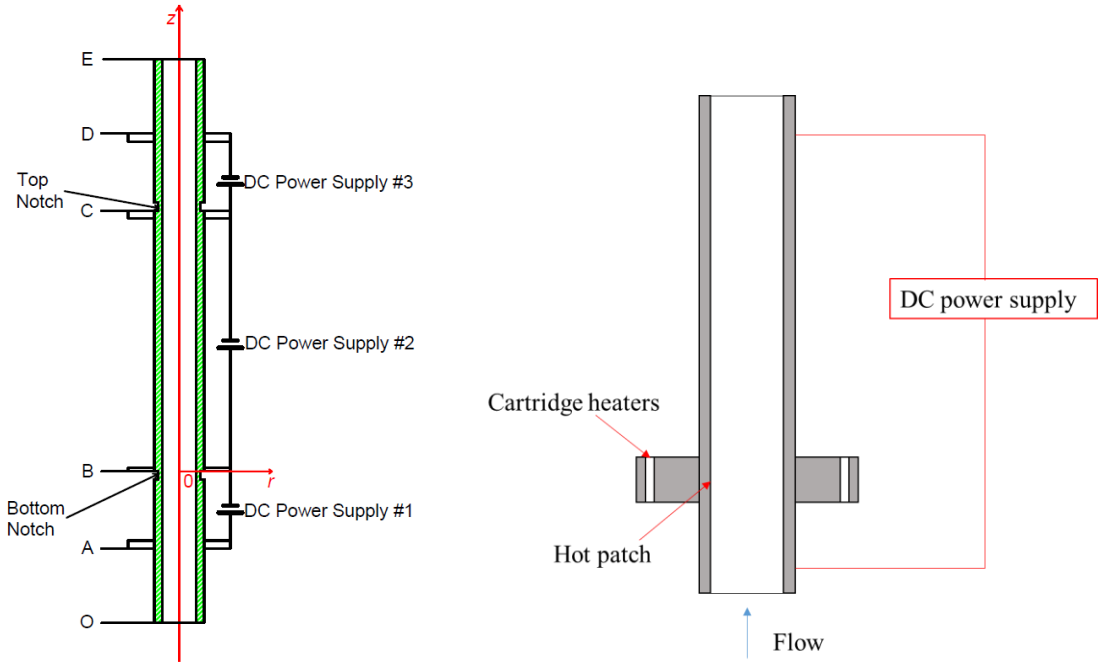


(a) Directly heated hot patch technique (b) Indirectly heated hot patch technique

Figure 1.4 Schematic of the hot patch technique

Both the indirectly heated (Fung, 1981; Stewart, 1981; Laperriere, 1983; Swinnerton et al., 1988; Hammouda et al., 1996; El Nakla et al., 2011) and directly heated (Chen, 1987; Chen et al., 1988, 1989, 1996, 2011; Mosaad and Johannsen, 1989; Savage et al., 1992 and 1993) methods have been widely used in subsequent steady-state film boiling experiments. With the indirectly heated hot patch technique, Fung (1981) obtained extensive film boiling data near the atmospheric pressure condition, while Stewart (1981) and Laperriere (1983) performed film boiling experiments under high-pressure conditions, up to 9.6 MPa. Takenaka et al. (1989), Hammouda et al. (1996), and EI Nakla et al. (2011) performed low-quality quasi-steady-state film boiling tests using cryogenics as the working fluids with the indirectly heated hot patch technique. Groeneveld et al. (2003 and

2007) provided a large amount of experimental data and developed look-up tables for CHF and fully developed film boiling heat transfer coefficients. Mosaad and Johannsen (1989) performed IAFB tests using the directly heated hot patch technique and introduced a heat transfer enhancement parameter to account for improved heat transfer due to the vapor-liquid interfacial waviness. Savage et al. (1992 and 1993) adopted the directly heated hot patch technique to obtain valuable heat transfer and void fraction data for pressures up to 7.0 MPa. With the hot patch technique, a large database for film boiling in tubes has been developed based on steady-state experimental data. However, only a small part of the database includes the void fraction measurement and almost no liquid core temperature measurements are available in the IAFB regime. The void fraction and liquid core temperature are important for benchmarking closure models for the two-fluid model in the post-CHF regimes. Table 1 summarize previous steady-state post-CHF experiments with water at subcooled and low-quality conditions (Fung, 1981; Stewart, 1981; Laperrière, 1983; Costigan et al., 1987; Mosaad, 1988; Swinnerton et al., 1988a and 1988b; Chen et al., 1988 and 1989; Savage et al., 1989, 1992, and 1993). Table 1.2 and Table 1.3 summarizes the test matrices of these previous steady-state post-CHF experiments. The wall temperature was measured in all the experiments but the void fraction was measured in part of the database, i.e., at five elevations in part of Fung's experiments (Fung, 1981), at three elevations in Winfirth Series #3 tests (Savage et al., 1989) and Series #4 tests (Savage et al, 1992), and at two elevations in Winfirth Series #5 tests (Savage et al, 1993). However, no liquid core temperature was measured. The red fonts in Table 1.1 mean that the void fraction was measured in part of the database in the reference. The red fonts in Table 1.2 and Table 1.3 represent the test conditions with void fraction measurement.

Table 1.1 Summary of previous steady-state post-CHF experiments at subcooled and low-quality conditions

| References | ID (mm)/OD (mm) | Length (mm) | Inlet subcooling (°C) | Mass flux (kg/m$^2$-s) | Pressure (MPa) | Hot patch |
|---|---|---|---|---|---|---|
| Fung, 1981 | 11.81/12.70<br>11.94/13.08 | 750-780 | 1-70 | 50-500 | 0.1 | Indirect |
| Stewart, 1981 | 8.93/11.14 | 1,970 | 10-50 | 120-2,750 | 2.0-9.0 | |
| Laperrière, 1983) | | | 10-45 | 1,000-4,500 | 4.0, 9.6 | |
| Costigan, et al., 1987 | 9.85/14 | 920 | 2-50 | 25-150 | 0.2, 0.4 | |
| Mosaad, 1988 | 9/12 | 280 | 0-30 | 50-500 | 0.1 | Direct |
| Chen, et al., 1988 and 1989 | 7/10<br>12/15 | 2,200 | 0-20 | 25-1,500 | 0.1-6.0 | |
| Swinnerton et al., 1988a and 1988b | 9.75/14 | 920 | 5-20 | 50-1,000 | 0.2-2.0 | Indirect |
| Savage, et al., 1989 | 9.75/13.97 | 920 | 5-15 | 50-2,000 | | |
| Savage et al, 1992 | 9.4/12.68 | 920 | 20-50 | 200-1,000 | 0.5-7.0 | Direct |
| Savage et al, 1993 | 9.4/12.68 | 920 | | 100-1,000 | | |

Table 1.2 Test matrix for previous steady-state post-CHF experiments at subcooled and low-quality conditions (0.1 to 0.7 MPa)

| $\Delta T_{sub,in}$* (ºC) | | $P$ (MPa) | | | | | | |
|---|---|---|---|---|---|---|---|---|
| | | **0.1** | **0.2** | **0.25** | **0.4** | **0.5** | **0.6** | **0.7** |
| $G$ (kg/m$^2$-s) | **25** | - | *5,10,20,35,50* | - | *5,10,20,35,50,60* | - | - | - |
| | **50** | *1,5,10,15,20,30,50,60,70* | *2,**5**,20,35,50* | | *5,15,20,35,40,50* | *5* | | |
| | **100** | ***1**,**2**,5,**10**,15,**20**,30,40,50,60* | *5,20,35* | | *5,**15**,20,35,40* | ***5**,10,15,20,25,**30**,**40*** | | |
| | **125** | *1,5,10,15* | - | | - | | | |
| | **150** | *5,10,20,30,40* | *5,20* | | ***5**,**15**,20,30,40* | ***30**,**40*** | | |
| | **170** | *15,25* | - | | - | - | | |
| | **200** | ***1**,5,**10**,15,**20**,30,40* | ***5*** | | | ***5**,10,20,**25**,**35**,**45*** | | |
| | **250** | *5,10,20* | - | | | - | | |
| | **300** | ***1**,5,**10**,20* | | | | - | | |
| | **350** | *5,10,20* | | | | | | |
| | **400** | ***1**,**5**,**10**,**20**,25* | | | | *2,**25**,**30**,**35*** | | |
| | **450** | 30 | | | | - | | |
| | **500** | ***1**,**5**,**10**,**20**,30* | ***5*** | *10* | *15* | ***5**,**30**,**35*** | | |
| | **600** | - | | | | | | |
| | **700** | - | - | - | - | - | *5,10* | - |
| | **750** | | | | | ***30*** | - | |
| | **1,000** | | ***5**,**10*** | | | ***5**,**30*** | *5,10* | |
| | **1,500** | | - | | | - | - | *20* |
| | **2,000** | | ***10**,**15*** | | | ***5*** | | - |

*: The numbers in the columns of different pressures indicate water inlet subcooling values.

Table 1.3 Test matrix for previous post-CHF experiments at subcooled and low-quality conditions (1.0 to 9.6 MPa)

| $\Delta T_{sub,in}$* (°C) | | P (MPa) | | | | | | | | | |
|---|---|---|---|---|---|---|---|---|---|---|---|
| | | 1.0 | 2.0 | 3.0 | 3.5 | 4.0 | 6.0 | 7.0 | 8.0 | 9.0 | 9.6 |
| G (kg/m²-s) | 50 | 5 | | | | - | | | - | | |
| | 100 | 5,30,45 | | | | 30,45 | | - | | | |
| | 120 | - | 10,20 | | | 10,20 | | | 20 | | |
| | 150 | 30,45 | | | | 30,40,50 | | 30,45 | - | | |
| | 200 | 5,10,20,30,40 | 5,40 | - | | 30,35,40,45,50 | - | 35,50 | | | |
| | 215 | - | 10,20 | | | 10,20 | | | 20,35 | | |
| | 250 | 40 | - | | | 30 | | | - | | |
| | 300 | - | 25,30,35,40 | | | - | | - | | | |
| | 350 | 10 | - | | | | | | | | |
| | 359 | - | 10,20 | | - | 10,20,35 | 20,35,50 | | 20,35,50 | | |
| | 400 | 2,25,30,35 | 25,30,35,40 | | 10 | 30 | 5,10 | 30 | - | | |
| | 500 | 5,30,35 | - | | | | - | | | | |
| | 524 | - | 10,20,35 | | | 10,20 | 20,35,50 | | 20,35,50 | 50 | - |
| | 600 | | 25 | | | - | | | - | | |
| | 700 | 20 | - | - | | | | | | | |
| | 923 | - | 10,20 | | - | 20 | 20,35 | - | 20,35,50 | 20,50 | |
| | 1,000 | | 10,15 | | | 20,30 | - | | - | - | 10,25,45 |
| | 2,000 | | - | | | - | | | | 10,20 | 10,25 |
| | 2,750 | | | | | | | | | | |
| | 4,500 | | | | | | | | | - | 10 |

*: The numbers in the columns of different pressures indicate water inlet subcooling values.

### 1.3.2 Closure models

(a) Wall heat transfer

In the past several decades, various heat transfer correlations, including analytical, empirical, and semi-empirical correlations, for the film boiling regimes have been developed. However, due to the complex nature of the physical phenomena in the film boiling regimes and close relationship between heat transfer characteristics and flow regimes, most of the correlations are only applicable to relatively narrow ranges of flow conditions, which limits their applications in practice. There are three major groups of wall heat transfer correlations: (1) modified Bromley's model (Bromley, 1950), (2) modified Dittus-Boelter model (Dittus and Boelter, 1985), and (3) laminar flow model (U.S. NRC, 2010). The modified Dittus-Boelter model was mainly developed for heat transfer in the DFFB regime. This dissertation focuses on the wall heat transfer correlations in the IAFB regime. Therefore, only the modified Bromley's model and laminar flow model are described in this section.

Bromley (Bromley, 1950) performed film boiling experiments on a horizontal and external tube surface, and derived a heat transfer correlation for saturated pool film boiling as:

$$h_c = C\left[\frac{\rho_v g\left(\rho_l - \rho_v\right) H'_{fg} k_v^3}{\mu_v D\left(T_w - T_{sat}\right)}\right]^{1/4}, \tag{1-1}$$

where $h_c$ is the convective heat transfer coefficient (W/m$^2$-K); $\rho_v$ the vapor density (kg/m$^3$); $\rho_l$ the liquid water density (kg/m$^3$); $g$ the gravitational acceleration (m/s$^2$); $H'_{fg}$ enthalpy difference

between the vapor at its arithmetic average temperature and liquid at the saturation temperature (kJ/kg); $k_v$ the vapor thermal conductivity (W/m-K); $\mu_v$ the vapor dynamic viscosity (kg/m-s); $T_w$ the wall temperature (K); $T_{sat}$ the water saturation temperature (K); $D$ outer diameter of the tube (m); and $C$ a constant to be specified.

Bromley et al. (1953) concluded that Eq. (1-1) is applicable to natural convection film boiling where the Froude number $\bar{V}_l / (gD) < 1.0$, and proposed a second empirical heat transfer correlation for the forced convection film boiling for $\bar{V}_l / (gD) > 2.0$ as:

$$h_c = 2.7 \sqrt{\frac{\bar{V}_l k_v \rho_v H'_{fg}}{D(T_w - T_{sat})}}, \tag{1-2}$$

where $\bar{V}_l$ is the area-averaged liquid velocity (m/s).

Later, many researchers developed heat transfer models for film boiling in the framework of the Bromley's model. Berenson (1961) applied the Taylor-Helmholtz instability to film boiling on a horizontal plate and derived a heat transfer coefficient correlation as:

$$h_c = 0.425 \left[ \frac{\rho_v g (\rho_l - \rho_v) h'_{fg} k_v^3}{\mu_v \sqrt{\sigma / g(\rho_l - \rho_v)} (T_w - T_{sat})} \right]^{1/4}, \tag{1-3}$$

where $\sigma$ is the surface tension between the liquid and vapor (kg/s$^2$). The major difference between this correlation and Bromley's model in Eq. (1-1) is the substitution of the characteristic length scale, i.e., the Laplace length scale $\sqrt{\sigma / g(\rho_l - \rho_v)}$, for the tube diameter $D$.

Sudo (1980) assumed that the local subcooling at the quench front had a strong effect on the heat transfer coefficient in film boiling and used the distance between the quench front and the point of interest, $L$, to replace the tube diameter $D$ in Bromley's model. The local subcooling was introduced into the correlation as:

$$h_c = 0.94\left(1 + 0.025\Delta T_{sub}\right)\left[\frac{\rho_v g\left(\rho_l - \rho_v\right)H'_{fg}k_v^3}{\mu_v L\left(T_w - T_{sat}\right)}\right]^{1/4}, \tag{1-4}$$

where $\Delta T_{sub}$ is the liquid subcooling at the quench front (K).

Mosaad and Johannsen (1989) preformed steady-state IAFB tests using directly heated hot patch technique and introduced a heat transfer enhancement factor due to the disturbances to the vapor-liquid interfaces, $\lambda$, and a dimensionless subcooling number, $\theta_s$, to the Bromley's model as:

$$h_c = \lambda\left(1 + 0.4\theta_s + 0.075\theta_s^2\right)\left[\frac{\rho_v g\left(\rho_l - \rho_v\right)H'_{fg}k_v^3}{16\mu_v z\Delta T_s}\right]^{1/4}, \tag{1-5}$$

$$\theta_s = \frac{h^*_{i-l}\Delta T_{sub}}{\Delta T_s\left[\frac{\rho_v g\left(\rho_l - \rho_v\right)H'_{fg}k_v^3}{16\mu_v z\Delta T_s}\right]^{1/4}}, \tag{1-6}$$

$$h^*_{i-l} = 0.8\left[1 + 3.5\left(D/z\right)\right]h_{i-l,\infty}, \tag{1-7}$$

where $h_{i-l,\infty}$ is the heat transfer coefficient from the vapor-liquid interface to the liquid in the fully-developed IAFB regime (W/m$^2$-K); $h^*_{i-l}$ the modified heat transfer coefficient at location $z$ from the vapor-liquid interface to the liquid (W/m$^2$-K); $\Delta T_s$ the wall superheat (K); and $z$ the distance from the location of film boiling incipience (m).

In nuclear reactor thermal hydraulics analysis codes COBRA/TRAC (Thurgood et al., 1983), the critical wavelength of the Taylor-Helmholtz instability was introduced into the Bromley's model and a modified Bromley model was proposed as:

$$h_c = 0.62\left(\frac{D}{\lambda_c}\right)^{0.172}\left[\frac{\rho_v g\left(\rho_l-\rho_v\right)H'_{fg}k_v^3}{\mu_v D\left(T_w-T_{sat}\right)}\right]^{1/4}, \tag{1-8}$$

and the critical wavelength of the Taylor-Helmholtz instability is given as:

$$\lambda_c = 2\pi\sqrt{\frac{\sigma}{g\left(\rho_l-\rho_v\right)}}. \tag{1-9}$$

This model is also used in an improved version of COBRA/TRAC, i.e., COBRA-TF or CTF (Salko et al., 2017), for light water reactor (LWR) safety analysis.

In the system analysis code TRACE (U.S. NRC, 2010), a laminar flow model was proposed for the wall heat transfer coefficient in the IAFB regime. Only heat conduction is assumed in the vapor film region when the vapor-liquid interface is smooth, and the vapor film is in the laminar flow regime. The heat transfer coefficient is given as:

$$h_c = \frac{k_v}{\delta}, \tag{1-10}$$

where $\delta$ is the vapor film thickness (m). The laminar flow model matches well with experimental data when the void fraction is less than 10% but performs poorly as the void fraction increases due to the waviness developed at the liquid-vapor interface (U.S. NRC, 2010). To account for the interfacial disturbances, an enhancement factor, i.e., a non-dimensional vapor film thickness, was introduced in the laminar flow model by Cachard (1996) as:

$$Nu_w = \frac{h_c \delta}{k_v} = 1 + \max\left(0.268\delta^{*0.77} - 0.34,\ 0\right), \tag{1-11}$$

which has a minimum value of unity when $\delta^* = 0$. The term $\left(0.268\delta^{*0.77} - 0.34\right)$ represents the enhancement factor, where $\delta^*$ is defined as:

$$\delta^* = \delta\left[\frac{\rho_v g\left(\rho_l - \rho_v\right)}{\mu_v^2}\right]^{1/3}. \tag{1-12}$$

The Bromley's correlation (Bromley, 1950), Berenson's correlation (Berenson, 1961), and the correlation in the nuclear reactor thermal hydraulics analysis code COBRA-TF or CTF (Salko et al., 2017) will be used for comparison with the experimental data in Chapter 4.

(b) Liquid-side interfacial heat transfer

The liquid-side interfacial heat transfer is necessary to model the IAFB regime using the two-fluid model. In the previous 1-D two-fluid models used by Analytis and Yadigaroglu (1987) and Hammouda et al. (1997), the Dittus-Boelter correlation (Dittus and Boelter, 1985) was used for the liquid-side interfacial heat transfer calculation. Wang and Shi (1985) proposed a model to analyze the liquid-side interfacial heat transfer for turbulent flow of subcooled liquid along a horizontal plate as:

$$Nu_{li} = 0.054\,\mathrm{Re}_l^{\,0.84}\,\mathrm{Pr}_l, \tag{1-13}$$

The characteristic length in Eq. (1-13) is the distance from the dryout point. Takenaka et al. (1989 and 1990) measured the temperature of the inverted annular liquid core near the outlet of their tubular test section in steady-state film boiling experiments with Freon R-113 as the working fluid.

They calculated the mean liquid temperature using Dittus-Boelter correlation (Dittus and Boelter, 1985) and Eq. (1-13), respectively. It was reported that the results obtained with Eq. (1-13) agree better with the experimental results than those obtained with the Dittus-Boelter correlation. Aritomi et al. (1990) proposed an empirical correlation for the liquid-side interfacial heat transfer coefficient but limited to Freon-113 at the atmospheric pressure as:

$$h_{li} = 1.287\left(1 + 0.8\Delta T_{sub} u_l^{1.5} \frac{\delta}{D_c}\right). \tag{1-14}$$

Vijaykumar and Dhir (1992a and 1992b) measured the liquid subcooling, up to 7 ºC, using holographic interferometry on a vertical plate in pool film boiling of water at the atmospheric pressure. The average interfacial heat transfer coefficient was from about 4,000 to 10,000 W/m2-K. Meduri (2007) performed IAFB experiments for water at the atmospheric pressure in a vertical flow channel. The liquid-side interfacial heat transfer coefficient appeared to be strongly dependent upon the value of the liquid subcooling and has an asymptotic value, which increases exponentially as the subcooling decreased and the interface became rough. Kelly (2015) calculated the liquid-side Nusselt number in the IAFB regime based on the experimental data in literature (Fung, 1981; Stewart, 1981; Swinnerton et al., 1988; Chen et al., 1989; Takenaka et al., 1990; Savage et al., 1992 and 1993; Hochreiter et al., 2012) and found no clear effect of mass flux on the liquid-side Nusselt number for mass flux below 1000 kg/m$^2$-s. He proposed a correlation as a function of the Prandtl number as:

$$\mathrm{Nu}_{li} = 130\sqrt{\mathrm{Pr}_l}\,. \tag{1-15}$$

(c) Interfacial friction

In single-phase flows, the friction factor is a function of the Reynolds number and flow channel geometry for fully developed laminar flow and a function of the Reynolds number and pipe roughness in fully developed turbulent flows. Analogous to single-phase flows, the interfacial friction factor in separate gas-liquid two-phase flows is affected by the Reynolds number and interfacial waves. The interfacial waves may be considered equivalent to the pipe roughness in single-phase flows. The characteristics of the vapor-liquid interface in separate two-phase flows have a significant effect on the interfacial friction factor, including interfacial waves, oscillations of the liquid core, droplet entrainment by the gas phase, and turbulence. Currently, there are three main groups of correlations for the interfacial friction factor used for separate two-phase flows: (1) based on the relative vapor film thickness ($\frac{\delta}{D}$), (2) based on the gas Reynolds number ($\mathrm{Re}_v$), and (3) based on a combination of the relative vapor film thickness and gas Reynolds number. Almost all of the correlations for the interfacial friction factor in the IAFB regime are extended from those in annular two-phase flows. In this section, some correlations used in the IAFB regime are briefly introduced. The definition of the interfacial friction factor is as:

$$f_i = \frac{2\tau_i}{\rho_v \left(V_v - V_l\right)^2}, \tag{1-16}$$

where $\rho_v$ is the vapor density (kg/m$^3$); $V_v$ the vapor velocity (m/s); $V_l$ the liquid velocity (m/s); and $\tau_i$ the shear stress at the vapor-liquid interface (kg/m-s$^2$). Wallis (1970) proposed a later widely used correlation for the interfacial friction factor as a function of the relative film thickness for wavy annular gas-liquid flows with no evaporation effects considered as:

$$f_{\text{Wallis}} = 0.005\left(1 + 300\frac{\delta}{D}\right), \tag{1-17}$$

where $f_{\text{Wallis}}$ is the interfacial friction factor by Wallis; $\delta$ the vapor thickness (m); and $D$ hydraulic diameter of the flow channel (m). The term $\frac{\delta}{D}$ is the relative film thickness, which represents the roughness of the interfaces and is equivalent to the pipe roughness in single-phase flows. Wallis validated this correlation using numerous data. At the similar time, Moeck (1970) proposed a similar correlation as a function of the relative film thickness for annular flows as:

$$f_{\text{Moeck}} = 0.005\left[1 + 1458\left(\frac{\delta}{D}\right)^{1.42}\right]. \tag{1-18}$$

Unlike Wallis's correlation, evaporation is considered in the Moeck's correlation. In both the correlations, interfacial waves dominate the interfacial friction, but no Reynolds number is included in the correlations. To account for the evaporation effects in the Wallis's correlation, Fung and Groeneveld (1982) added a vapor generation term in their IAFB physical model as:

$$f_{\text{Fung}} = 1.5 f_{\text{Wallis}}\left(e^{\frac{\phi}{2 f_{\text{Wallis}}}} - \frac{\phi}{f_{\text{Wallis}}}\right), \tag{1-19}$$

$$\phi = \frac{2\Gamma}{\rho_v V_v}, \tag{1-20}$$

$$\Gamma = \frac{D^2}{4\ D - 2\delta}\frac{\mathrm{d}G_v}{\mathrm{d}z}, \tag{1-21}$$

where $G_v$ is the vapor mass flux, kg/m$^2$-s. In a two-fluid model analysis for the IAFB regime, Analytis and Yadigaroglu (1987) improved Wallis' correlation by replacing the value of $f_g$, i.e., 0.005, with $0.085\,\mathrm{Re}_v^{-0.25}$ to account for the effects of interfacial disturbance on the interfacial friction factor as:

$$f_{\text{Analytis}} = 0.085\,\text{Re}_v^{-0.25}\left(1 + 300\frac{\delta}{D}\right), \tag{1-22}$$

$$\text{Re}_v = \frac{\rho_v \ V_v - V_l \ \ 2\delta}{\mu_v}, \tag{1-23}$$

where $\mu_v$ is the vapor dynamic viscosity (kg/m-s). Wang et al. (1988) applied a correlation of the interfacial friction factor in an analysis of the IAFB regime using the two-fluid model as:

$$f_{\text{Wang}} = \frac{0.0791}{\text{Re}_i^{0.25}}\left(1 + 90.9\frac{\delta}{D_c}\right). \tag{1-24}$$

The ratio of the film thickness to the diameter of the cylindrical interface instead of the inner diameter of the pipe is used in Wang's correlation, and a modified gas Reynolds number, $\text{Re}_i$, is used as:

$$\text{Re}_i = \frac{\rho_v \ V_v - V_l \ D_c}{\mu_v}, \tag{1-25}$$

where $D_i$ is the diameter of the cylindrical interface (m). $\frac{0.0791}{\text{Re}_i^{0.25}}$ is the friction factor of the smooth interface and $\left(1 + 90.9\frac{\delta}{D_c}\right)$ is the wavy interface influence factor. The difference between the gas Reynolds number, i.e., Eq. (1-23), and the modified gas Reynold number, i.e., Eq. (1-25), is the choice of the characteristic length, i.e., twice of the film thickness used in the gas Reynolds number while the diameter of the cylindrical interface in the modified Reynolds number. In theory, twice of the film thickness is the hydrodynamic diameter of the gas annulus between the channel wall and central cylinder, which is more meaningful as the characteristic length for the Reynolds number than the diameter of the cylindrical interface. The relationship between the two gas Reynolds number definitions is given as:

$$\mathrm{Re}_i = \mathrm{Re}_v \left( \frac{D_c}{2\delta} \right). \tag{1-26}$$

Aritomi et al. (1990) proposed an empirical correlation by combining the ratio of the film thickness to the diameter of the cylindrical interface and modified gas Reynolds number for inverted annular flows using Freon 113 at the atmospheric pressure as:

$$f_{\mathrm{Aritomi}} = \frac{8.5}{\mathrm{Re}_i^{\,0.25}} \frac{\delta}{D_c}. \tag{1-27}$$

Aritomi et al. (1990) claimed that the proposed empirical correlation could be applied only to Freon 113 at the atmospheric pressure and an additional correction needs to be developed to expand the applicability range. In the nuclear reactor thermal hydraulics analysis code COBRA-TF or CTF (Salko et al., 2017), the Wallis correlation is used for inverted annular flows but multiplied by a factor of 5 as:

$$f_{\mathrm{CTF}} = 0.025 \left( 1 + 300 \frac{\delta}{D} \right), \tag{1-28}$$

Cachard (1996) extended the friction factor between the two parallel plates in single-phase flows to the IAFB regime but introduced a factor, $\lambda_{fv}$, account for the interfacial disturbances and turbulence at the vapor-liquid interface as:

$$f_{\mathrm{Cachard}} = \lambda_{fv} \frac{24}{\mathrm{Re}_v}, \tag{1-29}$$

$$\lambda_{fv} = 0.0362 \ {\delta^*}^{1.96}. \tag{1-30}$$

In TRACE V5.0 (2010), a combination of two correlations was used to calculate the interfacial frication factor in the IAFB regime as:

$$f_{\text{TRACE}} = \sqrt{\left(\frac{144}{\delta^{*3}}\right)^2 + \left(0.35\left(\frac{\delta}{La}\right)^{0.72}\right)^2}\,, \tag{1-31}$$

$$\delta^* = \delta\left[\frac{\rho_v\ \rho_l - \rho_v\ g}{\mu_v^{\ 2}}\right]^{1/3}, \tag{1-32}$$

$$La = \sqrt{\frac{\sigma}{g\ \rho_v - \rho_l}}\,, \tag{1-33}$$

where $\delta^*$ is the non-dimensional vapor film thickness; $\rho_l$ the liquid density (kg/m$^3$); $\sigma$ the surface tension (kg/s$^2$); $g$ the gravitational acceleration (m/s$^2$); and $La$ the Laplace number. The first term under the square-root sign on the right-hand side of Eq. (1-31) is applicable to the smooth region and the second term is applicable to the wavy region. Instead of setting a criterion for the transition from the smooth to wavy IAFB regimes in TRACE, a power law providing a weighting between the two effects is used to combine these two terms as in Eq. (1-31).

(d) Flow regime transition

In the subcooled IAFB regime, a thin vapor film covers the heated wall and a subcooled liquid-core is located in the central region of the flow channel. Unlike pre-CHF regimes, evaporation occurs at the vapor-liquid interface instead of the heat wall surface. The vapor film acts as an insulating blanket, leading to significant thermal resistance between the liquid and the heated wall due to the low thermal conductivity of the vapor. In the subcooled region, most of the heat goes to heat up the subcooled liquid core, which results in a low vapor generation rate and low slip velocity between the two phases and contributes to the stability of the vapor-liquid interface. Therefore, the

larger the liquid subcooling is, in general, the more stable the vapor-liquid interface is. As the bulk liquid-core temperature approaches saturation, the vapor generation rate at the vapor-liquid interface increases. The vapor has a higher acceleration rate than the liquid core due to the low viscosity and low density of the vapor, which, in turn, makes the vapor-liquid interface unstable and further increases the evaporation rate. The surface of the liquid core has a wavy configuration and is disturbed by large waves or bubbles (Ottosen, 1982). As the slip velocity increases, the drag force on the liquid core increases to the point where the liquid core is torn apart into filaments and droplets due to the Kelvin-Helmholtz instability. As the breakup continues, the flow goes through a transition regime to the DFFB regime in which the droplets are irregular and break into smaller droplets.

In the past a few decades, some visual experiments using photography techniques have been performed to study the breakup of the liquid core in the IAFB regime. Westwater and Santangelo (1955) took pictures in their film boiling experiments with methanol as the working fluid. They observed that vapor was generated continuously at the vapor-liquid interface but no vapor was generated at the heated surface, which indicated that the smoothness of the solid and its chemical composition have little effect on the heat transfer. Hsu and Westwater (1958) showed a high-speed still photograph of benzene in the IAFB regime and the vapor-liquid interface was greatly disturbed. Dougall (1963) obtained some photographs of the flow patterns in a test section made of electrically conducting glass tube with Freon R-113 as the working fluid. He observed the IAFB regime with liquid in the middle of the tube and vapor along the wall of the tube, which occurred near the inlet of the test section with low qualities, and stated that the transition from the IAFB to DFFB regimes at an actual flow quality around 10%. Laverty and Rohsenow (1967) performed

film boiling in a Pyrex tube internally coated with a transparent electrically conducting coating using saturated nitrogen as the working fluid and observed the liquid in the center and the vapor in the annulus at the beginning of the heated section, where the vapor fraction was small. Goodman and Elias (1978) observed four regimes, nucleate boiling near the quench front, IAFB regime, ISFB regime, and single-phase steam flow regime, downstream of the quench front in a 2,000-mm long quartz tube during reflooding experiments with water as the working fluid. Ottosen (1982) used gamma rays to measure the void fraction and a high-speed camera to record the flow in a vertical tube for nitrogen in the IAFB regime. Based on the void fraction information and flow pattern photos, he concluded that the flow pattern changed from the IAFB to the DFFB regimes at a void fraction of 0.8 at the atmospheric pressure.

Considering the similarity of the hydrodynamics of a liquid jet-like core with a vapor annulus and the flow pattern in the IAFB regime, some researchers have applied jet breakup methods to predict the disintegration of the liquid core. Ishii and De Jarlais (1986) and Jarlais et al. (1986) reviewed the experimental work on the hydrodynamics of the post-CHF regimes and simulated the inverted annular flow using coaxial gas and liquid jets in adiabatic experiments. Considering the shortcomings of the adiabatic experiments, heat transfer was added in the simulation experiments and correlations for the flow regime transitions were developed based on the experiment results (Ishii and De Jarlais, 1987; Obot and Ishii, 1988, Ishii and Denten, 1990; Babelli et al., 1994). They established the two predominant mechanisms of liquid-core disintegration based on the liquid-jet experiments, i.e., roll wave entrainment and jet instability. The breakup of the liquid core in the IAFB regime is believed to be related to the velocity difference of the vapor and liquid at the liquid-vapor interface, i.e., Kelvin-Helmholtz instability. The vapor has a larger velocity

increase than the liquid due to the smaller inertia of the vapor. When the slip velocity reaches a critical value, the liquid core breaks into filaments and droplets.

In addition to the visualization studies, flow pattern maps for post-CHF flow regimes have also been studied based on the heat transfer characteristics. Takenaka et al. (1989 and 1990) performed post-CHF experiments using Freon R113 and liquid nitrogen as the working fluids and they divided the flow regimes into three regions, i.e., IAFB, AIAFB, and DFFB, for high flow velocities based on the heat transfer coefficients. But for low inlet velocities, the transition regime, i.e., ISFB, cannot be determined based on the heat transfer coefficients because this flow pattern has little effect on heat transfer characteristics. They concluded that these three regions are neither strongly dependent on the heat flux nor the inlet subcooling but are determined by the thermodynamic equilibrium quality and the mass flux. In addition, many studies have used the void fraction as a criterion for the termination of the IAFB regime, such as 0.3 (Mosaad, 1988), 0.4 (Kaufman, 1976), 0.5 (Groeneveld, 1992), or 0.6 (U.S. NRC, 2010).

The Weber number, a dimensionless number for the ratio of the inertia force and surface tension force of the fluid, is useful to explain the breakup of droplets physically (Hinze, 1955) and is widely used to predict the breakup of the droplets in the DFFB regime (Forslund and Rohsenow, 1966 and 1968; Laverty and Rohsenow, 1967; Hynek et al., 1969; Smith, 1976; Arrieta and Yadigaroglu, 1978; Hill and Rohsenow, 1982; Moose and Ganić, 1982). The critical Weber number criterion can also be used to predict the breakup of the liquid core in the IAFB regime, which is determined by the Kelvin-Helmholtz instability due to the vapor-liquid density and velocity differences. Denham (1983) set the value of the critical Weber number as 20 in his model

for the termination of the IAFB regime. Analytis and Yadigaroglu (1987) adopted a value of 8 for the critical Weber number for the stable length of the liquid column in the IAFB regime. Mosaad and Johannsen (1989) took the value of the critical Weber number as 15 for the transition from the IAFB to the ISFB/AIAFB regimes. However, no consensus has been reached on the value of the critical Weber number.

## 1.4 Objectives

The principal objectives of this dissertation are to experimentally study the wall heat transfer characteristics in the post-CHF flow regimes for subcooled and low-quality conditions and benchmark/improve the closure models in the IAFB regime. To achieve these two objectives, a PCHT test facility is designed, constructed, and tested to perform post-CHF experiments and a one-dimensional (1-D) two-fluid model is used to study the closure models for the IAFB regime. The specific tasks are proposed as follows:

Task #1: To design, construct, and test a PCHT test facility at the high-pressure, high-flow, and high inlet subcooling conditions. A series of shakedown tests are to be performed to evaluate the performance of the test facility and ensure that this test facility operates well;

Task #2: To test a gamma densitometer and an X-ray radiography system in subcooled boiling tests. The gamma densitometer and X-ray radiography system are employed to measure the void fraction and flow topology in the test section;

Task #3: To perform post-CHF heat transfer experiments and analyze wall heat transfer characteristics in the post-CHF flow regimes;

Task #4: To benchmark and improve closure models in the IAFB regime, including liquid-side interfacial heat transfer, interfacial friction, and flow regime transition criteria from IAFB to ISFB regimes.

# Chapter 2 Design and Construction of the PCHT Test Facility

## 2.1 Design Requirements

To perform post-CHF heat transfer experiments, a PCHT test facility is designed and constructed at high-pressure and high-flow conditions. The design requirements are as follows:

(1) The flow loop and test section should be able to work at high-pressure conditions, up to 1,000 psi. The mass flux in the test section is from 15 to 2,000 kg/m$^2$-s and the inlet subcooling is up to 50 ºC.

(2) The inside diameter of the test section should be in the range of the hydraulic diameter for BWR and PWR fuel assemblies.

(3) The heated length should be about that of two grid spans in a prototypic PWR rod bundle.

(4) The wall thickness should be maximized to provide strength for high-temperature and high-pressure conditions per ASME code.

(5) The test section is Joule heated and the electrical resistivity of the test section should be relatively temperature independent.

(6) The flow rate, pressure, pressure drop across the test section, fluid temperature at the inlet, outlet, and center of the test section near the outlet should be measured.

(7) The outer surface temperature of the test section should be measured at multiple elevations.

(8) The void fraction and flow topology should be measured by radiation-based measurement technique.

## 2.2 Flow Loop

The PCHT test facility, employing a directly heated circular tube as the test section, is designed to investigate the heat transfer characteristics in the post-CHF regimes under a pressure range of 20 to 1,000 psi (0.14 to 6.8 MPa), a mass flux range of 15 to 2,000 kg/m$^2$-s, and an inlet subcooling up to 50 ºC. The PCHT test facility primarily includes a flow loop and a test section, in addition to its auxiliary system. Figure 2.1 shows a schematic diagram of the PCHT test facility and Figure 2.2 shows a 3D drawing and a photo of the PCHT test facility that was constructed at the University of Michigan (UM). The flow loop mainly consists of:

(1) A reservoir tank for water storage and degassing

(2) A pre-cooler to control the inlet subcooling and prevent pump cavitation

(3) A circulation pump to provide the driving head for the flow loop

(4) A regulating valve to adjust the flow resistance

(5) An electric pre-heater to finely control the inlet subcooling

(6) Test section bypass lines

(7) A condenser to condense the steam in the two-phase mixture out of the test section

(8) A pressurizer to set and adjust the system pressure

(9) A vacuum pump to reduce the amount of air in the system

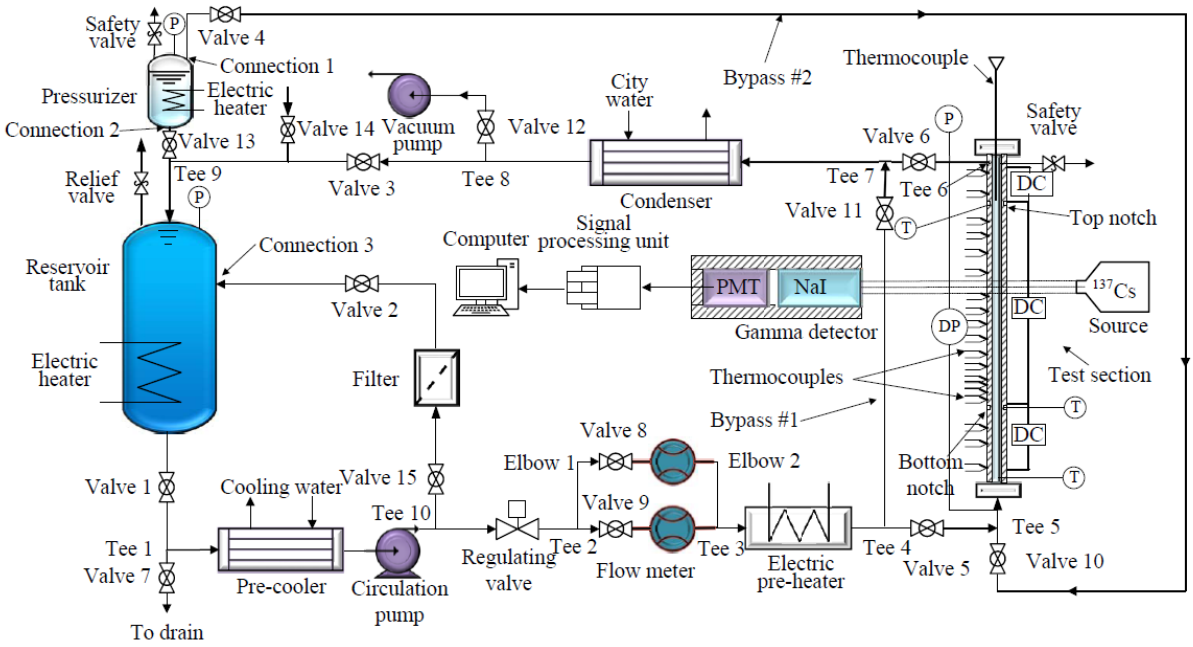


Figure 2.1 Schematic diagram of the PCHT test facility

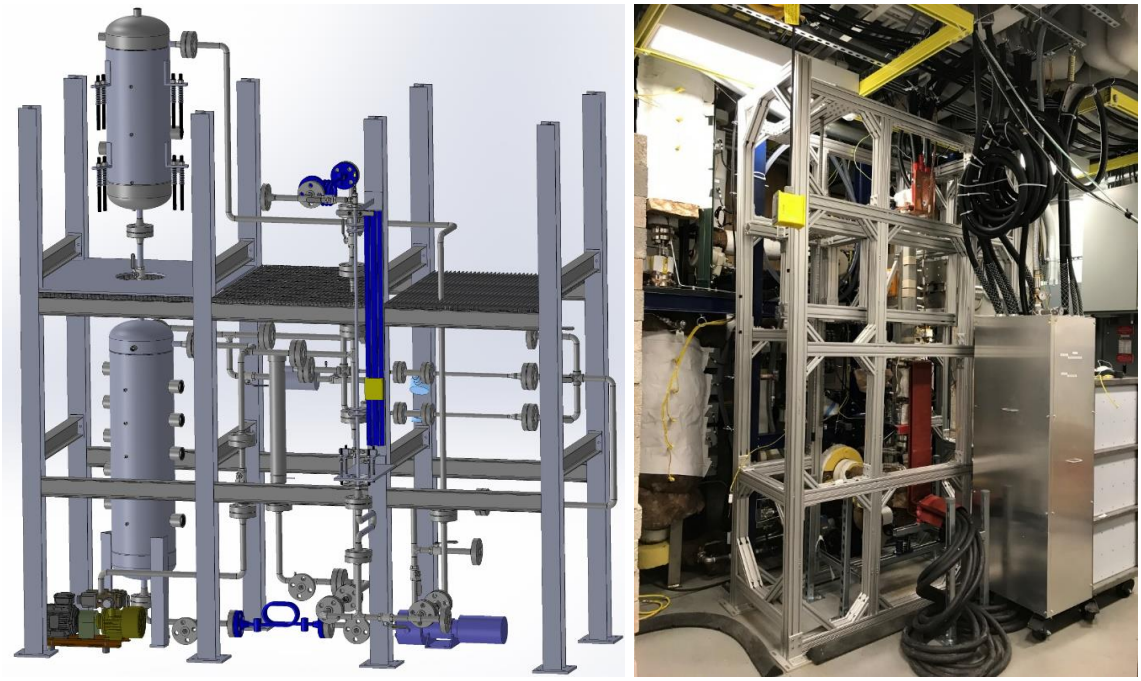

(a) (b)

Figure 2.2 A 3D drawing and a photo of the PCHT test facility

A schematic of the reservoir tank is shown in Figure 2.3. The main functions of the reservoir tank include water storage, water degassing, and coarse control of the water temperature. The reservoir tank features a total storage capacity of approximately 114 liters (30 gallons) and thus a large amount of thermal inertia, which helps stabilize the fluid temperature in the system. Ten electric heaters, with a total heating power of 45 kW, are inserted into the tank from its side for the degassing process and used to heat the water close to the desired inlet temperature during tests.

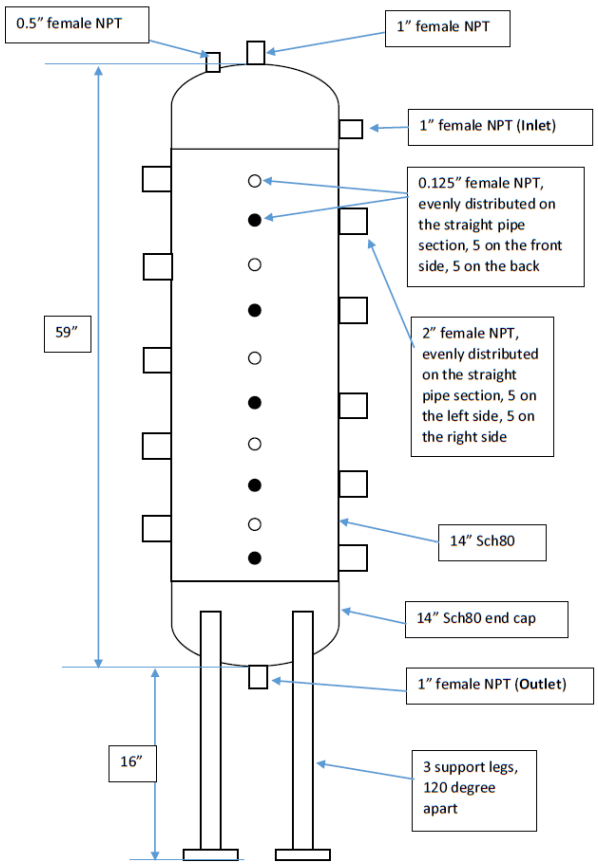


Figure 2.3. Schematic of the reservoir tank design

Figure 2.4 shows a schematic of the pressurizer design. A differential pressure transducer is installed between the top and bottom of the pressurizer to monitor the water level. Water level can

be calculated based on the differential pressure measurement. The pressurizer is used to pressurize the test loop to the desired testing pressures. In addition, it also helps degas the system along with the reservoir tank prior to performing actual tests. It features a total storage capacity of approximately 83 liters (22 gallons) and a heating power of 13.5 kW.

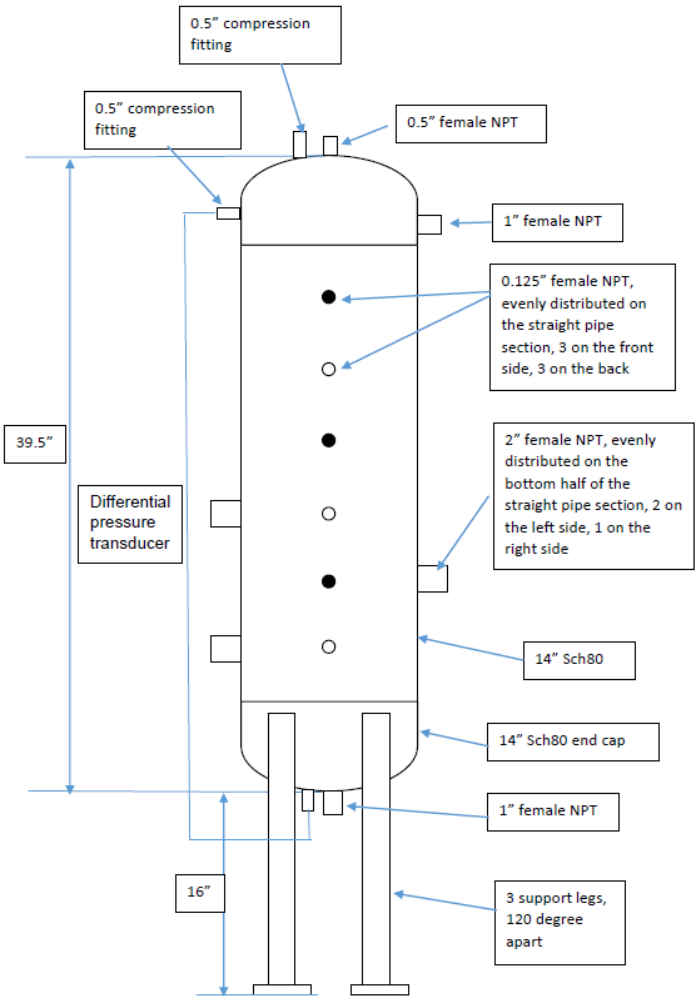


Figure 2.4. Schematic of the pressurizer design

The condenser is used to condense the steam in the steam-water mixture leaving the top of the test section and further cool down the water to a desired temperature. A coiled tube-in-tube heat exchanger is used in the flow loop. The thermal load of the condenser is designed as 35 kW based

on the test section power. It should be noted that there would be a large temperature drop between the cooling water and the heat exchanger wall in the condenser as well as in the pre-cooler, so post-CHF heat transfer could potentially occur on the cooling water side, which will largely reduce the heat transfer coefficient. However, in a coiled tube-in-tube heat exchanger, even though film boiling can occur in the annulus, the vapor will migrate into the periphery due to the centrifugal force, which helps mix the vapor and liquid water. Therefore, film boiling is difficult to form and maintain in the coiled tube-in-tube heat exchanger and is not considered in the current condenser design.

A coiled tube-in-tube pre-cooler is designed to provide a fine control of the test section inlet water temperature to meet the required inlet subcooling. In addition, the water temperature upstream of the circulation pump, i.e., at the pump suction, needs to be below its saturation temperature by a certain degree to prevent any cavitation in the pump. The thermal load of the pre-cooler is designed to be 5 kW. The pre-heater, along with the pre-cooler, is used to provide a fine control of the water subcooling at the inlet of the test section. It has a nominal electric heating power of 6 kW. At the envisioned maximum mass flux of 2,000 kg/m$^2$-s for the test section (corresponding to 0.264 kg/s with the current test section size), the 6-kW pre-heater can provide an adjustment up to 4.9 ºC for the water temperature. A 1.5 HP centrifugal pump from Parker Hannifin Corporation rated at 5,000 psi (MPa) and 343 °C is used to achieve the required flow rate in the flow loop. In addition, a variable frequency drive is used to adjust the frequency in a range of 30 to 76.5 Hz further to adjust the flow rate in the flow loop.

One-inch NPS (Nominal Pipe Size) SS (Stainless steel) 316 pipe and flange (Class 900) connection, which are capable of withstanding high pressures, are selected to be used in the flow loop. The minimum required wall thickness can be calculated as follows (ASME, 2007):

$$t_m = \frac{pD}{2(SE + py)} + A \tag{2-1}$$

where $t_m$ is the minimum required wall thickness (mm); $p$ the internal design pressure (psig). In this calculation, 1,000 psig is used; $D$ the pipe outer diameter (mm); $S$ the maximum allowable stress (psi). In this calculation, the allowable stress at 600 °F is used in Table 2.1; $E$ the weld joint efficiency. One is used for the weld joint efficiency for seamless pipes or tubes; *A* additional thickness (mm) (see explanation below); and $y$ coefficient, 0. It should be noted that, an additional thickness (*A*) corresponding to the thread height should be added for threaded pipes. It is found that, for 1-inch NPS pipes, the minimum required wall thicknesses are 3.03 and 1.27 mm for the thread connection and flange connection, respectively. The 1-inch NPS SCH 40 pipe has a sufficient wall thickness (3.38 mm) and is therefore adopted in the current design.

Table 2.1 Maximum allowable stress of SS 316 per ASME Code Section II (ASME, 2010)

| Temperature (ºF) | 200 | 300 | 400 | 500 | 600 |
|---|---|---|---|---|---|
| Temperature (ºC) | 93 | 149 | 204 | 260 | 316 |
| Maximum Allowable Stress (ksi) | 17.3 | 15.6 | 14.3 | 13.3 | 12.6 |

2.3 Test Section

### 2.3.1 Test section geometric design

Figure 2.5 shows a schematic diagram of the PCHT test section. It consists of a bottom unheated section (OA), bottom hot patch section (AB), bottom notch, film boiling section (BC), top notch, top hot patch section (CD), and top unheated section (DE). Three separate Direct Current (DC) power supplies, i.e., DC Power Supply #1, 2, and 3, are installed respectively between the AB, BC, and CD sections. PID controllers are used for DC Power Supplies #1 and 3 to keep the notches at specific temperatures. Bus bars and electric cables from the power supplies are connected to the disk-shape electrodes that are attached to the outer surface of the tube wall.

Table 2.2 shows the geometrical design parameters of the test section, which is made from a ¾ inch tube. The bottom hot patch section length, bottom notch length and depth, and electrode thicknesses are designed based on the COMSOL simulation results in Section 2.4. The top hot-patch section and top notch are assumed to have the same sizes as those at the bottom. The electrode disk at Point B is desired to be 1.5-mm thick, to more precisely determine the position of the bottom quench front, while the electrode disks at Points A, C, and D are desired to be 4-mm thick, to reduce or remove the heat flux spikes at Point A, C, and D. To make sure that the flow is fully developed at the inlet of the heated section, the bottom unheated section length is to be 400 mm, about 30 pipe diameters.

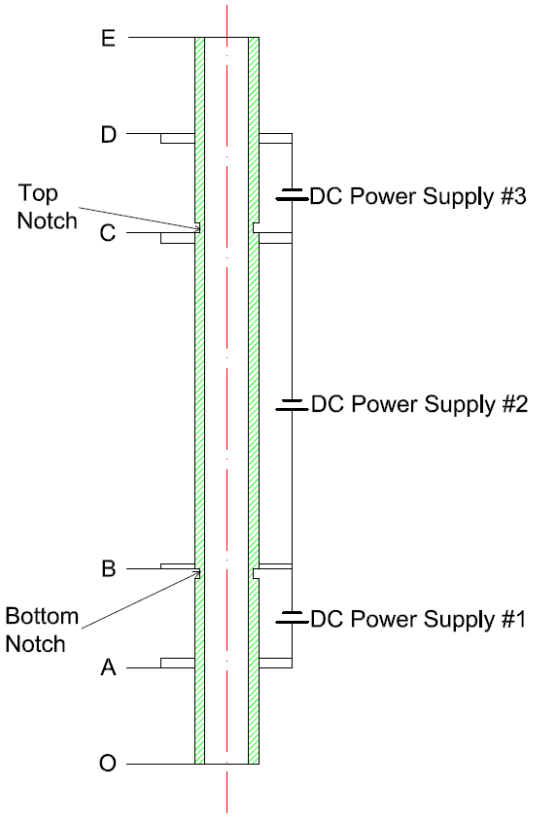


Figure 2.5 Schematic diagram of the PCHT test section (Not Scaled)

Table 2.2 Geometrical design of the test section

| **Items** | **Value (mm)** |
|---|---|
| Tube outer diameter | 19.05 |
| Tube wall thickness | 3.05 |
| Bottom and top notch length | 3.00 |
| Bottom and top notch depth | 1.50 |
| Bottom and top hot patch section length | 25 |
| Thickness of electrode disk at Point B | 1.50 |
| Thickness of electrode disk at Points A, C, and D | 4 |
| Electrode disk side length | 150 |
| Bottom unheated section length | 400 |
| Film boiling section length | 1,000 |
| Top unheated section length | 100 |
| Test section total length | 1,550 |

Seven materials, i.e., Inconel 617, Inconel HX, Incoloy 800HT, Incoloy 800H, HAYNES HR-120, HAYNES HR-160, and HAYNES 556 have been examined per ASME Code Section II (ASME, 2010) and it was concluded that they could potentially meet the structural mechanical requirements of the proposed test conditions. Considering the size of the test section in Table 2.2, only Incoloy 800 H/HT is commercially available with a reasonable cost and therefore is selected as the test section material. It should be noted that Incoloy 800 HT and Incoloy 800 H are very similar in their chemical compositions. Available tubes are dual certified to Incoloy 800 H/HT.

The electrical resistivity and thermal conductivity values of Incoloy 800 H/HT as a function of temperature are shown in Table 2.3. It can be seen that Incoloy 800 H/HT meet the negative temperature feedback requirement for the heating power given a constant voltage applied. The average electrical resistivity of Incoloy 800H/HT is 1.193 μΩ-m between 100 and 1,000 ºC, which is larger than that of SS 316 between 100 and 1,000 ºC (1.016 μΩ-m). In addition, the film boiling section is much longer than that of the electrodes, leading to the electric resistance of the film boiling section much higher than that of electrodes. Therefore, higher resistance (Joule) heat rate will be produced in the film boiling section than that in the electrodes, indicating SS 316 could be a proper candidate as the electrode material, which was also used as the electrode materials in similar test sections in the literatures (Chen et al., 1988; Chen et al, 1989; Mosaad and Johannsen, 1989; Savage et al., 1992). The inner surface roughness of the received Incoloy 800H/HT tube was measured by a Veeco Wyko Non-contact Profilometer (Model Number NT3300) and the average inner surface roughness is 1.425±0.246 μm.

Table 2.3. Electrical resistivity and thermal conductivity of Incoloy 800H/HT

| Temperature (ºC) | Electrical resistivity (μΩ-m) | Thermal conductivity (W/m-K) |
|---|---|---|
| 20 | 0.989 | 11.5 |
| 100 | 1.035 | 13.0 |
| 200 | 1.089 | 14.7 |
| 300 | 1.127 | 16.3 |
| 400 | 1.157 | 17.9 |
| 500 | 1.191 | 19.5 |
| 600 | 1.223 | 21.1 |
| 700 | 1.251 | 22.8 |
| 800 | 1.266 | 24.7 |
| 900 | 1.283 | 27.1 |
| 1,000 | 1.291 | 31.9 |

2.3.2 Pressure and temperature limits of the test section

Incoloy 800H/HT (dual certified based on Incoloy 800H and 800HT) is selected as the material of construction for the test section per ASME codes and commercial availability. The pressure and temperature limits of the Incoloy 800H/HT tube based on the current PCHT test section design are calculated per ASME codes. Per ASME code, the maximum allowable stresses under different temperatures for Incoloy 800H and 800HT are shown in Table 2.4 and Figure 2.6. In Figure 2.6, it can be seen that once the temperature is higher than 600 ºC, the maximum allowable stress decreases significantly as the temperature increases.

Table 2.4 Maximum allowable stress and pressure for the test section per ASME codes (ASME, 2007 and 2010)

| Temperature | | Maximum allowable stress (ksi)* | | Maximum pressure at the film boiling section (psia) | | Maximum pressure at the notch (psia) | |
|---|---|---|---|---|---|---|---|
| $^{o}$F | $^{o}$C | Incoloy 800H | Incoloy 800HT | Incoloy 800H | Incoloy 800HT | Incoloy 800H | Incoloy 800HT |
| 200 | 93 | 15.4 | 15.4 | 4,928 | 4,928 | 2,971 | 2,971 |
| 300 | 149 | 14.4 | 14.4 | 4,608 | 4,608 | 2,778 | 2,778 |
| 400 | 204 | 13.6 | 13.6 | 4,352 | 4,352 | 2,623 | 2,623 |
| 500 | 260 | 12.9 | 12.9 | 4,128 | 4,128 | 2,488 | 2,488 |
| 600 | 316 | 12.2 | 12.2 | 3,904 | 3,904 | 2,353 | 2,353 |
| 650 | 343 | 11.9 | 11.9 | 3,808 | 3,808 | 2,295 | 2,295 |
| 700 | 371 | 11.6 | 11.6 | 3,712 | 3,712 | 2,238 | 2,238 |
| 750 | 399 | 11.4 | 11.4 | 3,648 | 3,648 | 2,199 | 2,199 |
| 800 | 426 | 11.1 | 11.1 | 3,552 | 3,552 | 2,141 | 2,141 |
| 850 | 454 | 10.9 | 10.9 | 3,488 | 3,488 | 2,103 | 2,103 |
| 900 | 482 | 10.7 | 10.7 | 3,424 | 3,424 | 2,064 | 2,064 |
| 950 | 510 | 10.5 | 10.5 | 3,360 | 3,360 | 2,025 | 2,025 |
| 1,000 | 537 | 10.4 | 10.4 | 3,328 | 3328 | 2,006 | 2,006 |
| 1,050 | 566 | 10.2 | 10.2 | 3,264 | 3,264 | 1,968 | 1,968 |
| 1,100 | 593 | 10 | 10 | 3,200 | 3,200 | 1,929 | 1,929 |
| 1,150 | 621 | **9.3** | **9.8** | 2,976 | 3,136 | 1,794 | 1,890 |
| 1,200 | 649 | **7.4** | **8.3** | 2,368 | 2,656 | 1,427 | 1,601 |
| 1,250 | 677 | **5.9** | **6.7** | 1,888 | 2,144 | 1,138 | 1,292 |
| 1,300 | 704 | **4.7** | **5.4** | 1,504 | 1,728 | 907 | 1,042 |
| 1,350 | 732 | **3.8** | **4.3** | 1,216 | 1,376 | 733 | 829 |
| 1,400 | 760 | **3** | **3.4** | 960 | 1,088 | 579 | 656 |
| 1,450 | 788 | **2.4** | **2.7** | 768 | 864 | 463 | 521 |
| 1,500 | 816 | **1.9** | **2.2** | 608 | 704 | 367 | 424 |
| 1,550 | 843 | **1.4** | **1.6** | 448 | 512 | 270 | 309 |
| 1,600 | 871 | **1.1** | **1.2** | 352 | 384 | 212 | 231 |
| 1,650 | 899 | **1.3** | **0.91** | 275 | 291 | 166 | 176 |

*: ksi=1,000 psi

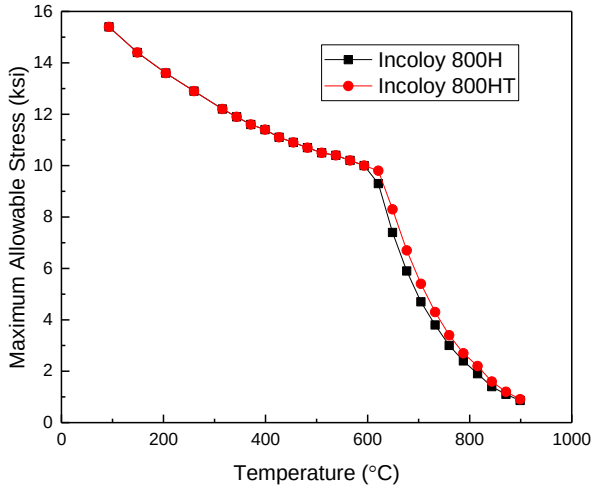


Figure 2.6 Maximum allowable stress of Incoloy 800H and 800HT under different temperatures

Based on the current PCHT test section design in Table 2.2, the allowed internal pressure of the test section tube can be calculated as follows per ASME Code B31.1 (ASME, 2007):

$$P = \frac{2SE(t_w - A)}{D - 2y(t_w - A)}, \tag{2-2}$$

where $t_w$ is the wall thickness (mm). At the film boiling section, the outer diameter of the tube is 19.05 mm and thickness 3.05 mm. At the notches, the values are 16.05 mm and 1.55 mm, respectively. The maximum allowable pressures based on the tube sizes at the film boiling section and notch are calculated under different temperatures and shown in Table 2.4 and Figure 2.7. It can be seen that when the material temperature exceeds 600 ºC, the maximum pressure decreases significantly as the material temperature increases.

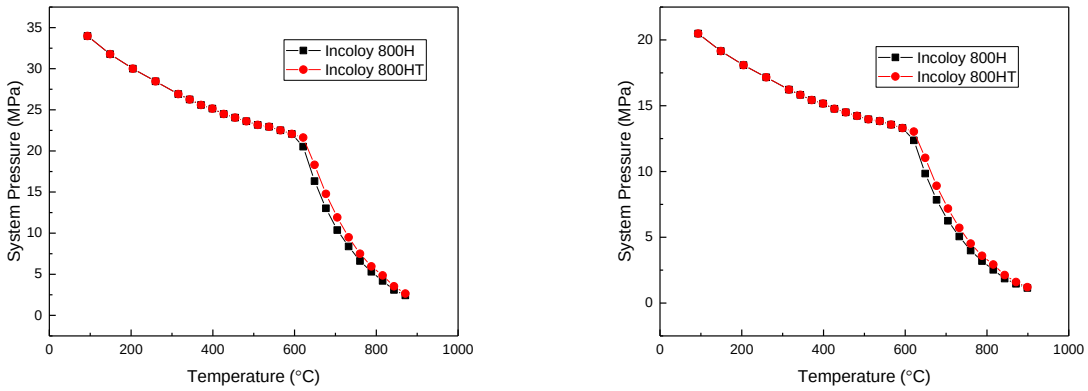


(a) Film boiling section (b) Notch

Figure 2.7 Maximum allowable system pressures under different temperatures

Table 2.5 shows the maximum allowable wall temperatures under different pressures, i.e., 1,000, 500, 350, 200, 60, 40, and 20 psia (6.8, 3.4, 2.4, 1.4, 0.41, 0.28 and 0.14 MPa). It should be noted that the maximum temperatures are interpolated using the data in Table 2.4 based on Incoloy 800H since Incoloy 800H is less strong than Incoloy 800HT. Based on the trend of pressures and temperatures in Table 2.5, the maximum allowable temperatures should be larger than 899 ºC if the system pressures are 200, 60, 40, and 20 psia for the film boiling section and 60, 40, and 20 psia for the notch. In the simulations and actual experiments, the temperatures of the middle points of the bottom and top notch outer surface are controlled to be about 527 ºC (800K) using PID controllers.

Table 2.5 Maximum allowable temperatures under different system pressures for the test section design

| Pressure (psia) | Maximum temperature (°C) | |
|---|---|---|
| | Film boiling section | Notch |
| 1,000 | 755 | 693 |
| 500 | 834 | 774 |
| 350 | 870 | 820 |
| 200 | > 899 | 878 |
| 60 | | > 899 |
| 40 | | |
| 20 | | |

2.3.3 Characterization of the inner surface of the test section

To have a better understanding of the inner surface roughness of the received ¾-inch Incoloy 800 H/HT tube that is used as the test section tube, its inner surface roughness was measured. Figure 2.8 shows the tube samples. The tube piece in Figure 2.8(b) was used to measure the inner surface roughness using a Veeco Wyko Non-contact Profilometer (Model Number NT3300) in five regions on its inner surface.

(a) (b)

Figure 2.8. Tube samples: (a) a one-inch long short section cut from our received Incoly 800 H/HT tube and (b) cut-open tube piece from (a)

Figure 2.9 shows the measurement results of the inner surface roughness of ¾-inch Incoloy 800 H/HT tube. The Veeco Wyko Non-contact Profilometer can only measure the surface roughness of a plane. So small regions at the inner surface bottom of the tube piece shown in Figure 2.8 b), which are approximate to planes, are measured. The figures on the left in Figure 2.9 show the roughness along the X profile, and the figures on the right show the roughness along the Y profile.

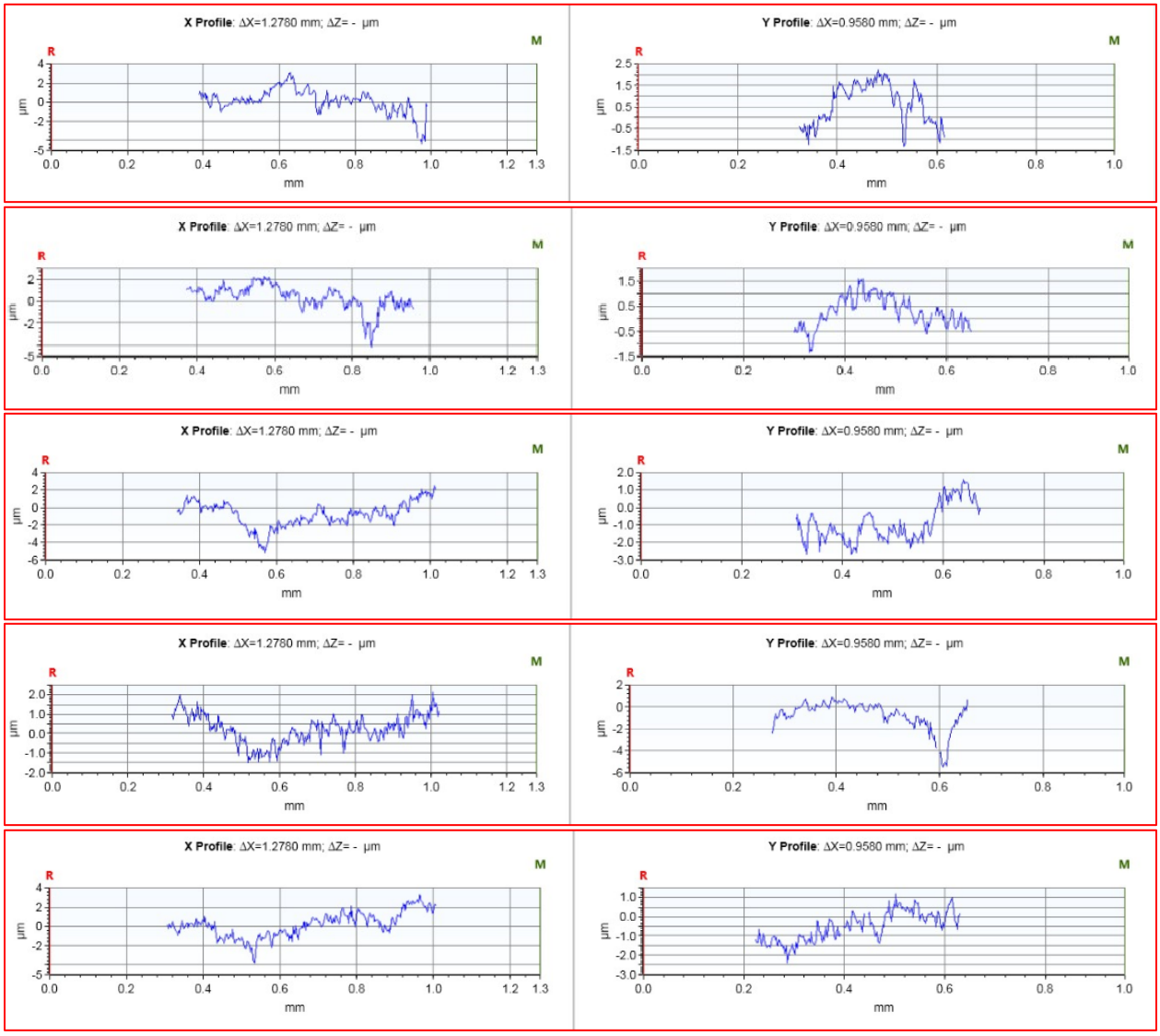


Figure 2.9. Measurements of the inner surface roughness of ¾-inch Incoloy 800 H/HT tube

There are many different roughness parameters in use, such as $Ra$, $Rp$, $Rv$, $Rt$, and $Rq$, but $Ra$ is by far the most common. Table 2.6 shows the measured roughness values of the five semi-circular tube samples. In the table, the number of the data points refers to the total number of measurements in each region. The arithmetic average surface roughness (Ra) is 1.452 ± 0.246 μm for these measurements.

Table 2.6. Specific roughness data of our received ¾-inch Incoloy 800 H/HT tube

| | | Value | | | | |
|---|---|---|---|---|---|---|
| 1 | No. of data points | 91,428 | 145,307 | 113,608 | 86,088 | 73,257 |
| | $Ra$ (μm) | 1.187 | 2.817 | 1.564 | 1.603 | 1.077 |
| 2 | No. of data points | 58,287 | 76,577 | 83,271 | 89,813 | 99,323 |
| | $Ra$ (μm) | 1.020 | 1.218 | 1.188 | 1.290 | 1.405 |
| 3 | No. of data points | 82,518 | 110,605 | 71,766 | 79,676 | 72,521 |
| | $Ra$ (μm) | 1.090 | 1.598 | 0.922 | 1.123 | 1.348 |
| 4 | No. of data points | 65,353 | 69,200 | 96,630 | 71,413 | 72,879 |
| | $Ra$ (μm) | 1.074 | 1.234 | 1.533 | 1.445 | 1.358 |
| 5 | No. of data points | 43,862 | 51,098 | 61,393 | 67,025 | 71,352 |
| | $Ra$ (μm) | 0.999 | 1.18 | 2.014 | 1.615 | 2.018 |
| Average surface roughness (μm) | | 1.452 | | | | |

Note: $Ra$ is the arithmetic average surface roughness; $Rp$ the maximum peak height; $Rv$ the maximum valley depth; $Rt$ the maximum height of the profile, $Rp + |Rv|$; $Rq$ the root mean squared.

In addition to the roughness measurements of the as-received Incoloy 800 H/HT tube, a one-inch long Incoloy 800 H/HT tube is used to characterize its inner surface by a Scanning Electron Microscope (SEM) from the Center for Electron Microscopy and Analysis at the Ohio State University (OSU). Figure 2.10 shows the Quanta 200 SEM and Figure 2.11presents the SEM

measurement results. From these results, we could develop a better understanding of the inner surface characteristics, which indicate that the inner surface has some small pits.

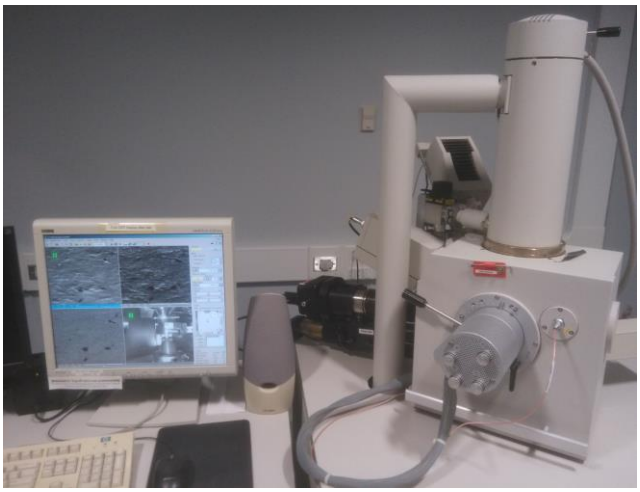

Figure 2.10 Quanta 200 SEM

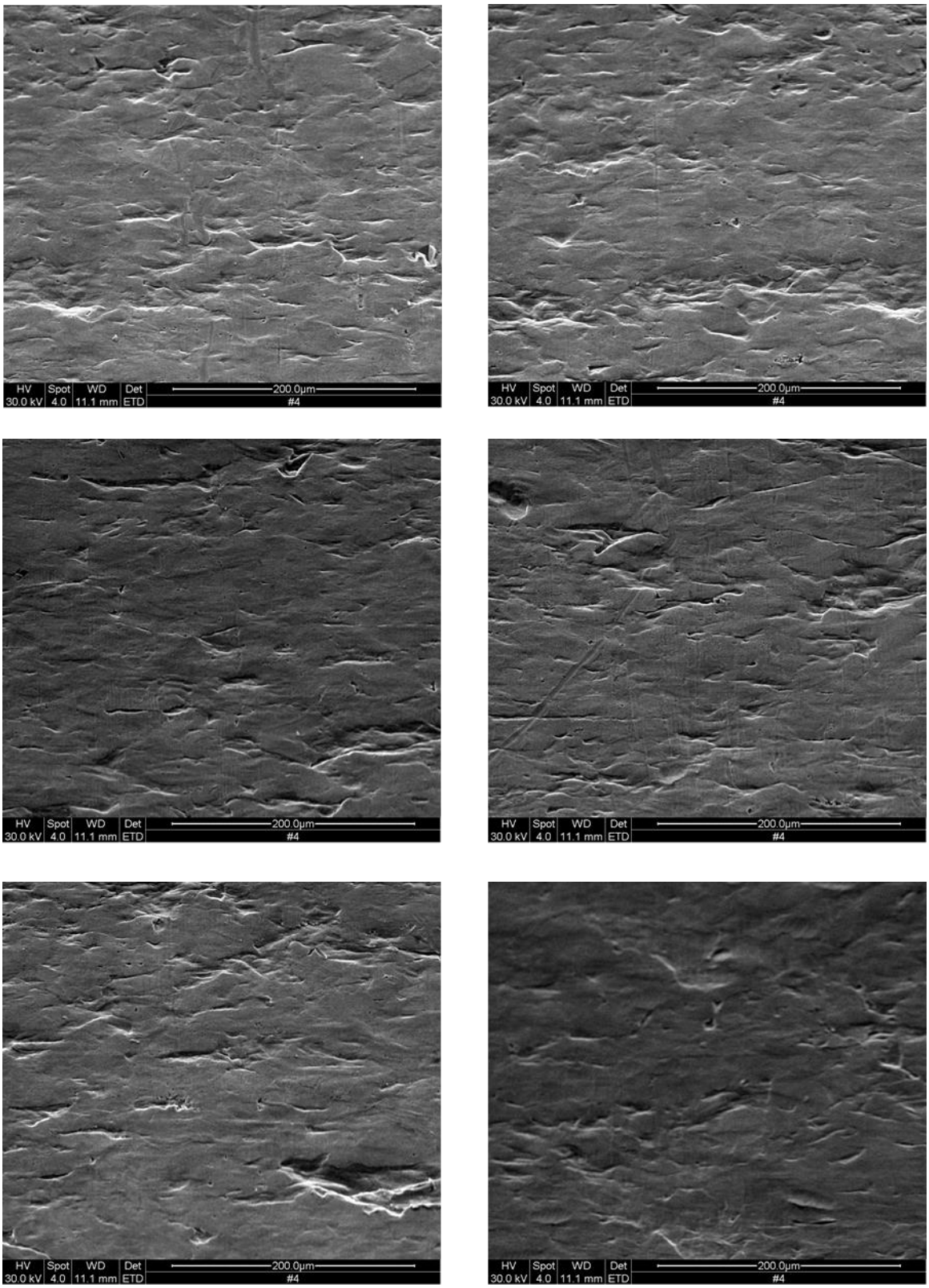


Figure 2.11 Inner surface characteristics of the as-received Incoloy 800 H/HT tube by SEM

### 2.3.4 Test section fabrication and installation

In the shakedown tests, three reduce-length test sections (RTSs) were designed and fabricated as shown in Figure 2.12. There are eight thermocouples spot welded (using microscopic laser welding technique) onto the test section, with five on the tube surface, one in the top notch, and two in the bottom notch. In the bottom notch, the signal of one thermocouple will provide an input signal (as a reference) to a PID controller to control the power of DC Power Supply #1, which provides heating to the bottom hot patch, and the second thermocouple will provide a temperature input to the LabVIEW program for the temperature measurements and data recording. It should be noted that the thermocouple signal is a very low-level millivolt signal and that as such it should only be connected to one device. Splitting one thermocouple output signal to two devices may result in erroneous readings or loss of signal strength.

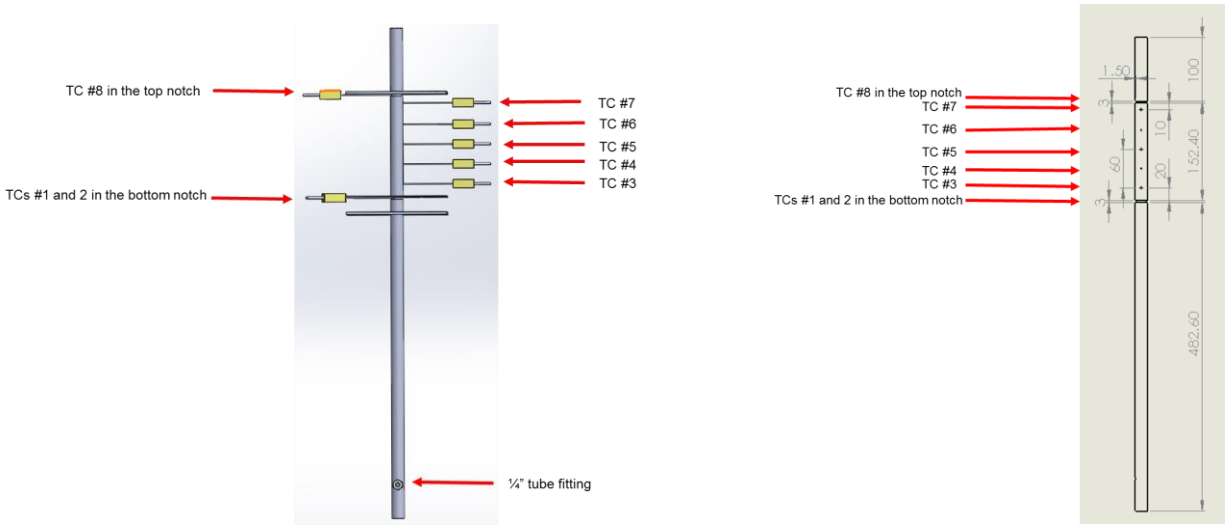


(a) (b)

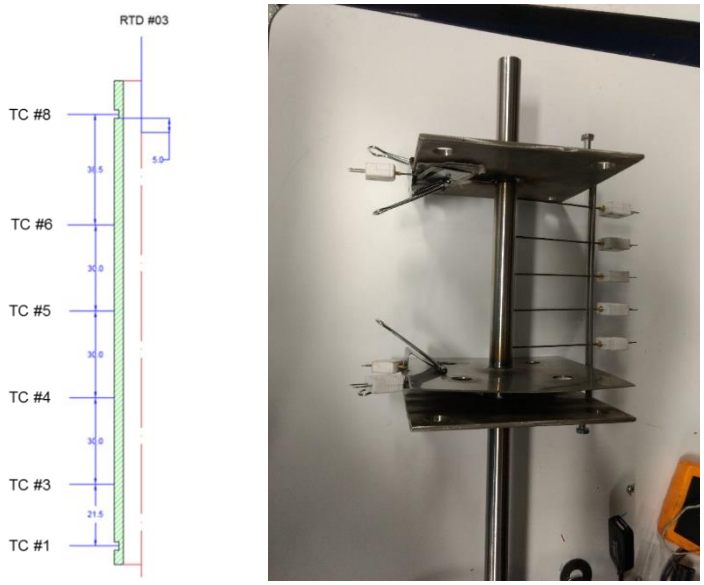


(c) (d)

Figure 2.12 Design and fabrication of RTS (Unit: mm)

A full-length test section (FTS) was designed based on the dimensions in Table 2.2 and fabricated as shown in Figure 2.13. A total of 21 1/16" K-type sheathed but ungrounded thermocouples were attached to the test section using microscopic laser welding technique. Four thermocouples are in the two notches (two in each notch), and 17 thermocouples are attached on the outer surface of the

test section. To protect the thermocouples from potential damage, a removable holder was installed on the test section to support the thermocouples. After the test section was installed in the flow loop, the removable holder was removed carefully.

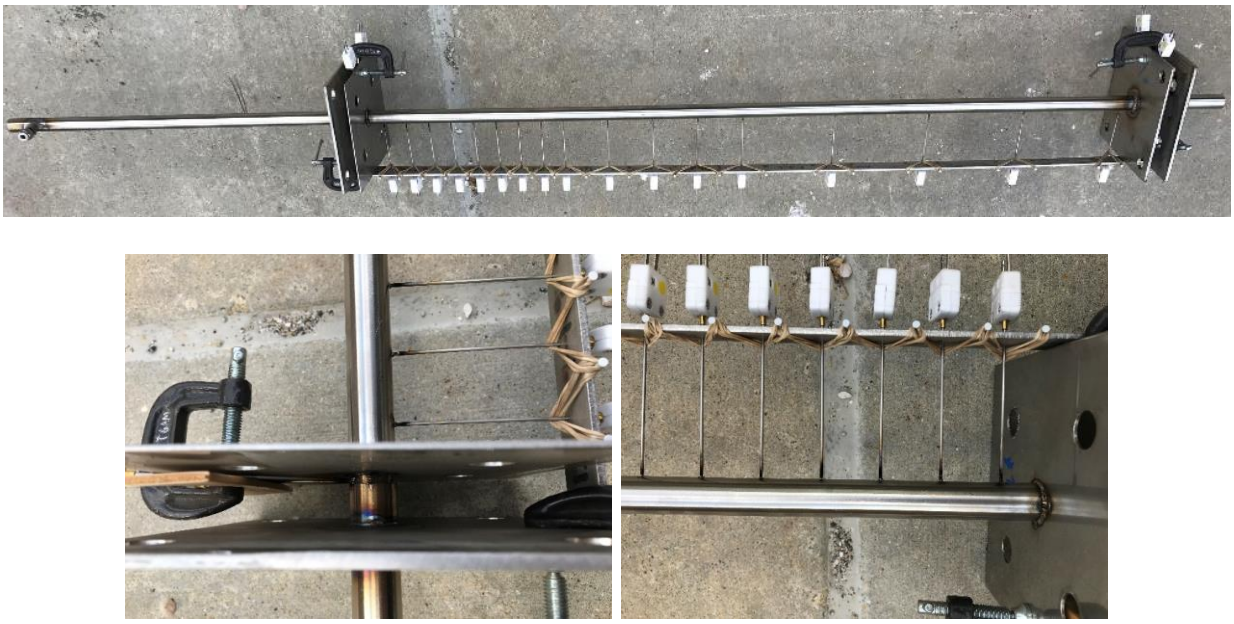

Figure 2.13 Design and fabrication of the FTS

Figure 2.14 shows the test section installed in the flow loop. The top of the test section is fixed by a clamp, which is connected to the I-beam structure. The bottom of the test section is connected to a U-loop, which allows thermal expansion towards the bottom of the test section. Three DC power supplies were connected to the full-length test section as shown in Figure 2.15 and the thermocouple extension wires were connected to the 21 thermocouples that are attached to the test section as shown in Figure 2.16. Also, one-inch-thick microporous insulation has been applied to the test section as shown in Figure 2.17. All the 21 thermocouples have been connected to the NI (National Instruments) modules.

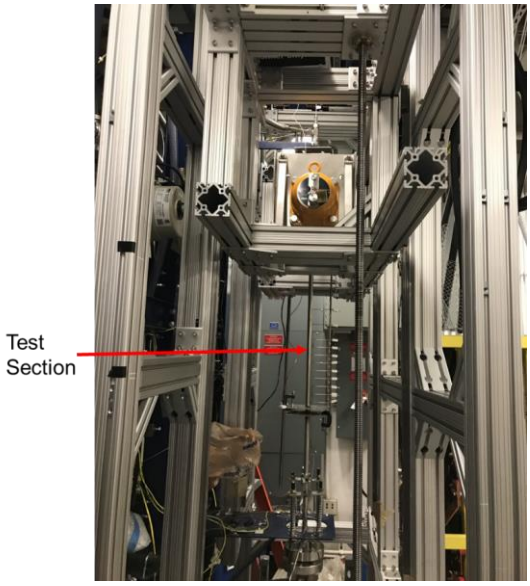


Figure 2.14 Installation of the full-length test section in the flow loop

(a) (b) (c)

Figure 2.15 DC power supply connections to the FTS

(a) (b) (c)

Figure 2.16 Thermocouple extension wire connections to the thermocouples on the FTS

(a) (b) (c)

Figure 2.17 Thermal insulation installed on the FTS

## 2.4 COMSOL Multiphysics Simulation

To ensure that low-quality quasi-steady-state film boiling experiments can be achieved in the directly heated circular tube, Kelly (2015) developed a model using COMSOL Multiphysics software to provide guidance for the design of the test section, such as the tube sizes, tube material selection, and test section power. To make the model more representative of the actual situation, the model has been improved by using three separate DC power supplies and adding thermal insulation material outside the test section tube. With the improved model, more simulations at different test conditions are performed to predict the wall heat flux and wall temperature distributions and needed heating power for the test section. In addition, the effects of insulation thickness on the heat loss from the test section and temperature distributions of the insulation outer surface, and the effects of the electrode thickness and length of the top hot patch on the heat flux distributions are also studied.

### 2.4.1 Computational model descriptions

The COMOSL simulation domain includes the Incoloy 800 H/HT tube wall and thermal insulation materials as shown in Figure 2.18. A two-dimensional computational model is adopted to reduce the calculation time, considering the axial symmetry of the test section. The test section consists of a bottom unheated section (OA), bottom hot patch (AB), bottom notch, film boiling section (BC), top notch, top hot patch (CD), and top unheated section (DE). Three separate DC electric voltages are applied to the AB, BC, and CD sections. The geometrical parameters (except the bottom unheated section length) of the model are the same with those shown in Table 2.2. The actual bottom unheated section length is 400 mm to make sure that the flow is fully developed at the inlet of the heated section. To reduce the calculation time, the bottom unheated section length

is assumed to be 40 mm in the COMOSL numerical model. The thermal insulation thickness of the test section is assumed to be 50 mm.

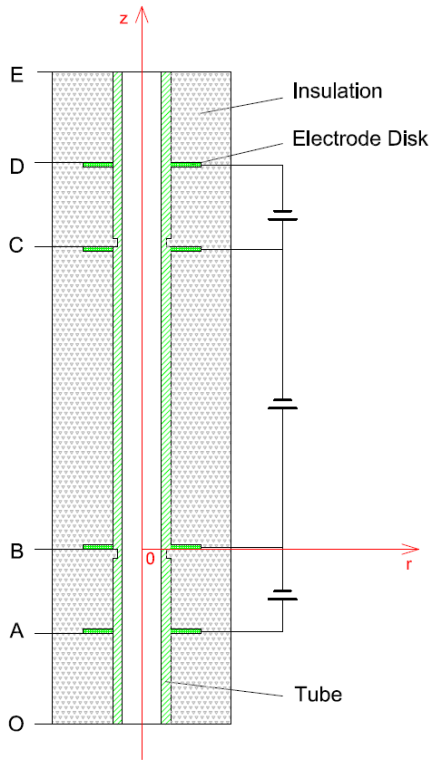


Figure 2.18. Schematic diagram of the geometric model (Not Scaled)

The test section tube material is modeled as Incoloy 800 H/HT, and its electrical resistivity and thermal conductivity values are given in Table 2.3. The test section is insulated with microporous pipe insulation, which has an extremely low coefficient of thermal conductivity, as shown in Table 2.7. Because the 50-mm thick pipe thermal insulation has a very large electrical resistance (> 2,000 MΩ), the pipe insulation is assumed electrically insulative in this model.

Table 2.7. Thermal conductivity of microporous pipe insulation

| Temperature (°C) | Thermal conductivity (W/m-K) |
|---|---|
| 50 | 0.018 |
| 100 | 0.019 |
| 200 | 0.020 |
| 300 | 0.022 |
| 400 | 0.024 |
| 500 | 0.027 |
| 600 | 0.031 |
| 700 | 0.035 |
| 800 | 0.040 |

The model methodology in this simulation is as follows:

(1) Two PID (Proportional-Integral-Derivative) controllers are adopted at the bottom and top hot patches to determine the hot patch heating power values and fix the quench front by keeping the notch at a specific temperature between 650 and 800 K, which is determined based on the water pressure, mass flux, and inlet subcooling.

(2) In the IAFB regime, the heat flux at the film boiling section is selected to be large enough to form film boiling but small enough to keep the flow at subcooled conditions. In the ISFB regime, the heat flux is selected to be large enough to form inverted slug film boiling.

(3) The time step can be automatically adjusted to accelerate the convergence and reduce the computation time in COMSOL.

The model in the test section is developed based on the heat conduction equation with consideration of Joule heating as the internal heat source. It can be described as follows,

$$\frac{\partial\left(\rho c_p T_w\right)}{\partial t} = \frac{1}{r}\frac{\partial}{\partial r}\left(kr\frac{\partial T}{\partial r}\right) + \frac{\partial}{\partial z}\left(k\frac{\partial T}{\partial z}\right) + \dot{q}_v, \tag{2-3}$$

where $T_w$ is the temperature of the test section wall (ºC); $t$ the heating time (s); $k$ the thermal conductivity of the test section wall (W/m-K); $\rho$ the density of the test section wall (kg/m$^3$); $c_p$ the heat capacity of the test section wall (J/kg-K); $\dot{q}_v$ the internal heat source in the test section wall (W/m$^3$). The tube wall is resistance (Joule) heated by applying the three separated electric voltages. The voltage applied to the film boiling section is determined from the desired heat flux and held constant during a test. This DC power voltage needs to generate a heat flux that is above the minimum film boiling heat flux to prevent spontaneous quenching of the film boiling section. The maximum heat flux value is primarily limited by the temperature limits of Incoloy 800 H/HT per the ASME code (ASME, 2010). The bottom and top hot patch voltages are PID controlled to keep the notch mid-point temperature at the set values. No internal heat generation is assumed in the thermal insulation since its electrical resistance is very large as explained earlier.

On the inner surface of the Incoloy 800 H/HT tube, convective and nucleate boiling heat transfer modes are assumed for the bottom hot patch section, and film boiling is assumed for the rest of the test section. CHF and heat transfer coefficient data are obtained from the look-up tables for the CHF and fully developed film boiling heat transfer in the literatures (Groeneveld et al., 2003; Groeneveld et al, 1996). On the outer surface of the insulation, natural convection heat transfer is assumed between the outer surface of the insulation and the environment, and the natural convection heat transfer coefficient is assumed to be constant, namely 10 W/m$^2$-K, for simplification. However, the effects of the insulation thicknesses on the heat loss to the ambient and the temperature distributions of the outer surface of the insulation are closely related to the natural convection heat transfer coefficient. Therefore, iterative calculations are performed to

obtain more accurate calculations of the natural convection heat transfer coefficient and therefore the heat loss from the test section to the ambient air.

To determine the maximum required test section power, simulations are performed at the highest mass flux and highest inlet subcooling with different water pressures. Heat flux is kept relatively low to make sure that the flow achieves subcooled film boiling. With these simulations, the design power supply values, including the bottom hot patch power, top hot patch power and film boiling section power are determined. In addition, the wall heat flux and wall temperature distributions are also be calculated. The simulation conditions are as follows:

Pressure: 20, 100, 300, 500, 600, 800, and 1,000 psi,

Mass flux: 2,000 kg/m$^2$-s,

Inlet subcooling: 50 ºC.

With the test section power determined based on the simulations in the IAFB regime, simulations are performed under various conditions to predict the wall temperature distributions and outlet quality in the ISFB regime. Since in the ISFB regime there is a higher quality and the liquid is almost saturated (Kelly, 2015; Hammouda et al., 1996) at the test section exit, the heat flux at the film boiling section is selected to be higher than that in the IAFB regime for the same test conditions. The simulation conditions are as follows:

Pressure: 100, 300, and 500 psi,

Mass flux: 500, 1,000, and 2,000 kg/m$^2$-s,

Inlet subcooling: 10, 30, and 50 ºC.

### 2.4.2 Thermal analysis in the IAFB regime

(a) Wall heat flux distributions

The operating principle of the hot patch technique is to supply enough independent power to a short section just upstream of the test section to reach CHF, thereby preventing the quench front from advancing upward. Figure 2.19 shows the calculated heat flux distributions along the axial direction at water pressures of 20 and 100 psi, mass flux of 2,000 kg/m$^2$-s, and inlet subcooling of 50 °C. Two heat flux peaks are created due to the higher electric resistance at the bottom and top notch. The bottom heat flux peak can prevent the quench front from advancing into the film boiling section and the top heat flux peak can prevent top-down progression of a quench front from the top unheated section. In the film boiling section, the heat flux is almost uniform and much smaller than the heat flux peak to avoid the wall temperature being too high. In addition, the heat flux values at 100 psi are larger than those at 20 psi, which suggests that at higher pressures, higher power is needed to form the IAFB regime at the same mass flux and inlet subcooling.

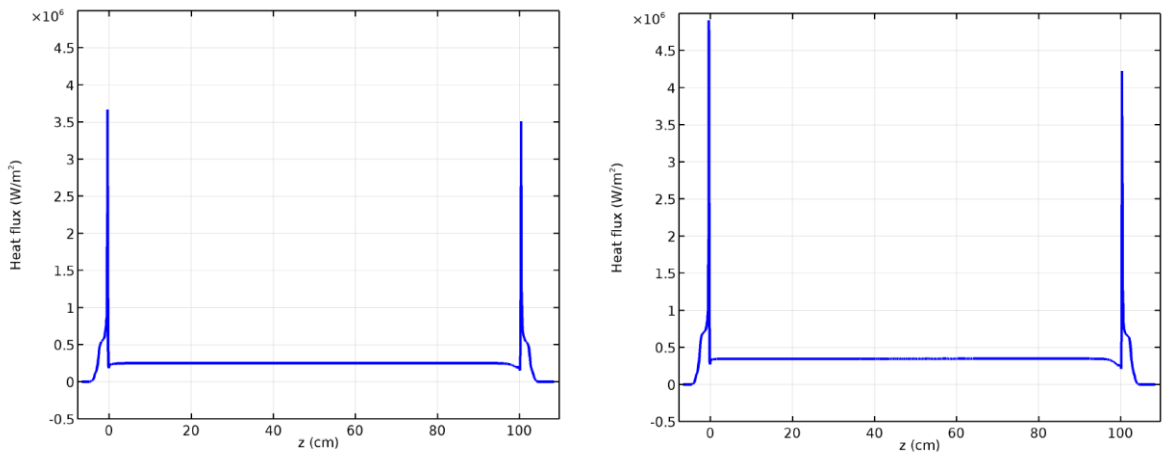


(a) (b)

Figure 2.19. Heat flux distributions along the axial direction at mass flux of 2,000 kg/m$^2$-s and inlet subcooling of 50ºC at the water pressures of (a) 20 psi and (b) 100 psi

(b) Wall temperature distributions

Figure 2.20 shows the wall temperature distributions along the axial direction at water pressures of 500 psi and 1,000 psi, mass flux of 2,000 kg/m$^2$-s, and inlet subcooling of 50 °C. At the bottom hot patch where the liquid is subcooled, the heat transfer modes are single-phase convective heat transfer and nucleate boiling heat transfer, so the heat transfer coefficient in that section is large, leading to a relatively low wall temperature. When water flows into the film boiling section and contacts with a hot wall at a high temperature, vapor will be generated dramatically and covers the heated wall, forming a vapor film and reducing the heat transfer coefficient. Therefore, the wall temperature in the film boiling section is much higher than that at the bottom hot patch shown in Figure 2.20. In addition, it can be seen that the temperature difference between the inner wall and outer wall is not very large, less than 50 ºC in the film boiling section, which would be used as the

correction for the inner wall temperature to be derived from the outer wall temperature measurements.

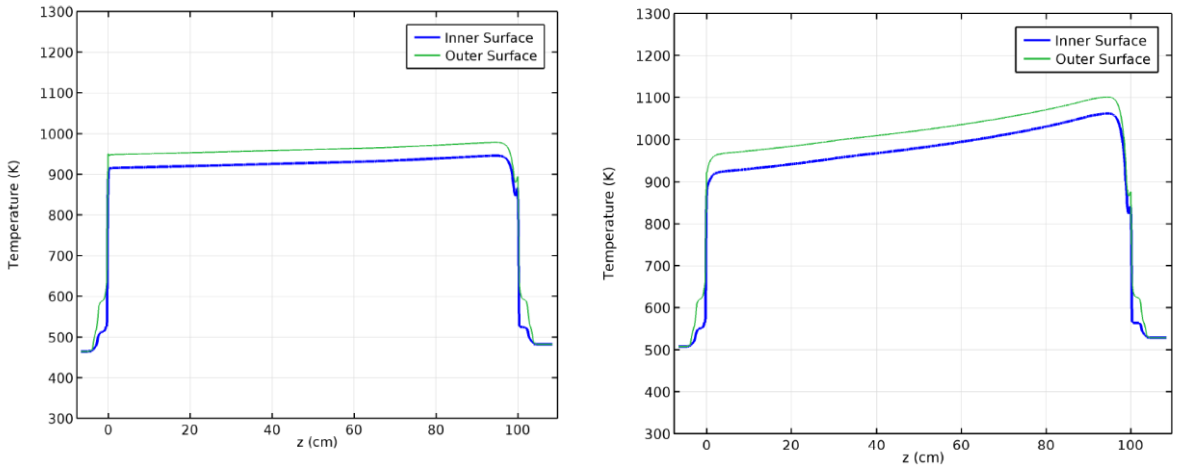


(a) (b)

Figure 2.20 Wall temperature distribution along the axial direction at mass flux of 2,000 kg/m$^2$-s and inlet subcooling 50 ºC at the water pressures of (a) 500 psi and (b) 1,000 psi

In the IAFB regime, heat is transferred from the tube wall to the liquid by both thermal convection and conduction through a vapor film. Due to liquid evaporation by the wall heating, the quality of the flow increases along the axial direction. As the quality increases, there are two opposite effects on the heat transfer coefficients. On one hand, the vapor film thickness increases with the increase of the vapor quality, which will weaken the thermal conduction through the vapor film. On the other hand, the vapor velocity will also increase because the quality increases, which can promote the convective heat transfer. In Figure 2.20, it can be seen that the wall temperature increases along the axial direction, which indicates that the heat transfer coefficient in the film boiling section decreases along the axial direction. Therefore, the weakening effect on the vapor thermal

conduction is dominant for the two cases studied. It should be noted that the heat transfer coefficient mentioned in the film boiling section is defined as:

$$q'' = h_t(T_{w,in} - T_s), \tag{2-4}$$

where $q''$ is the heat flux (W/m$^2$); $h_t$ the heat transfer coefficient (W/m$^2$-K); $T_{w,in}$ the wall temperature of the inner wall surface (ºC); $T_s$ the saturation temperature (ºC).

(c) Test section power calculation

Table 2.8 shows the bottom hot patch power, top hot patch power and film boiling section power needed at the mass flux of 2,000 kg/m$^2$-s, and inlet subcooling of 50 ºC at different pressures. As can be seen, the total power needed for the film boiling tests increases with the increase of the pressure at the mass flux of 2,000 kg/m$^2$-s and inlet subcooling of 50 ºC.

Table 2.8. Test section power calculation

| Pressure (psi) | Bottom hot patch | | Top hot patch | | Film boiling section | | | Total power (W) |
|---|---|---|---|---|---|---|---|---|
| | Voltage (V) | Power (W) | Voltage (V) | Power (W) | Heat flux (kW/m$^2$) | Voltage (V) | Power (W) | |
| 20 | 0.558 | 979 | 0.617 | 1197 | 250 | 9.005 | 10171 | 12347 |
| 100 | 0.629 | 1244 | 0.55 | 951 | 300 | 9.864 | 12205 | 14400 |
| 300 | 0.685 | 1475 | 0.472 | 701 | 400 | 11.390 | 16273 | 18449 |
| 500 | 0.683 | 1467 | 0.402 | 508 | 520 | 12.987 | 21155 | 23131 |
| 600 | 0.672 | 1420 | 0.37 | 430 | 550 | 13.356 | 22376 | 24227 |
| 800 | 0.662 | 1378 | 0.332 | 347 | 600 | 13.950 | 24410 | 26135 |
| 1,000 | 0.631 | 1252 | 0.364 | 417 | 720 | 15.282 | 29292 | 30961 |

According to the calculated power values needed for different conditions in Table 2.8, the test section design power, including the bottom hot patch power, top hot patch power, and film boiling

section power, is determined as shown in Table 2.9. The DC power supplies at the bottom and top hot patches are both designed to be 2 kW and that at the film boiling section is designed to be 30 kW. As can be seen, the required voltage is small, but the electric current is very large. Since the film boiling section is much longer than the bottom and top hot patch sections as shown in Table 2.2, the electric current in the film boiling section is smaller, despite the larger voltage than that at the bottom and top hot patch sections.

Table 2.9. Test section design power

| **Items** | **Bottom hot patch** | **Top hot patch** | **Film boiling section** |
|---|---|---|---|
| Power (kW) | 2 | 2 | 30 |
| Maximum voltage (V) | 0.8 | 0.8 | 15.4 |
| Maximum current (A) | 2507.8 | 2507.8 | 1941.8 |

2.4.3 Thermal analysis in the ISFB regime

Figure 2.21 shows the wall temperature distributions along the axial direction at pressures of 100 and 500 psi, mass flux of 1,000 kg/m$^2$-s and inlet subcooling of 10 °C. At the pressure of 100 psi, mass flux of 1,000 kg/m$^2$-s, and inlet subcooling of 10 °C, the wall temperature decreases along the axial direction. This is because the promoting effect of the quality on the heat transfer coefficient is dominant. The vapor quality in the ISFB regime is higher than that in the IAFB regime. With a higher quality, the vapor velocity is higher, leading to strong turbulence and mixing in the vapor film, further promoting the heat transfer coefficient in the ISFB regime.

At the pressure of 500 psi, mass flux of 1,000 kg/m$^2$-s, and inlet subcooling of 10 °C, the wall temperature increases first and then decreases along the axial direction, which indicates that the

effects of the quality on the wall temperature is complex and in fact, the wall temperature distributions are also related to the pressure, mass flux, and inlet subcooling. It should be noted that at the pressure of 500 psi, mass flux of 1,000 kg/m$^2$-s and inlet subcooling of 10 °C, the maximum wall temperature is near 1400 K, higher than the maximum allowable temperature for the Incoloy 800 H/HT at 500 psi per the ASME code, i.e., 1107 K (ASME, 2010). Although the test section power can meet the ISFB requirements, the wall temperature is excessively high. Therefore, in the actual tests, the wall temperature will be carefully monitored.

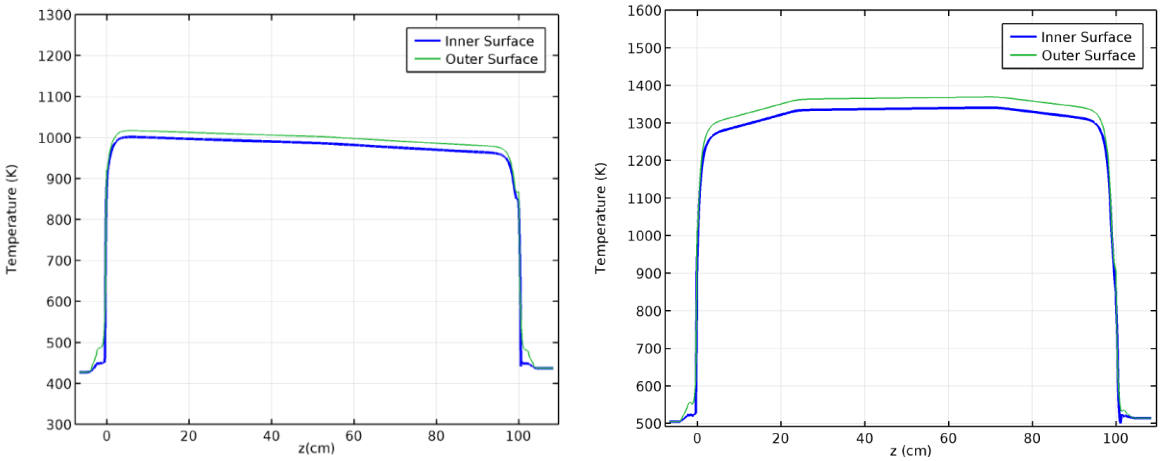


(a) (b)

Figure 2.21 Wall temperature distribution along the axial direction at mass flux of 1,000 kg/m$^2$-s and inlet subcooling 10 °C at the water pressures of (a) 100 psi and (b) 500 psi

### 2.4.4 Effects of thermal insulation thicknesses

In the COMSOL simulations presented in the previous sections, natural convection heat transfer mode is assumed between the outer surface of the insulation and the environment, and the natural convection heat transfer coefficient is assumed to be constant, namely 10 W/m$^2$-K, for simplification. However, effects of the insulation thicknesses on the heat loss to the ambient and

the temperature distributions of the outer surface of the insulation are closely related to the natural convection heat transfer coefficient. Therefore, iterative calculations need to be performed to obtain more accurate calculations of the natural convection heat transfer coefficient and therefore the heat loss from the test section to the ambient air. The subsection describes these calculations for obtaining the heat loss from the test section to the ambient air with different insulation thickness values.

(a) Natural convection heat transfer coefficient

The natural convection heat transfer coefficient on the outer surface of the PCHT test section with the thermal insulation is calculated by the correlation in Ref. (Holman, 1986). All the air thermal and transport properties are determined based on the film temperature ($T_m$). On the inner surface of the Incoloy 800H/HT test section tube, convective and nucleate boiling heat transfer modes are assumed for the bottom hot patch section, and film boiling is assumed for the rest of the test section. Table 2.10 shows the calculated natural convection heat transfer coefficients on the outer surface of the test section with two different insulation (microporous insulation) thicknesses, i.e., 20 and 50 mm, at the following flow condition: water pressure 500 psi, mass flux 2,000 kg/m$^2$-s, inlet subcooling 50 ºC, and air ambient temperature 20 ºC. $T_{w,m}$ refers to the average temperature on the outer surface of the test section tube and 67 and 30 ºC are assumed in the two calculations. The calculated natural convection heat transfer coefficients for the two different values of the insulation thickness are smaller than the assumed value used in the previous COMSOL simulations, i.e., 10 W/m$^2$-K.

Table 2.10. Calculated natural convection heat transfer coefficients

| Insulation thickness (mm) | 20 | 50 |
|---|---|---|
| $T_{w,m}$ (°C) | 67 | 30 |
| $T_m$ (°C) | 43.5 | 25 |
| $\alpha_v$ (1/K) | 0.00316 | 0.00335 |
| $v$ ($\times 10^{-5}$ m$^2$/s) | 1.17 | 1.55 |
| $a$ ($\times 10^{-5}$ m$^2$/s) | 2.48 | 2.22 |
| $k$ ($\times 10^{-2}$W/m-K) | 2.92 | 2.63 |
| Pr | 0.691 | 0.701 |
| Gr | $7.53\times10^9$ | $2.07\times10^9$ |
| Nu | 180 | 115 |
| $h$ (W/m$^2$-K) | 4.57 | 2.63 |

To obtain more accurate results, following iterative calculations are performed. The calculated natural convection heat transfer coefficient shown in Table 2.10 is first used in the next COMSOL simulation as an initial estimate to obtain the outer surface temperature of the insulation until the differences of the insulation surface temperature and natural convection heat transfer coefficient between the two immediate iterative calculations become small enough. The iteration process is shown in Table 2.11. From Iterations 2 to 3, the outer wall temperatures of the test section tube get closer for the 50-mm thick case and therefore 2.18 W/m$^2$-K is used as the natural convective heat transfer coefficient for this case. For the 20-mm insulation thickness case, from Iterations 3 to 4, the outer wall temperature calculation is converged. For the current heat loss calculations, the convective heat transfer coefficients given after the third iteration for the 50-mm thick case and the fourth iteration for the 20-mm thick case were used in estimating the heat loss from the test section.

Table 2.11. Iterative computation

| Iteration number | Insulation thickness (mm) | 20 | 50 |
|---|---|---|---|
| 1 | $T_{w,m}$ (ºC) | **67** | **30** |
| | $T_m$ (ºC) | 43.5 | 25 |
| | $h$ (W/m$^2$-K) | 4.57 | 2.63 |
| 2 | $T_{w,m}$ (ºC) | **115** | **26** |
| | $T_m$ (ºC) | 67.5 | 23 |
| | $h$ (W/m$^2$-K) | 5.30 | 2.35 |
| 3 | $T_{w,m}$ (ºC) | **106** | **27** |
| | $T_m$ (ºC) | 63 | 23.5 |
| | $h$ (W/m$^2$-K) | 5.16 | 2.18 |
| 4 | $T_{w,m}$ (ºC) | **107** | -- |
| | $T_m$ (ºC) | 63.5 | -- |
| | $h$ (W/m$^2$-K) | 5.18 | -- |

(b) Temperature distributions on the insulation surface

Figure 2.22 and Figure 2.23 show the wall temperature distributions on the insulation outer surface with the two different insulation thicknesses at water pressure of 500 psi, mass flux of 2,000 kg/m$^2$-s, and inlet subcooling of 50 °C. From Figure 2.22, it can be seen that with the insulation thickness being 20 mm, the outer surface temperature of the insulation can be up to 107 ºC at the film boiling section. The temperature spikes are due to the thinner insulation and heat flux spikes at the electrodes. The electrode disks have an outer diameter of 40 mm and the test section tube outer diameter is 19.05 mm. The actual thicknesses of the thermal insulation at the electrodes will be only about 9.5 and 39.5 mm for the two cases where the insulation for the test section tube is 20 and 50 mm, respectively. In Figure 2.23, with the insulation thickness increased to 50 mm, the outer surface temperatures of the insulation are much lower than those with the thinner thermal insulation.

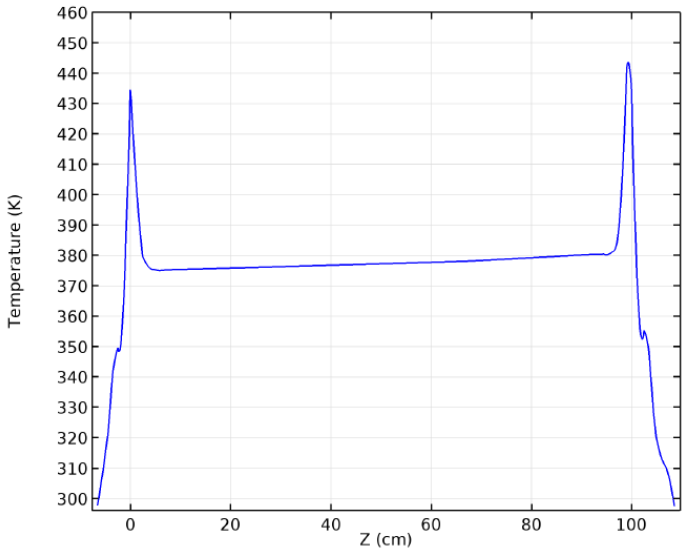


Figure 2.22 Temperature distributions on the insulation outer surface with the insulation thickness being 20 mm

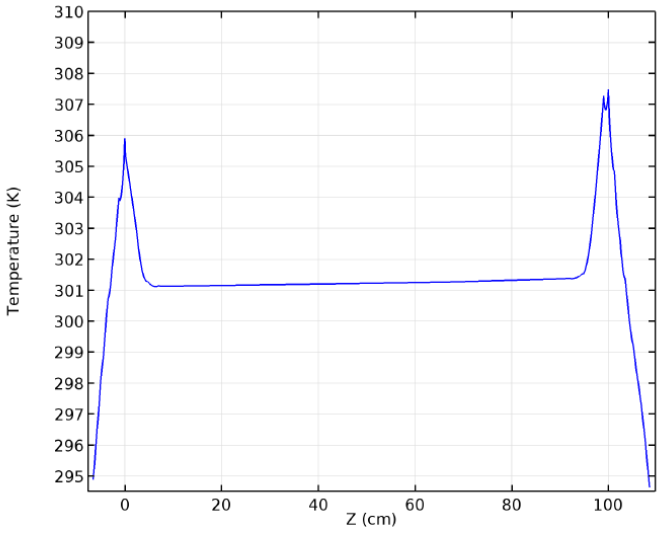


Figure 2.23 Temperature distributions on the insulation outer surface with the insulation thickness being 50 mm

(c) Heat loss

In the COMOSL calculations, the heat losses from the insulation surface to the ambient air and heat transferred to the water and vapor in the test section are calculated by integrating the wall heat flux over the test section. Table 2.12 shows the results with two different insulation thicknesses for the same flow condition: water pressure of 500 psi, mass flux of 2,000 kg/m$^2$-s, and inlet subcooling of 50 ºC. The heat loss with the insulation thickness of 20 mm is larger than that of 50 mm and their percentages in the total heating power are both small.

Table 2.12. Heat loss calculations

| Insulation thickness (mm) | Heat loss (W) | Heat to water and vapor in the test section (W) | Total heating power (W) | Percentage of heat loss (%) |
|---|---|---|---|---|
| 20 | 60.95 | 23,804.4 | 23,865.4 | 0.255 |
| 50 | 5.34 | 23,782.0 | 23,787.4 | 0.022 |

Based on the above calculations and analysis of the effects of the insulation thicknesses on the temperature distributions and heat loss, the thermal insulation could be designed to be 20 mm since the calculated heat loss is less than 1% of total heating power. However, as shown in Figure 2.22, the outer surface temperature of the insulation can exceed 100 ºC, which may not be desirable. On the other hand, a thicker thermal insulation will, to some degree, affect the X-ray radiography system performance. Currently, we choose the insulation thickness to be 25 mm based on the commercial availability of the insulation.

2.4.5 Effects of electrode thickness on the heat flux distribution

To study the effects of the electrode thickness on the heat flux distribution, the thicknesses of the electrodes at Points A, C and D shown in Figure 2.18 are assumed to be 1.5, 3, 3.5, 4, 5, and 10 mm while the thickness of the electrode at Point B remains as 1.5 mm since it affects the position of the bottom quench front. Figure 2.24 shows the heat flux distribution calculated by COMSOL Multiphysics code for the flow conditions with the water pressure of 100 psi, mass flux of 2,000 $kg/m^2$-s, and inlet subcooling of 50 ºC with the electrodes at Points A, C and D being 1.5 mm thick and Figure 2.25 to Figure 2.29 show the heat flux distributions with the electrodes at Points A, C and D being 3, 3.5, 4, 5, and 10 mm thick for the same flow conditions.

With the 1.5, 3, and 3.5-mm thickness for the electrodes at Points A, C and D in Figure 2.24 to Figure 2.26, there are two small heat flux peaks at Points A and D, and two large heat flux peaks at Points B and C. As shown in Figure 2.27 to Figure 2.29, with the 4, 5, and 10-mm thickness for the electrodes at Points A, C and D, the two large heat flux peaks can be seen at Points B and C, while the two small heat flux peaks disappeared at Points A and D. Furthermore, the peak heat flux value at Points B does not change significantly while the peak heat flux value at Point C decreases slightly with the increased electrode thickness. At the top and bottom notches, the notch temperatures are kept at 800 K by the PID controllers. In this case, the control mechanism depends on the heat generation rate. Although the electric resistance is smaller with a thicker electrode, the electric current will be larger to keep the notch temperature at the set value. Therefore, the heat flux at Point C remains large with a thicker electrode. However, the effect of increasing the electrode thickness for Points A and D on reducing the local heat flux spikes is clearly observed.

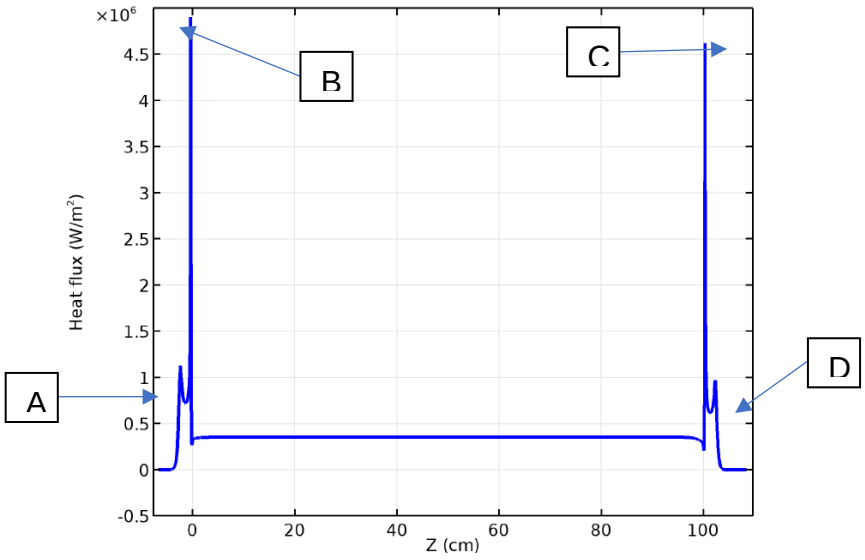


Figure 2.24. Heat flux distribution at water pressure of 100 psi, mass flux of 2,000 kg/m$^2$-s, and inlet subcooling of 50 ºC with all the four electrodes being 1.5 mm thick

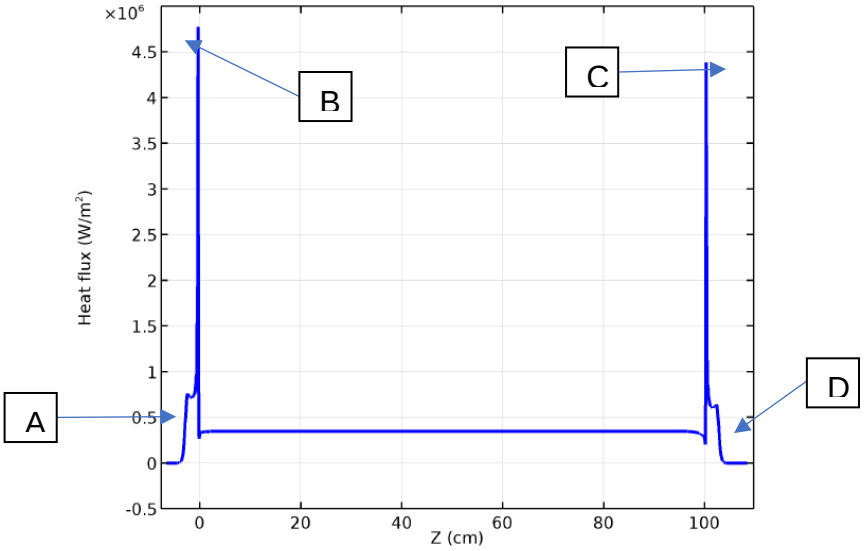


Figure 2.25. Heat flux distribution at water pressure of 100 psi, mass flux of 2,000 kg/m$^2$-s, and inlet subcooling of 50 ºC with the electrodes at Points A, C, and D being 3 mm thick (Point B remains at 1.5 mm thick)

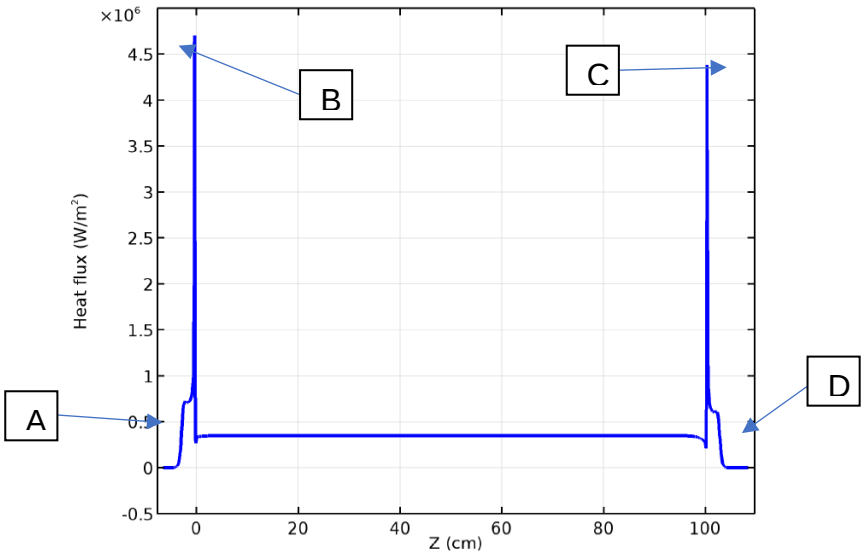


Figure 2.26. Heat flux distribution at water pressure of 100 psi, mass flux of 2,000 kg/m$^2$-s and inlet subcooling of 50 ºC with the electrodes at Points A, C, and D being 3.5 mm thick (Point B remains at 1.5 mm thick)

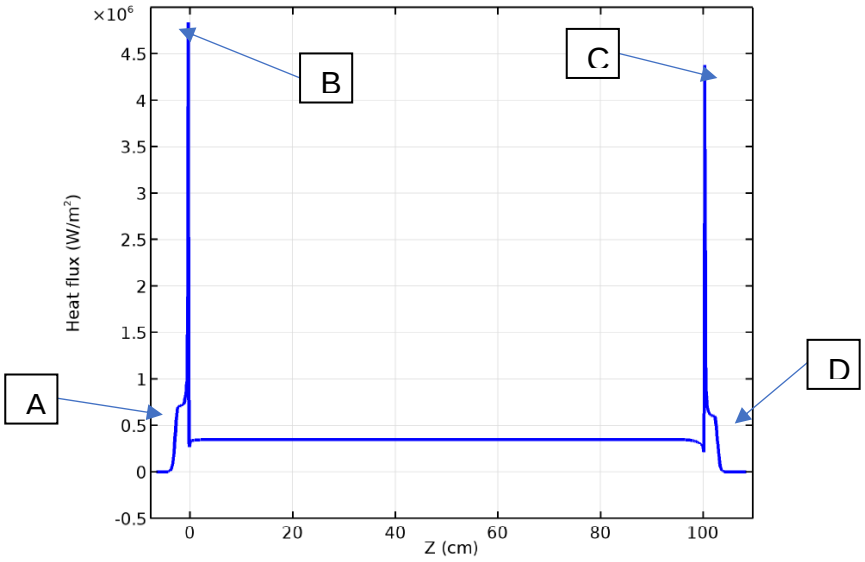


Figure 2.27. Heat flux distribution at water pressure of 100 psi, mass flux of 2,000 kg/m$^2$-s and inlet subcooling of 50 ºC with the electrodes at Points A, C, and D being 4 mm thick (Point B remains at 1.5 mm thick)

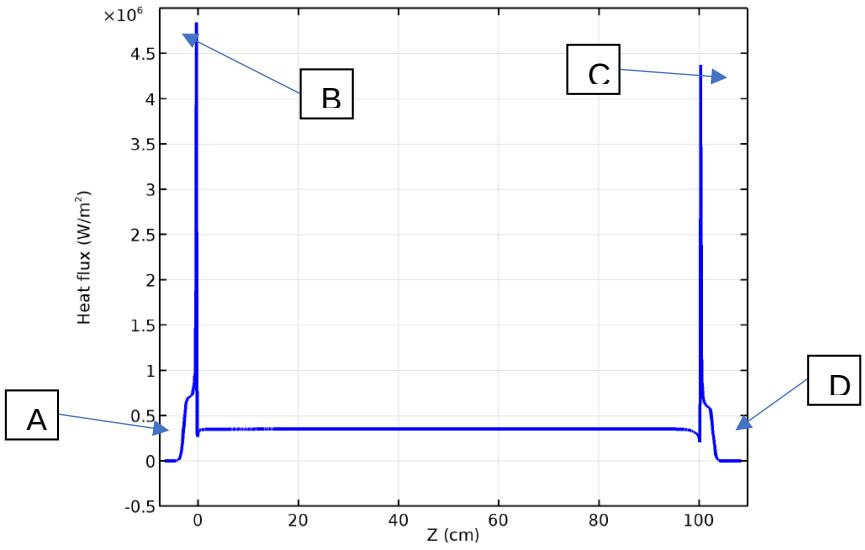


Figure 2.28. Heat flux distribution at water pressure of 100 psi, mass flux of 2,000 kg/m$^2$-s and inlet subcooling of 50 ºC with the electrodes at Points A, C, and D being 5 mm thick (Point B remains at 1.5 mm thick)

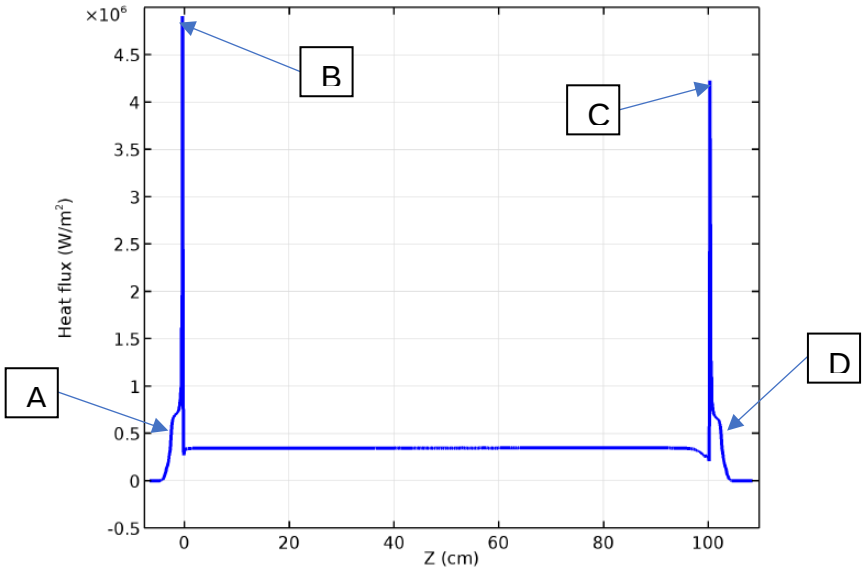


Figure 2.29. Heat flux distribution at water pressure of 100 psi, mass flux of 2,000 kg/m$^2$-s and inlet subcooling of 50 ºC with the electrodes at Points A, C, and D being 10 mm thick (Point B remains at 1.5 mm thick)

From Figure 2.24 to Figure 2.29, the electrode thickness for Points A, C and D does not appear to have significant influence on the heat flux distribution in the entire test section, especially in the film boiling section (Section BC). Increasing the electrode thickness for Points A and D can reduce or remove the local heat flux spikes. However, if the thickness of the electrode is too long, it will increase the length of the preheater section. At present, the electrode thickness at Points A, C and D is preliminarily designed to be 4 mm and that at Point B 1.5 mm. To confirm that the designed electrode thickness would work well for higher pressure conditions, Figure 2.30 shows the heat flux distribution for the flow condition with the water pressure of 1,000 psi, mass flux of 2,000 kg/m$^2$-s and inlet subcooling of 50 ºC with the electrodes at Points A, C and D being 4 mm thick (The electrode thickness at Point B remains 1.5 mm). It can be observed that the heat flux spikes at Point A and D are removed.

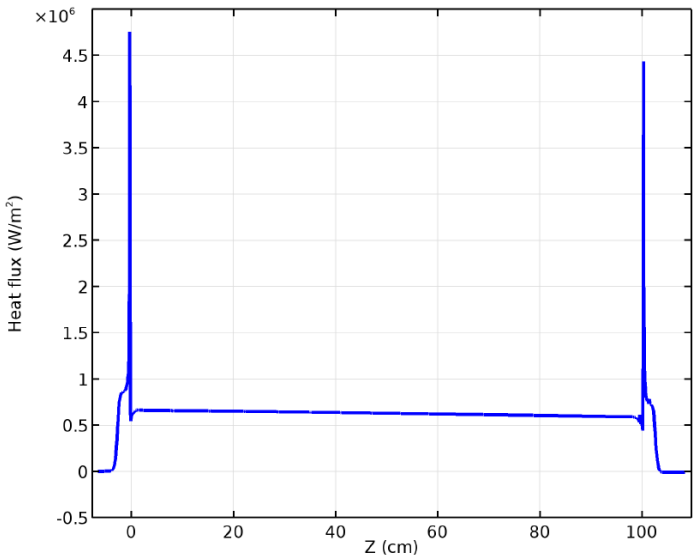


Figure 2.30 Heat flux distribution at water pressure of 1,000 psi, mass flux of 2,000 kg/m$^2$-s and inlet subcooling of 50 ºC with the electrodes at Points A, C and D being 4 mm thick (Point B remains at 1.5 mm thick)

### 2.4.6 Length of the top hot patch section on the heat flux distribution

To study the effects of the length of the top hot patch section (Section CD in Figure 2.18), its length is varied from its original design value of 25 mm to a larger value of 50 mm. Again, Figure 2.27 shows the heat flux distribution for the flow condition with water pressure of 100 psi, mass flux of 2,000 kg/m$^2$-s, and inlet subcooling of 50 ºC with the thickness of the electrodes at Points A, C and D being 4 mm (The electrode at Point B remains at 1.5 mm thick) and the length of the CD section being 25 mm. Figure 2.31 shows the heat flux distribution for the same flow condition and same electrode thickness but an increased length of the CD section being 50 mm. From the COMSOL calculations, the value of the heat flux at the CD section in Figure 2.27 is similar to that in Figure 2.31. Therefore, increasing the length of the CD section does not seem to significantly affect the heat flux distribution in that section, but provides more working space in that section for attaching the electrodes and thermocouples to the test section. However, this increased length will increase the insertion length of the RTD for measuring the liquid core temperature at the location below Point C and may lead to increased vibration of the temperature measurement device. Therefore, the length of the top hot patch is kept as 25 mm.

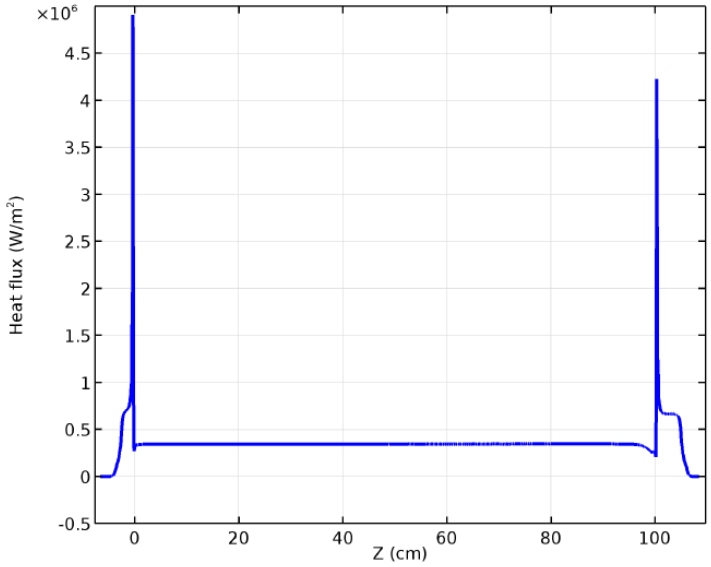


Figure 2.31 Heat flux distribution for the flow condition of water pressure of 100 psi, mass flux of 2,000 kg/m$^2$-s, and inlet subcooling of 50 ºC with the electrode thickness at Points A, C and D being 4 mm (1.5 mm for Point B) and length of the CD section being 50 mm

## 2.5 Instrumentation

### 2.5.1 Temperature measurements in the flow loop

Six thermocouples are inserted into the pressurizer to monitor the water and steam temperatures. Based on the temperature measurements and the pressure measurement in the pressurizer, the heating power in the pressurizer can be adjusted to maintain the system pressure. Ten thermocouples are inserted into the reservoir tank to monitor the water temperature. The water temperature in the tank is kept close to the required inlet temperature of the test section. The tank has a total storage capacity of approximately 114 liters, so it can provide a sufficient thermal buffer to stabilize the test section inlet temperature. The temperature at the outlet of the pre-cooler is

measured to ensure that it is below the water saturation temperature by a certain margin to avoid any cavitation in the pump. If the inlet temperature of the pre-cooler is below the inlet temperature of the test section, the cooling water will be turned off and the pre-cooler be disabled. The pre-heater is the final device to adjust the water temperature before the test section, so it is very important to monitor the outlet temperature of the pre-heater. The power of the pre-heater should be adjusted to ensure that the outlet temperature of the pre-heater is equal to or slightly higher than the required inlet temperature of the test section. The temperature at the outlet of the condenser is measured. The cooling water is adjusted to keep the outlet temperature of the condenser close to the required inlet temperature of the test section.

### 2.5.2 Temperature measurements on the test section

The temperature measurement can be divided into two groups for monitoring the water temperatures and measuring the outer surface temperatures of the test section. Two resistance temperature detectors (RTDs) with good measurement accuracy are inserted into the inlet and outlet of the test section to measure the inlet and outlet fluid temperature. A third RTD is inserted from the top of the test section to measure the temperature of the liquid core in the IAFB regime near the end of the heated length. The temperature of the water core in the IAFB regime will provide useful information in reducing the experimental data to obtain the liquid-side interfacial heat transfer coefficient.

The outer surface temperatures of the test section are measured at 17 elevations using 17 K-type sheathed but ungrounded thermocouples attached to the test section using microscopic laser

welding technique and/or an infrared (IR) thermometer. Four thermocouples are installed at the bottom and top notches, respectively, to measure the notch temperatures. Figure 2.32 and Table 2.13 show the thermocouple distribution along the vertical test section.

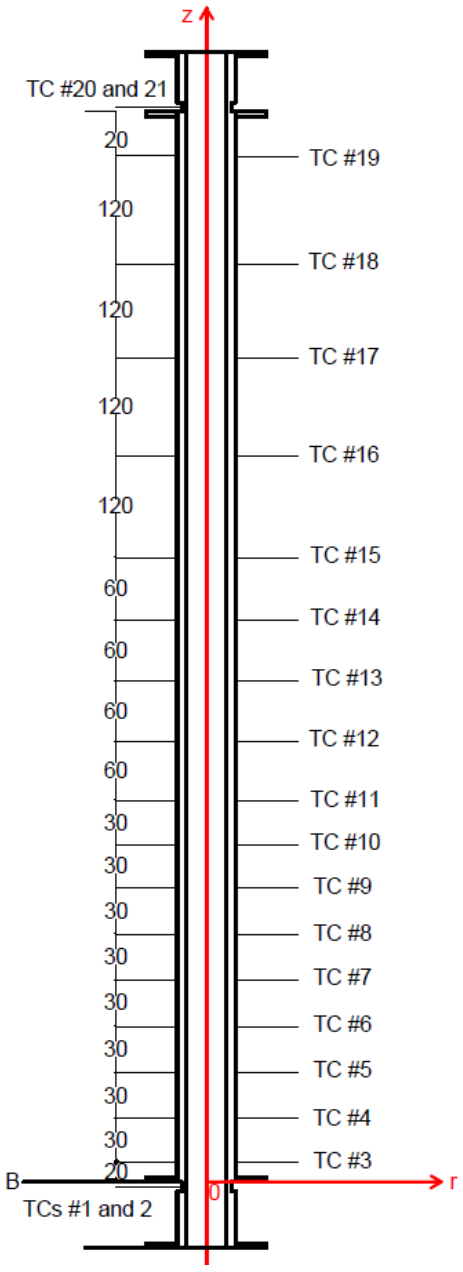


Figure 2.32 Schematic of the thermocouple distribution along the vertical test section (Not scaled. Length unit: mm)

Table 2.13. Thermocouple distributions along the vertical test section tube wall

| Section | TC # | Distance from Point B* (mm ) | Intervals (mm) |
|---|---|---|---|
| Bottom notch | 1 | -1.5 | - |
| Film boiling section | 2 | 20 | 21.5 |
| | 3 | 50 | 30 |
| | 4 | 80 | 30 |
| | 5 | 110 | 30 |
| | 6 | 140 | 30 |
| | 7 | 170 | 30 |
| | 8 | 200 | 30 |
| | 9 | 230 | 30 |
| | 10 | 260 | 30 |
| | 11 | 320 | 60 |
| | 12 | 380 | 60 |
| | 13 | 440 | 60 |
| | 14 | 500 | 60 |
| | 15 | 620 | 120 |
| | 16 | 740 | 120 |
| | 17 | 860 | 120 |
| | 18 | 980 | 120 |
| | 19 | 1001.5 | 21.5 |
| Top notch | 20 | -1.5 | - |

*: B is at the top edge of the bottom notch

To make sure that the attached thermocouples work properly, a benchmark test is performed. Four thermocouples of the same design are attached, by the same laser welding technique, to the outer surface of four test section samples, i.e., TCs # A, B, C, and D as shown in Figure 2.33, and the samples are placed in a high-temperature furnace (up to 700 ºC). Their readings are compared with a reference thermocouple. Figure 2.34 shows the comparisons between the attached thermocouples and the reference thermocouple, which show that these four attached thermocouples function reasonably as expected, with an average difference of 2 ºC with the reference thermocouple at 700 ºC.

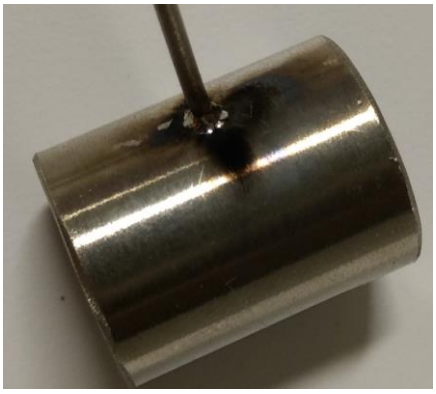

(a) TC #A

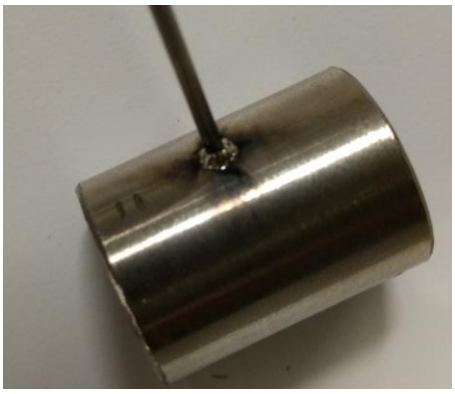

(b) TC #B

(c) TC #C

(d) TC #D

Figure 2.33 Thermocouples attached on tube samples by the laser welding technique

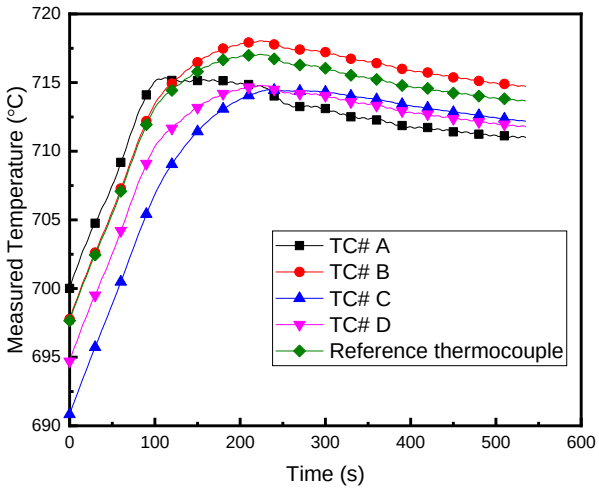


Figure 2.34 Comparisons between the attached thermocouples and the reference thermocouple

### 2.5.3 Flow rate measurements

The water flow rate is measured by two turbine flowmeters with ranges of 1.0 to 10 LPM, and 3.6 to 36 LPM. From the calibration data of the flowmeter, its measurement accuracy is 0.25%. The expected volumetric flow rate to be covered in the experiments is 1.1 to 21.4 LPM (0.31 to 5.63 GPM) corresponding to a mass flux range from 150 to 2000 $kg/m^2$-s in the test section (of a 3/4-inch tube with the thickness of 0.12 inch). These two flowmeters are installed in parallel downstream of the pump.

### 2.5.4 Pressure measurements

The absolute pressure at the outlet of the test section and in the pressurizer are measured by two absolute pressure transducers installed at the outlet of the test section and in the top section of the pressurizer, respectively. The pressure difference across the test section is measured by a differential pressure transducer. The water level in the pressurizer is measured by a second differential pressure transducer. The measurement accuracy of the absolute pressure transducer is 0.065% of the span. The measurement range of the differential pressure transducer can be adjusted in the range of -400 to 400 in$H_2O$ and its accuracy is 0.05% of the span.

### 2.5.5 Void fraction and flow topology measurements

The void fraction is measured by a gamma densitometer and an X-ray radiography system (Adams et al., 2017). The flow topology is measured by this X-ray radiography system. The basic principle

of photon attenuation is that the intensity of photon beam decreases exponentially as it goes through matters. In the PCHT test section, the photon attenuation principle can be applied to situations where gas-liquid two-phase flows are encountered in the test section as:

$$I(\alpha) = I_0 \exp\ \left[-2\mu_{ins} t_{ins} - 2\mu_w t_w - \left[\alpha\mu_g + (1-\alpha)\ \mu_f\right] D\right] , \tag{2-5}$$

where $I_0$ is the source intensity (#/cm$^2$-s); $\alpha$ the line-averaged void fraction; $I(\alpha)$ the intensity at void fraction $a$ (#/cm$^2$-s); $\mu_{ins}$ the linear attenuation coefficient of the insulation (cm$^{-1}$); $\mu_w$ the linear attenuation coefficient of the tube wall (cm$^{-1}$); $\mu_g$ the linear attenuation coefficient of steam (cm$^{-1}$); $\mu_f$ the linear attenuation coefficient of water (cm$^{-1}$); $t_{ins}$ the thickness of the insulation (cm); $t_w$ the thickness of the tube wall (cm); and $D$ the inner diameter of the tube (cm). Since the count rate, which can be obtained by a detector, is proportional to the photon intensity, the void fraction can be expressed as a function of count rates for pure vapor (void fraction being 1.0), pure liquid (void fraction being 0.0), and two-phase mixture (void fraction between 0.0 and 1.0) as:

$$I(0) = I_0 \exp\left\{-2\mu_{ins} t_{ins} - 2\mu_w t_w - \mu_f D\right\}, \tag{2-6}$$

$$I(1) = I_0 \exp\left\{-2\mu_{ins} t_{ins} - 2\mu_w t_w - \mu_g D\right\}, \tag{2-7}$$

$$\alpha = \frac{\ln\left[I(0)/I(\alpha)\right]}{\ln\left[I(0)/I(1)\right]}. \tag{2-8}$$

where $I(0)$ is the intensity at void fraction 0 (#/cm$^2$-s); and $I(1)$ the intensity at void fraction 1 (#/cm$^2$-s). The standard deviation of the void fraction can be obtained based on propagation principle as:

$$\sigma_{\alpha} = \sqrt{\left[\frac{\partial \alpha}{\partial I(\alpha)}\right]^2 \sigma_{I(\alpha)}{}^2 + \left[\frac{\partial \alpha}{\partial I(1)}\right]^2 \sigma_{I(1)}{}^2 + \left[\frac{\partial \alpha}{\partial I(0)}\right]^2 \sigma_{I(0)}{}^2}, \tag{2-9}$$

where $\sigma_{I(\alpha)}$ is the standard deviation of the intensity at void fraction $a$ (#/cm$^2$-s); $\sigma_{I(1)}$ the standard deviation of the intensity at void fraction 1 (#/cm$^2$-s); and $\sigma_{I(0)}$ the standard deviation of the intensity at void fraction 0 (#/cm$^2$-s);. For the X-ray radiography system, the statistical uncertainty of the mean void fraction is calculated as:

$$\sigma_{\bar{\alpha}} = \frac{\sigma_{\alpha}}{\sqrt{N}}, \tag{2-10}$$

where $N$ is the measurement time. As can be seen in Eq. (2-10), the statistical uncertainty of the mean void fraction will decrease as the measurement time increases. For the gamma densitometer, the statistical uncertainty of count rate is calculated as:

$$\sigma_{\bar{I}} = \sqrt{\frac{I}{2\tau}}, \tag{2-11}$$

where $\tau$ is the time constant of the RC-filters (s), which can be set manually in the gamma densitometer. The larger the time constant is, the smaller the statistical uncertainty of the count rate is. The statistical uncertainty of the mean void fraction measured by the gamma densitometer can be obtained by inserting Eq. (2-11) into Eq. (2-9). To obtain the cross-sectional-averaged void fraction from the X-ray radiography system, the integration of the line-averaged void fraction is performed as:

$$\bar{\alpha}_{cross} = \frac{1}{A}\sum_{i=1}^{N} \alpha_i A_i. \tag{2-12}$$

The standard deviation of cross-sectional-averaged void fraction can be calculated based on propagation principle as:

$$\sigma_{\bar{\alpha}_{cross}} = \frac{1}{A}\sqrt{\sum_{i=1}^{N}\left(\sigma_{\alpha_i}{}^2 A_i^2\right)}. \tag{2-13}$$

If air is used in the calibration tests to obtain $I(1)$ and steam and water exist in the two-phase flow, the measured void fraction can be corrected by:

$$\alpha_{corr} = \frac{\ln\left[I(0)/I(\alpha)\right]}{\ln\left[I(0)/I(1)\right]} \cdot \frac{1-\left(\mu\cdot\rho\right)_{air}/\left(\mu\cdot\rho\right)_{water}}{1-\rho_{steam}/\rho_{water}}. \tag{2-14}$$

The gamma densitometer, including a gamma source, a detector, and electronic unit, has been installed in the custom designed traversing system as shown in Figure 2.35. The UM staff from Department of Environment, Health & Safety (EHS) and the engineer from the vendor, i.e., Berthold Technologies, performed some radiation survey to ensure the safety of the installation. In addition, the engineer from the vendor performed leak tests, inspected the installation, and checked the setup of the evaluation unit of the gamma densitometer.

The X-ray radiography system includes an X-ray tube, a detector, and control system. The spatial resolution of the detector is 0.1 mm. Figure 2.36 shows the schematic of the X-ray radiography system. The working time of the X-ray tube is less than 1 second for each shot. The X-ray tube and detector are synchronized to make sure that the detector can capture the images when the X-ray tube is shooting. Figure 2.37 shows the installation of the X-ray radiography system.

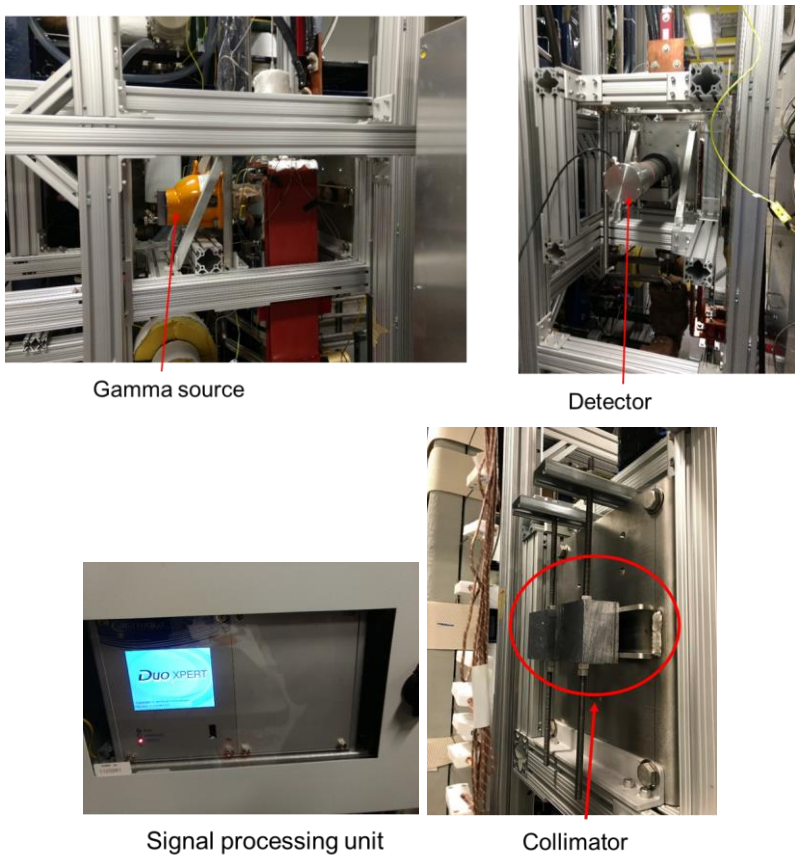


Figure 2.35 Installation of the gamma densitometer in the traversing system

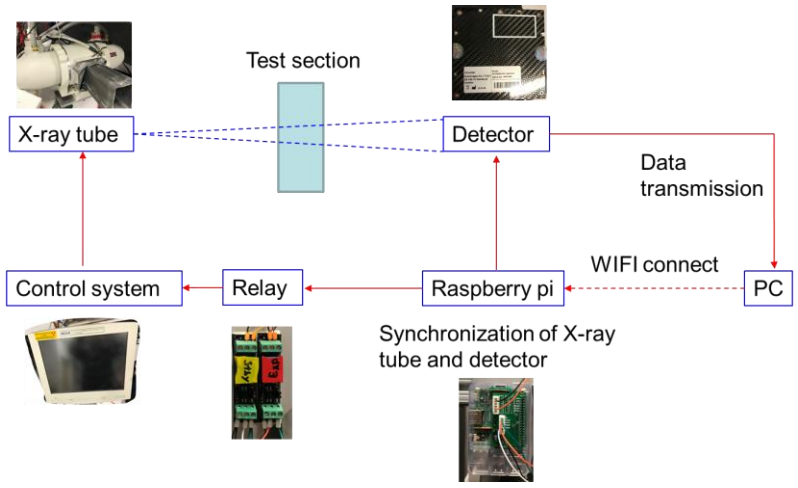


Figure 2.36 Schematic of the X-ray radiography system

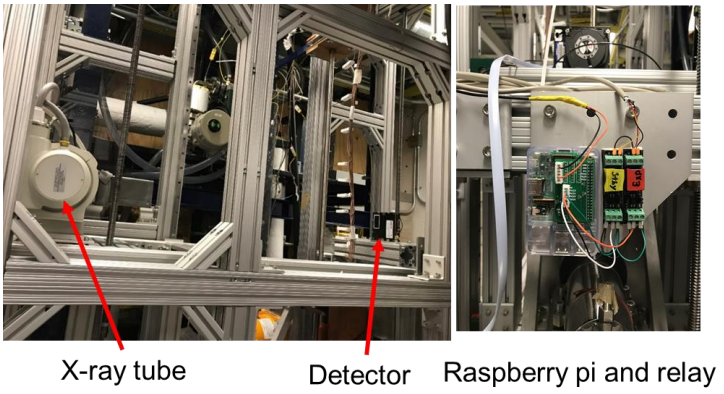


Figure 2.37 Installation of the X-ray radiography system

To protect the personnel from the X-ray radiation, concrete blocks are built up against the west-side lab wall (drywall) and four lead-lined plywood panels are put on the concrete blocks. The lead-lined plywood panels were anchored on wood structures attached to the wall as shown in Figure 2.38. The UM team and the staff from EHS at UM have tested the dose rate from the X-ray radiography system and the results show that the shielding in Figure 2.38 is sufficient to reduce the dose rate to a safe level.

Figure 2.38 Concrete blocks and lead-lined plywood panels for the X-ray radiography system

As shown in Figure 2.39, a platform was designed to vertically lift these two instruments, the X-ray radiography system and the gamma densitometer, along the test section so that the void fraction and flow topology can be measured at different elevations. The platform consists of two screw jacks, a gearbox, a servo motor, four linear rails, and T-slotted frames. These two instruments will be moved vertically up and down along four linear trails by two screw jacks and the servo motor. Figure 2.40 shows the dimensions of the traversing platform. Figure 2.41 shows the dimension of the screw jack assembly. The length of the stroke on the screw jack is 1,900 mm.

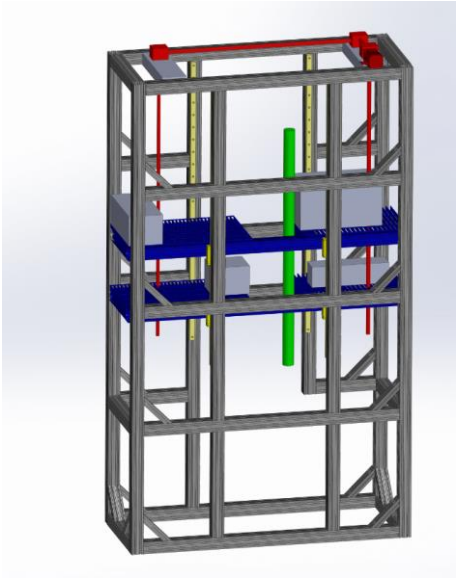

Figure 2.39 Platform to traverse the X-ray radiography system and gamma densitometer

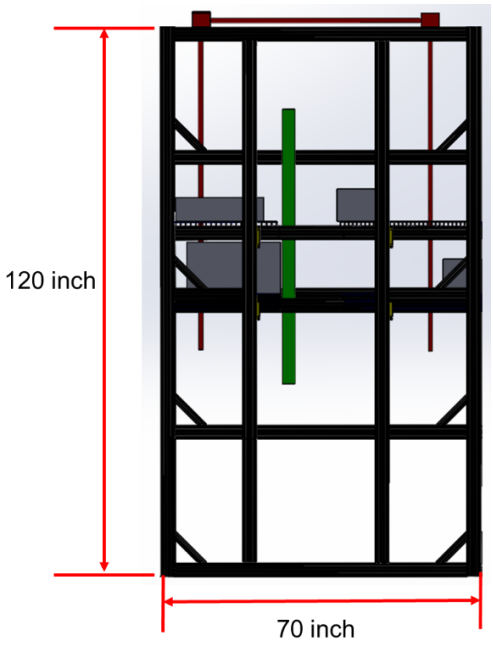


(a) Front view

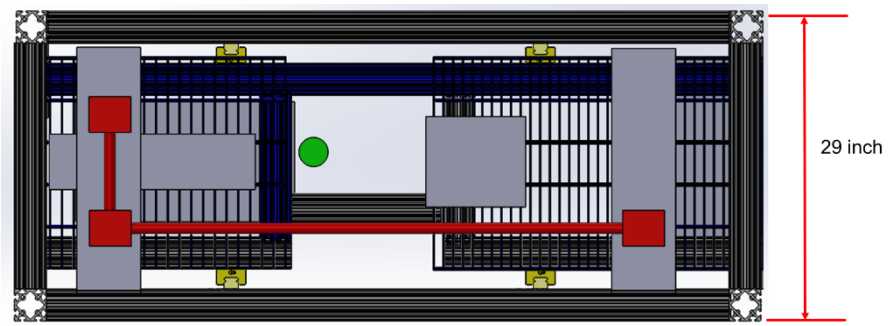


(b) Top view

Figure 2.40 Dimensions of the traversing platform

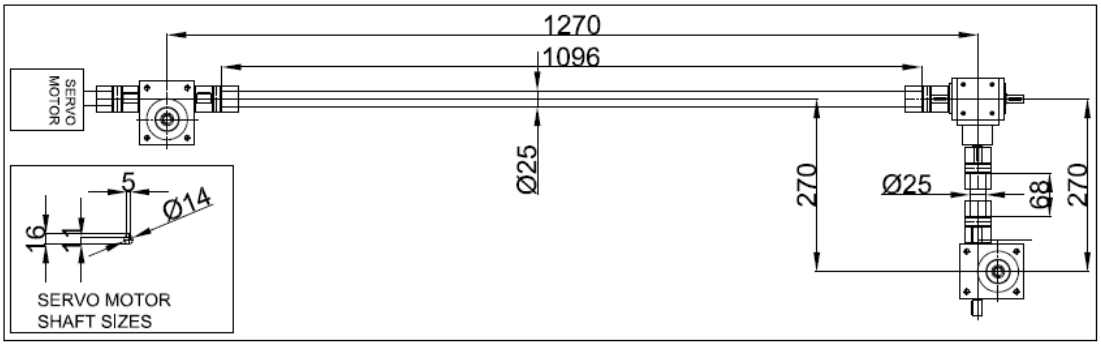


Figure 2.41 Dimensions of the screw jack assembly (Unit: mm)

A photo of the traversing platform is shown in Figure 2.42 and Figure 2.43. Two screw jacks, four linear rails, and two platforms to accommodate the X-ray radiography system and gamma densitometer have been installed on the T-slot beam structure. The servo motor is connected to the screw jack and wired to the power supply, and the platform has been tested. The rated speed of the motor is 1,500 RPM. Currently, the motor is tested at a speed of 150 RPM and the platform lifting speed is 30 mm /min.

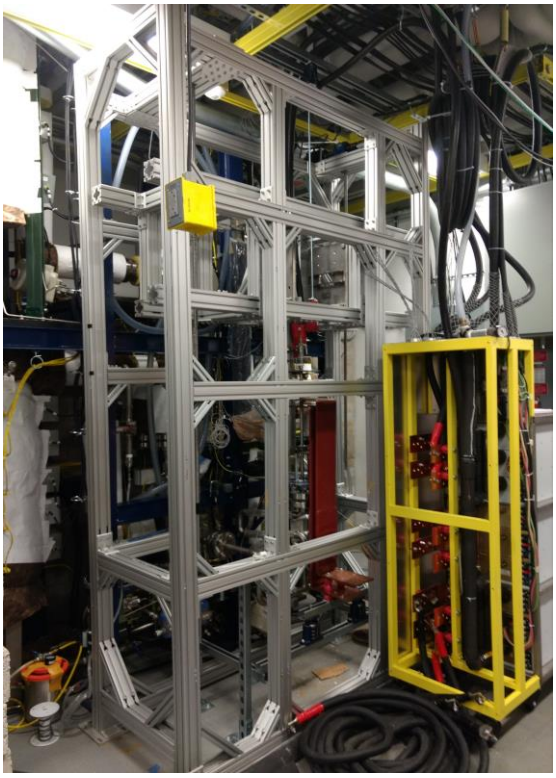

Figure 2.42  Platform to traverse the X-ray radiography system and gamma densitometer

Figure 2.43 Screw jack system on top of the T-slot beam structure

2.5.6 Power measurements on the test section

Figure 2.44 shows the schematic of the power connection of three DC power supplies on the test section. The current and voltage can be read from the DC power supplies. However, the voltage

reading from the DC power supplies includes the voltage drop on the test section, bus bars and electrical cables. To get more accurate voltage measurement on the test section, some copper cables are connected to the test section to measure the voltage by NI modules. Based on the voltage and current, the power on the test section can be calculated.

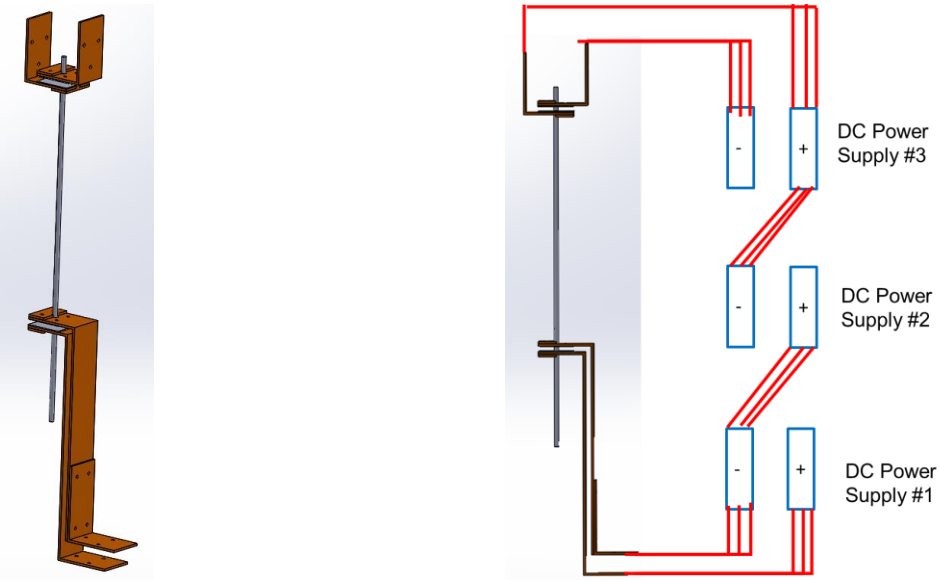


(a) Bus bar (b) Schematic of power connection

Figure 2.44 Electrical power connection on the test section

## 2.6 Data Acquisition and Control System

Figure 2.45 shows the schematic of the electrical power connection for the PCHT test facility, including 14 heaters, one pump and VFD, three DC power supplies, four motorized ball valves, three motorized needle valves, 19 temperature controllers, breakers, fuse, SCR (Silicon controlled rectifier), SSR (Solid state relay), and so on. Figure 2.46 shows three photos of part of the equipment for the power connection and Figure 2.47 shows the electrical and data acquisition

(DAQ) terminal box to accommodate control modules and data acquisition modules. The control panel as shown in Figure 2.47(a) is located in the control room to manually control the temperature and valves remotely, which also includes a shunt trip button to shut off all the power in the test facility in case of any emergency. In addition, there is a screw jack system for the traversing system in Figure 2.43 and signal processing unit for the gamma densitometer in Figure 2.35.

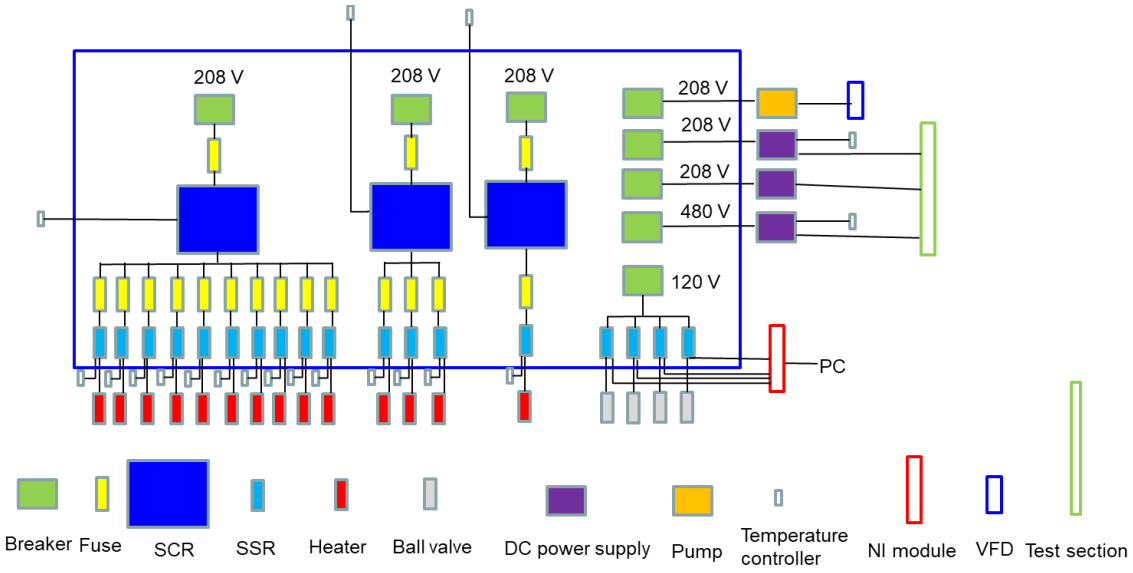


Figure 2.45 Schematic of the electrical power connection for the PCHT test facility

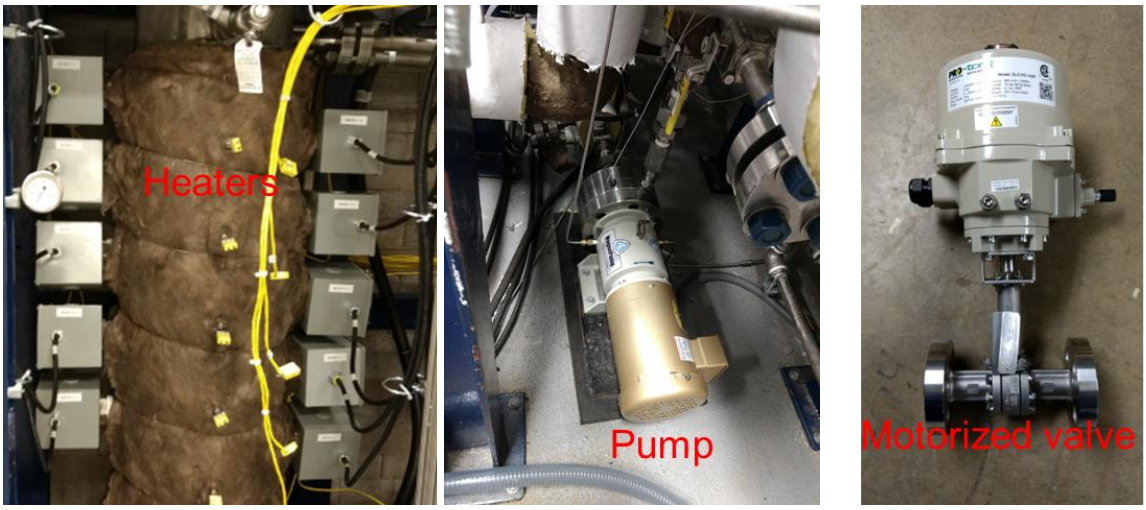


Figure 2.46 Photos of part of the equipment for power connection

(a) Control panel: Temperture controllers et al.

(b) Fuse, SCR, SSR et al.

(c) Breakers

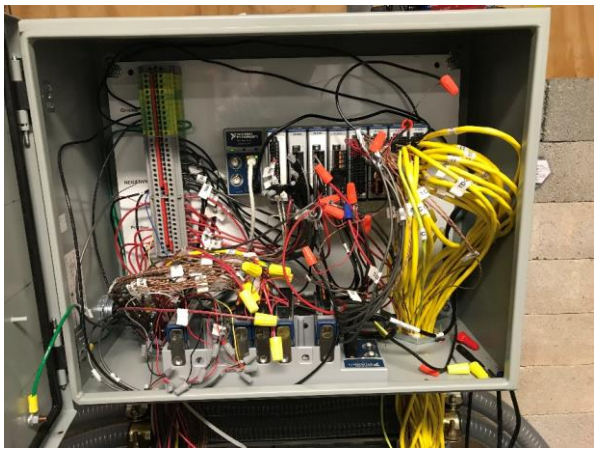

(d) DAQ terminal box

Figure 2.47 Electrical and DAQ terminal box

Besides the above hardware, there are a few software tools for the operation and control of the PCHT test facility, including a LabVIEW program in as shown in Figure 2.48, remote interface software for DC power supplies in Figure 2.49, Python scripts for motor control in the traversing system, and control system for the X-ray radiography system. In addition, an automatic shutdown system is designed and installed for DC Power Supply #2 as shown in Figure 2.50, which is based on the interlock function in the DC power supply and LabVIEW program. When the measured maximum temperature of the test section reaches a preset temperature, DC Power Supply #2 will be automatically shut off. Two tests are performed to test this automatic shutdown system. The results for two tests are shown in Figure 2.51 with the preset temperature at 25 and 30°C. It can be seen that when the measured maximum temperature of the test section reaches the preset temperature, the current of DC Power Supply #2 reduces from 200 A to 0 immediately, within one second (The thermocouple sampling rate is 1 Hz). After the shutdown of DC Power Supply #2, the maximum temperature continues to increase by about 1 °C due to the delay of the thermocouple response. In the actual post-CHF tests, the preset temperature will be set lower than the maximum allowable temperature of the test section by a certain margin to prevent the test section from overheating, therefore, to limit the test section failure due to overheating.

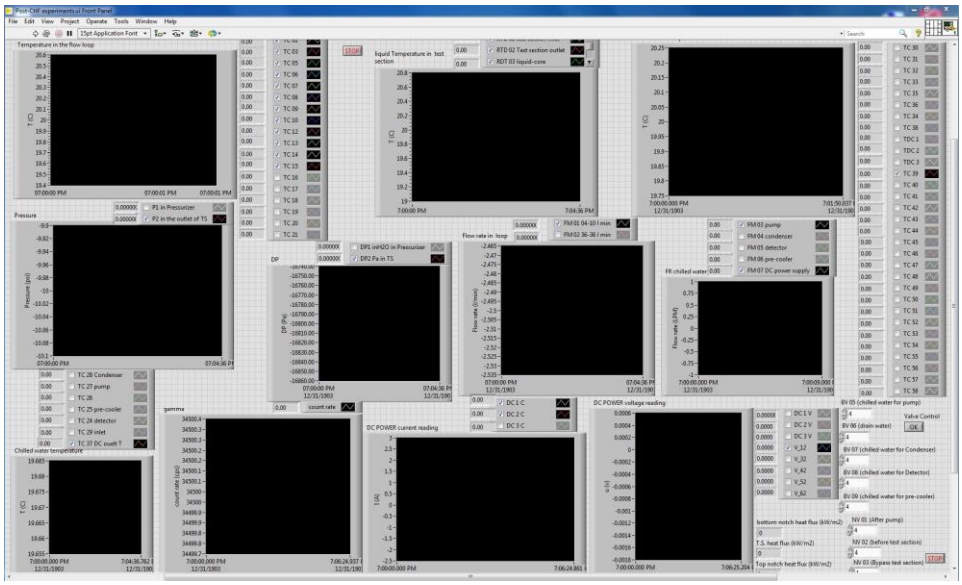

Figure 2.48 LabVIEW program for the PCHT test facility

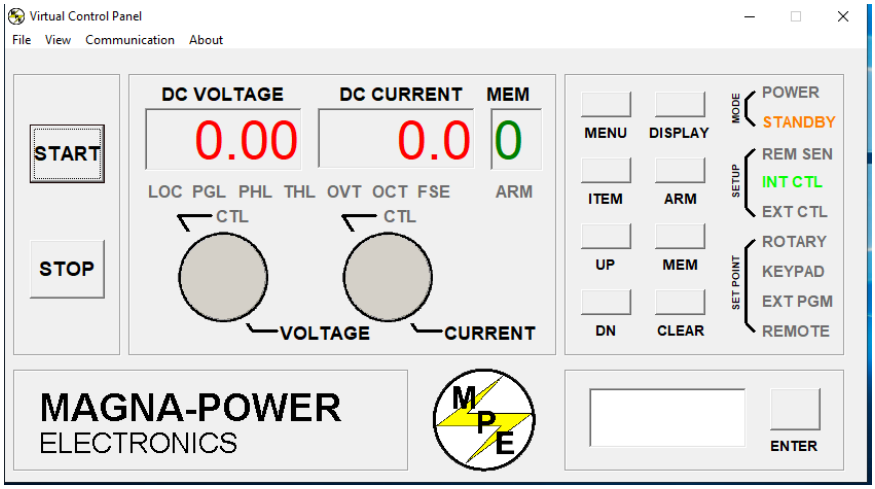


Figure 2.49 Remote interface software for DC power supplies

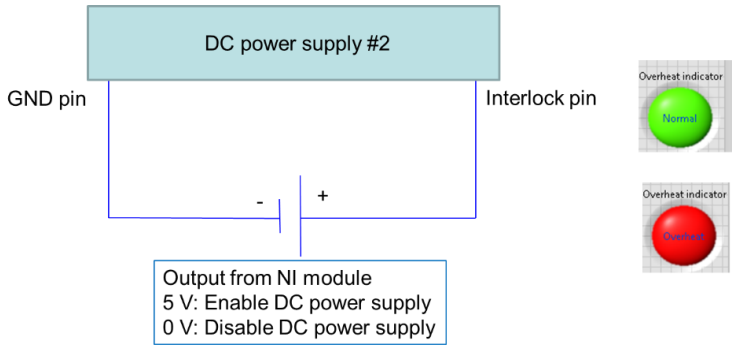


Figure 2.50 Schematic of the automatic shutdown system for DC Power Supply #2

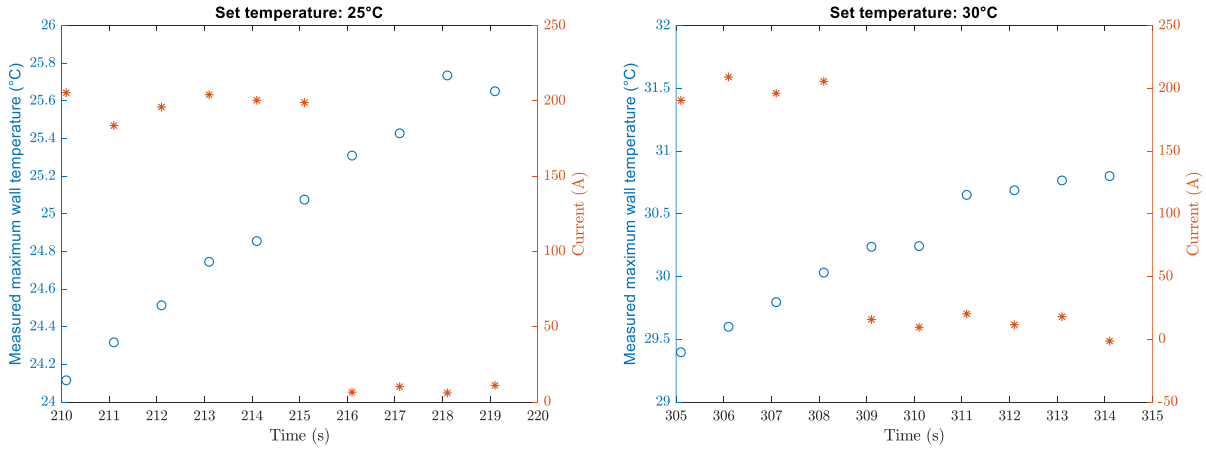


(a) Preset temperature at 25 °C (b) Preset temperature at 30 °C

Figure 2.51 Test results for the automatic shutdown system

## 2.7 Operation Procedure of the PCHT Test Facility

An operation procedure is designed for the IAFB tests. Table 2.14 summarizes the types of the valves in the flow loop in Figure 2.1. The operation procedure of the IAFB tests is described sequentially as follows.

Table 2.14 Types of major valves in the PCHT flow loop

| **Valve #** | **Valve type** |
|---|---|
| 1, 3, 4, 9, 10, 11, 12, 13, 15, 16, and 21 | Ball valve without an electric actuator |
| 2, 5, and 6 | Needle valve with an electric actuator |
| 7 | Check valve |
| 8, 14, 17, and 18 | Ball valve with an electric actuator |
| 19 and 20 | Safety valve |

(1) Degassing

Dissolved air in the water affects water boiling phenomenon in the test section, therefore, it must be removed out of the flow loop before performing any film boiling experiments. The following describes a procedure of removing air from the PCHT test facility.

1) First, Valves #11, 18 and 21 are closed, and all other valves are in open position. The entire flow loop, including the test section, is vacuumed by a vacuum pump.

2) When a certain level of vacuum, i.e., 1 micrometer of mercury head, is reached, Valves #1, 9, 10, 13, and 17 are closed and Valve #21 is opened. The distilled water will be charged into the reservoir tank and pressurizer through Valve #21 since the line with Valve #21 is connected to the DI water source.

3) After the reservoir tank and pressurizer are filled with water, Valve #21 will be closed and Valve #18 opened. The water will then be heated to boil for degassing in the reservoir tank and pressurizer, and the air/steam mixture will be released through Valve #18 to the atmosphere.

4) After the degassing, Valves #5, 8, and 14 will be closed, while Valves #1, 10, and 17 will be opened. Degassed water will flow into the corresponding pipe sections from the reservoir tank and pressurizer.

5) If needed, additional distilled water may be added to the pressurizer as to make up its loss of liquid inventory, while Valve # 12 should be closed to prevent the newly added water from getting into the reservoir tank and flow loop. The degassing process in the pressurizer will then be repeated.

6) After degassing in the pressurizer, Valve #18 will be closed, and Valves #12 and 13 will be reopened. If the water in the loop does not need to be filtered, Valves #15 and 16 are closed.

(2) Pressurizing the system

The system pressure is adjusted and maintained by the pressurizer. In the pressurizer, pressure is controlled by varying the water and steam temperatures. Three electric heaters with a total heating power of 13.5 kW are used to heat and vaporize, if needed, the water in the pressurizer, controlled by proportional–integral–derivative (PID) controllers. If the system pressure is higher than the desired value, Valve #18 can be opened to release the pressure. A safety valve is installed on the pressurizer for automatic pressure relief if needed. In addition, a differential pressure transducer is installed between the top and bottom of the pressurizer to monitor the water level in the pressurizer, which can be calculated based on the differential pressure measurement.

(3) Establishing the flow conditions at the test section inlet

Initially, Valves #5 and 8 are closed and water is heated and circulated through Bypass line #1 instead of the test section till the desired flow condition, such as the system pressure, flow rate, and inlet subcooling, reaches the desired values. The water flow rate is adjusted to the desired value by adjusting the variable frequency drive of the circulation pump and regulating valve, i.e., Valve #2. If needed, Valve #17 can be opened and a pump bypass to the test section will be used to help further adjust the flow rate flowing through the test section.

(4) Heating the test section

The bottom hot patch power, test section power and top hot patch power are turned on to heat up the test section to the desired temperatures. In Chen and Li's experiments (Chen and Li, 1984), the test section wall temperature was heated to the range of 500-700 ºC before liquid water was diverted into the test section, which provides a temperature reference for our future tests.

(5) Drawing the steam

To help form the film boiling phenomenon in the test section, Valve # 14 can be opened so that the steam from the pressurizer will be drawn into the test section to form a steam environment before the liquid water enters the test section.

(6) Diverting the water flow from Bypass line #1 to the test section

After the water flow conditions and test section power reach the desired values, Valve #8 is gradually opened. Valve #5 is opened gradually and then Valve #6 is closed gradually to prevent wetting of the test section (film boiling section). Because the test section wall is cooled by the water flow, the test section power needs to be adjusted to keep the wall temperature higher than the minimum film boiling temperature to stabilize film boiling inside the test section. In addition, because there is a flow resistance difference between Bypass line #1 and the test section, the water flow rate may need to be slightly adjusted by adjusting the regulating valve, Valve #2.

(7) Performing IAFB tests

The test section power can be adjusted gradually to expose the void measurement station to the full range of conditions for the IAFB region. The test section power is then kept steady. Sufficient time is allowed for test conditions to stabilize. The X-ray radiography system and gamma densitometer are traversed up and down to measure the void fraction at different elevations.

(8) Completing one test and continuing next test

After finishing the first IAFB test, the test section power will be reduced in steps while maintaining the system pressure. At each power level, the flow conditions will be allowed to stabilize, a data scan is taken, and the obtained data are stored until the test section rewets. This test procedure is expected to allow measurements of both the minimum film boiling temperature and heat flux values. After completing the tests at one system pressure level, repeat the procedures from Steps (2) to (8) and start the next test at a different system pressure.

## 2.8 Test Summary

In this research, a number of performance tests and post-CHF heat transfer experiments have been performed in the PCHT test facility, including hydrostatic leak test (HLT), pressure control test (PCT), subcooled boiling test (SBT), hot patch test (HPT), gamma densitometer test (GDT), X-ray radiography test (XRT), reflooding test (RFT), and dry patch test (DPT). The flow conditions of selected tests are summarized in Table 2.15 and will be discussed in Chapters 3 and 4.

Table 2.15 Flow conditions of selected tests

| **Test** | **System pressure (psia (MPa))** | **Mass flux (kg/m$^2$-s)** | **Inlet subcooling (ºC)** |
|---|---|---|---|
| HLT | 95 to 1,015 (0.66 to 7.00) | - | - |
| PCT | 42 (0.30) | - | - |
| SBT | 16 to 20 (0.11 to 0.14) | 300 to 1,000 | 20 to 80 |
| HPT | 13.6 (0.09) | 60 | 50 |
| GDT | 18 (0.12) | 350, 380, 420 | 20, 30, 35 |
| XRT | 17 (0.12) | 0, 420 | 20 |
| RFT | 17 (0.12) | 0 to 400 | 20 |
| DPT | 22 (0.15) | 150 | 30 |

# Chapter 3 Test Facility Performance Tests

## 3.1 Pressure Tests

To ensure the reliability and leak tightness of the test facility, and therefore the personnel safety, hydrostatic leak tests have been performed for the PCHT test facility. It should be noted that all the components of the test facility are supposed to be able to withstand pressures up to 1,000 psi at 280 ℃ (a requirement to all the component vendors). The three vessels, i.e., the reservoir tank, pressurizer, and pre-heater, and all the piping in the flow loop have successfully passed the hydrostatic tests at a pressure of 1,500 psig at the room temperature, as evidenced by the vendors. The hydrostatic leak tests for the PCHT test facility have been performed at the room temperature (instead of the actual higher temperatures when the facility is under operation) per ASME B31.3 code (ASME 2007). According to the code, the minimum "equivalent" hydrostatic test gage pressure for the post-CHF tests at 500 psig is 813 psig:

$$P_T = 1.5P\,S_T \big/ S \tag{3-1}$$

where $P$ is the internal design gage pressure (500 psig); $P_T$ the minimum hydrostatic test gage pressure at the room temperature (psig); $S$ the allowable stress of the material of construction of the facility, i.e., SS 316, at the design temperature 242°C, 15.4 ksi per the ASME code; $S_T$ the

allowable stress of SS 316 at the hydrostatic test temperature, i.e., the room temperature 20 °C: 16.7 ksi.

Figure 3.1 shows the schematic diagram for the hydrostatic leak test. Table 3.1 shows the test pressures and the corresponding test times held at those pressures (without leakage observed or pressure reduced). Typically, duration of 10 to 35 minutes was held at each of the test pressures while the ASME code requires a minimum of 10 minutes of holding time.

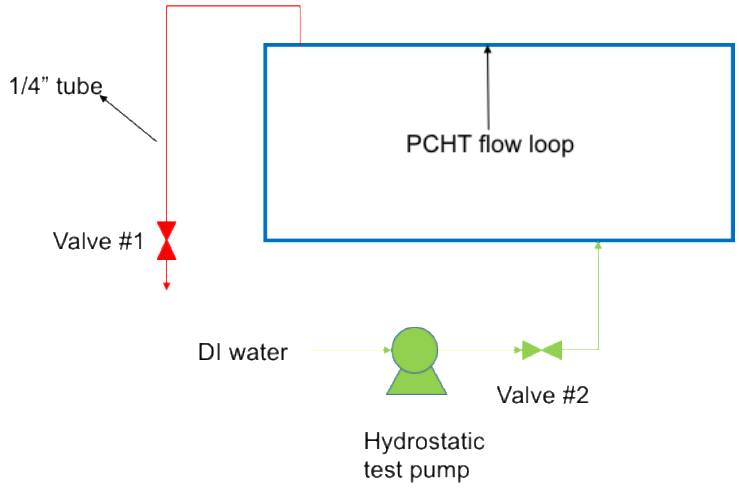


Figure 3.1 Schematic diagram for the hydrostatic leak test

Table 3.1 Hydrostatic leak test pressures and holding times

| | | | | | | | | | | | | |
|---|---|---|---|---|---|---|---|---|---|---|---|---|
| Pressure (psig) | 80 | 160 | 270 | 400 | 500 | 580 | 640 | 720 | 830 | 860 | 940 | 1,000 |
| Pressure (MPa) | 0.55 | 1.10 | 1.86 | 2.76 | 3.45 | 4.00 | 4.41 | 4.96 | 5.72 | 5.93 | 6.48 | 6.89 |
| Holding time (min) | 10 | 10 | 11 | 10 | 10 | 10 | 14 | 16 | 13 | 29 | 18 | 35 |

A preliminary test was performed to increase the system pressure to a low level, i.e., 42 psia, by heating the water to produce steam using three electric heaters in the pressurizer. Figure 3.2 shows the system pressure measured at the outlet of the test section. From 2,550 to 3,750 s, the system pressure reached a steady-state condition. The average pressure during that period of time was 42.03 psia, and the standard deviation of the measured pressure was 0.20 psi, which indicates that the system pressure can be controlled at a steady-state state by the pressurizer. The motorized valve connecting the pressurizer to a discharge line was opened remotely at about 3,750 s and the system pressure dropped rapidly.

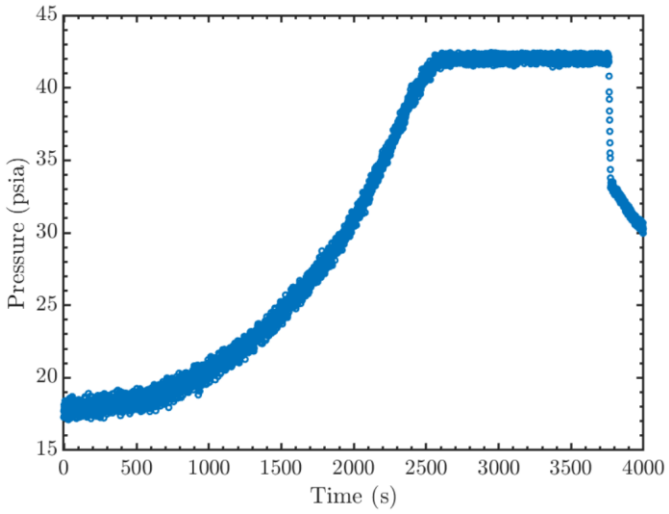


Figure 3.2 System pressure measured at the outlet of the test section

## 3.2 Subcooled Boiling Tests

Prior to the film boiling tests, subcooled flow boiling tests were performed to test the operation of the flow loop and evaluate the hot patch design. In this section, one of the subcooled flow boiling tests is described. In this test, the power of the DC Power Supply #2 was current controlled, and

the current was increased up to 1,750 A in steps in these tests. It should be noted that the water is heated in the test section by the DC power supplies and no cooling water in the condenser is used to cool the water. The outer surface temperature of the test section wall, including the two notches, were measured using six 1/16" K-type sheathed but ungrounded thermocouples. The locations of the thermocouples are shown in Figure 2.12(c). The experimental data, including the system pressure, flow rate, heating power to the test section, wall temperature, water temperature, and pressure drop across the test section are described in the following section.

The water pressure was measured by a Honeywell absolute pressure transducer (Model No.: STA77L-E1H000-1-A-AHC-11S-A-00A0-F1-0000). The measurement accuracy of the pressure transducer is 0.065% of the span. In the tests, the pressure was measured at the outlet of the test section and the results are shown in Figure 3.3. The water pressure was initially measured to be 17.0 psia and increased to 18.0 psia as the water was heated in the test section. The standard deviation of the measured pressure data is 0.19 psi.

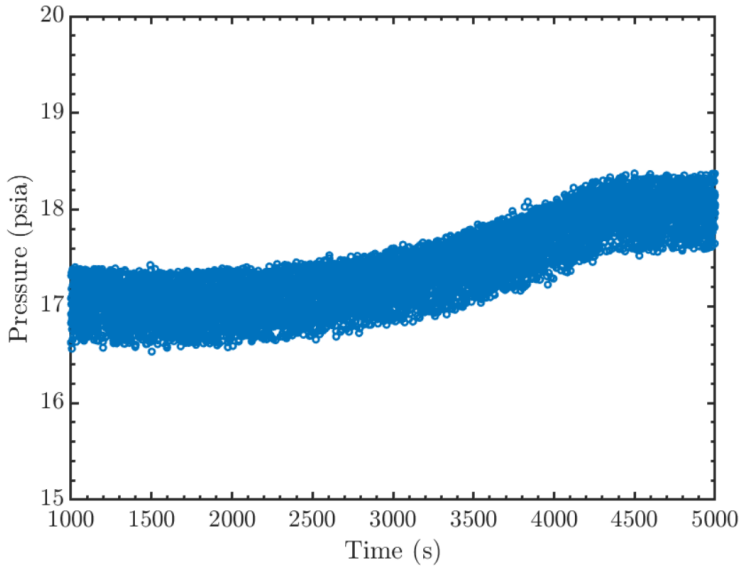


Figure 3.3 Water pressure measured at the outlet of the test section

The water flow rate was measured by a turbine flowmeter from ICENTA (Model No: IC-LTM-06A-S-S-H-B-H-0-D-R-Z). The measurement range of the flowmeter is 0.4 to 10 LPM. From the calibration data of the flowmeter, its measurement accuracy is 0.25%. The measured volumetric flow rate is shown in Figure 3.4. The volumetric flow rate increases slightly as the water is heated. The average volumetric flow rate is about 8.1 LPM, corresponding to a mass flux of 1,021 kg/m$^2$-s in the test section.

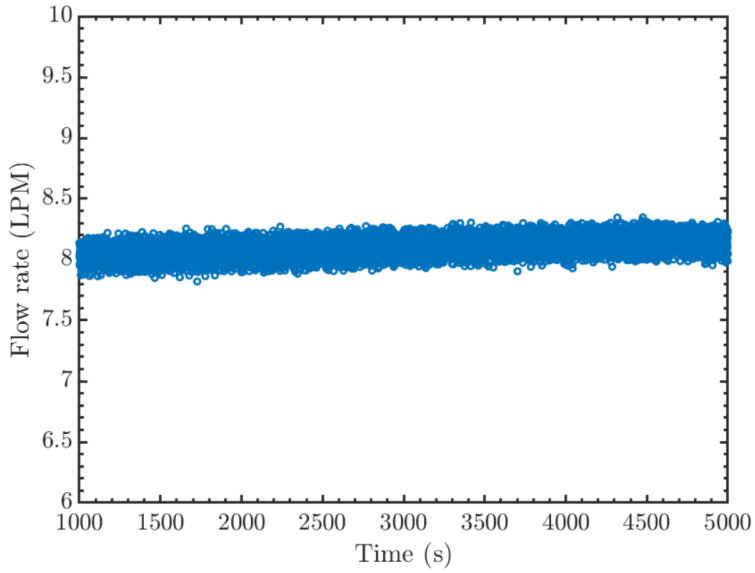


Figure 3.4 Measured water volumetric flow rate

The pressure drop across the test section was measured by a Honeywell differential pressure transducer (Model No.: STD720-E1HC2AS-1-A-AHC-11S-A-10A0-00-0000). The measurement range can be adjusted in the range of -400 to 400 in$H_2O$. The measurement accuracy is 0.05% of the span. The pressure drop across the test section decreased slightly as the water was heated as shown in Figure 3.5. Between 3,300 and 4,400 s, there were some fluctuations of the pressure

drop, which could be due to subcooled boiling. From Figure 3.6 and Figure 3.9, it can be seen that the test section wall outer surface temperature is higher than 100 ℃ while the water temperature is less than 33 ℃. Boiling could have occurred on the inner surface of the tube, and condensed as the bubbles departed due to the significant subcooling of the bulk water, which caused the fluctuations in the pressure drop measurement.

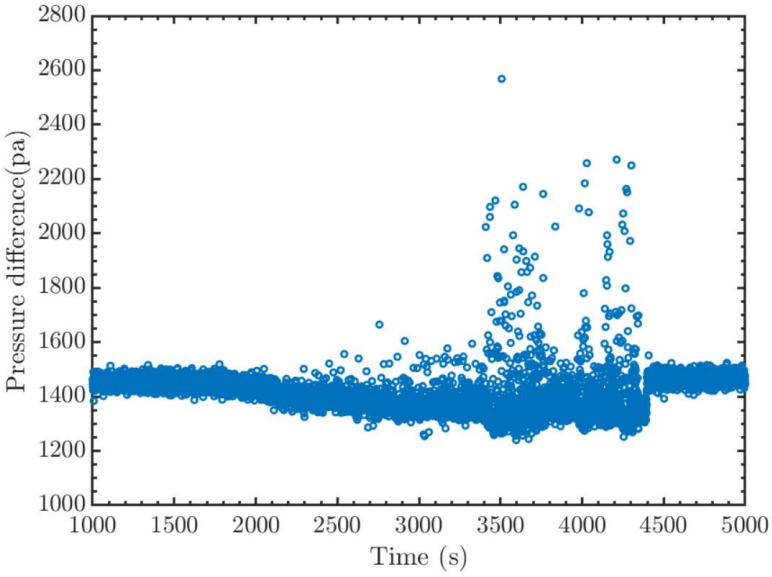


Figure 3.5 Measured pressure drop across the test section

Figure 3.6 shows the outer surface temperature of the test section wall. It can be seen that the temperatures at the notches (TCs # 1 and 8) are higher than those at the tube surface due to the higher heat flux at the notches. When the current is 1,750 A, the temperature difference between the notches and tube surface is up to 80 °C.

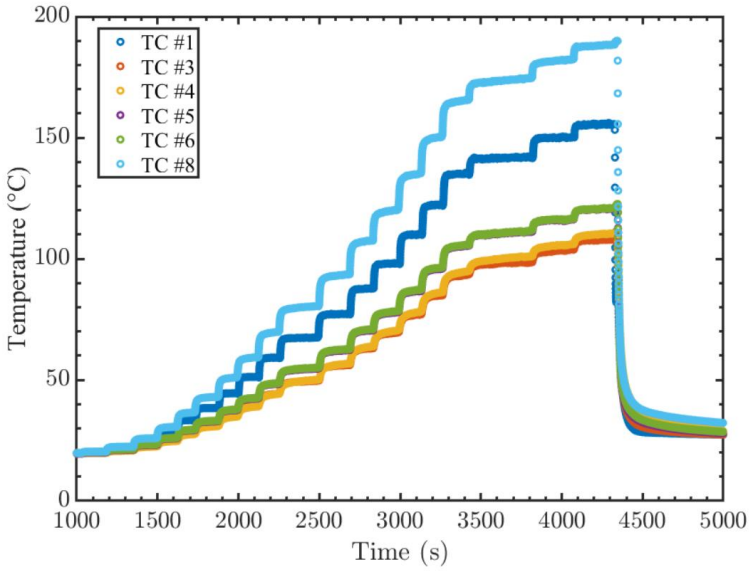


Figure 3.6 Measured outer surface temperature of the test section

The outer surface temperature of the thermal insulation on the test section was measured and shown in Figure 3.7, which increased by about 10 °C as the current increased from 100 to 1,750 A. The thermal insulation is microporous insulation with a one-inch thickness. In addition, the room temperature was also measured for reference and is shown in Figure 3.8. This information will be used to evaluate the heat losses to the ambient.

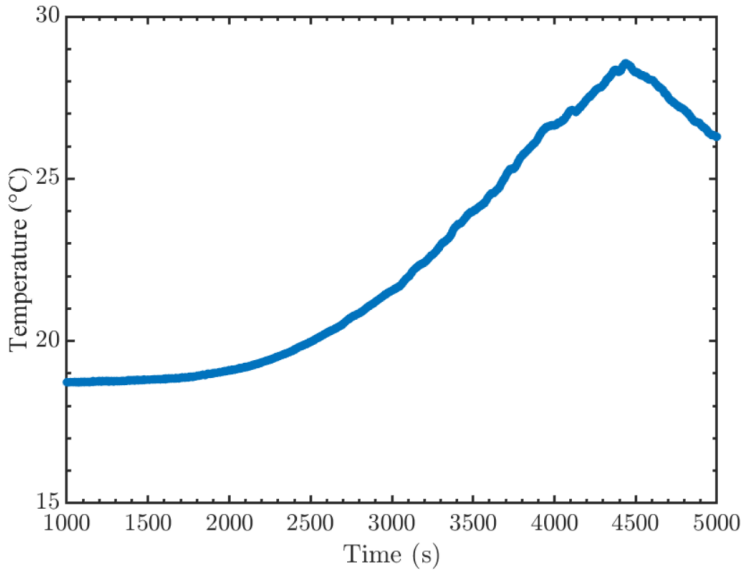


Figure 3.7 Measured outer surface temperature of the insulation on the test section

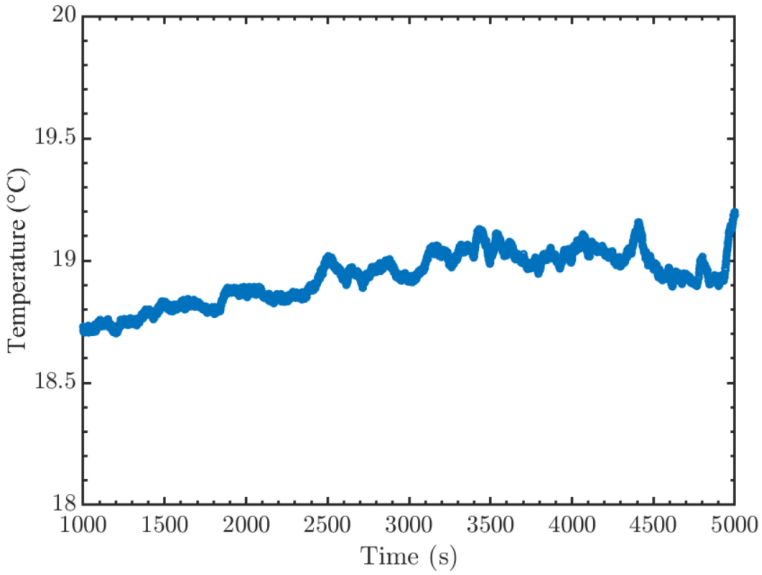


Figure 3.8 Measured room temperature near the PCHT test facility

The water temperature was measured at the inlet, outlet, and center of the test section using RTDs #01, 02, and 03, respectively. The location of the RTD #03 is shown in Figure 2.12(c). Water was circulated in the PCHT test facility and was heated in the test section but not cooled. Therefore,

the water inlet temperature increased with time. When the DC power supplies were turned off at about 4,400 s, the inlet temperature, outlet temperature, and liquid-core temperature became approximately the same. The liquid-core temperature represents the centerline temperature of the water in the test section measured by RTD #3 as shown in Figure 3.9.

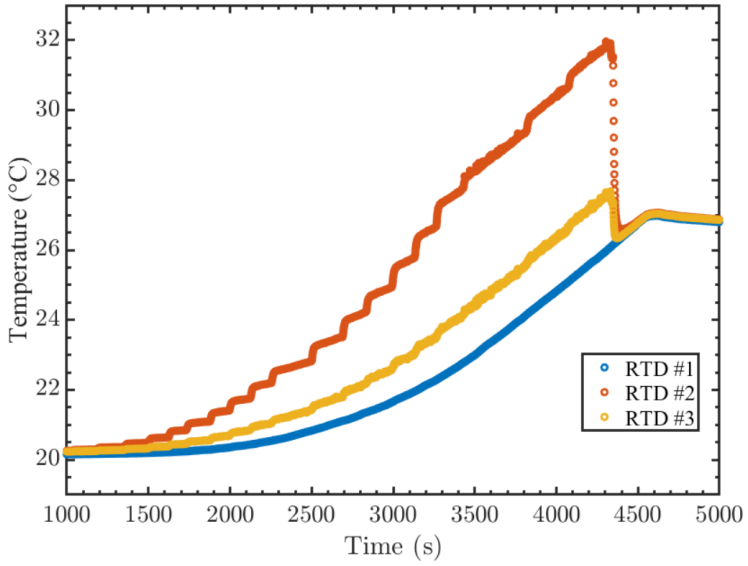


Figure 3.9 Measured water temperatures in the test section

## 3.3 Hot Patch Tests

The objective of the hot patch tests is to heat the bottom notch to a high temperature to initiate film boiling at the bottom notch. In the hot patch tests, the bottom notch temperature is controlled at 230, 310 and 435 °C, respectively. The water flowed through the test section with a flow rate of 0.5 LPM. The system pressure was only 13.6 psia. The inlet subcooling is about 50 ºC. The results are shown in Figure 3.10 to Figure 3.12. It can be seen that the DC current fluctuated significantly

at first, and then the magnitudes of the fluctuations decrease gradually. The notch temperature is relatively constant.

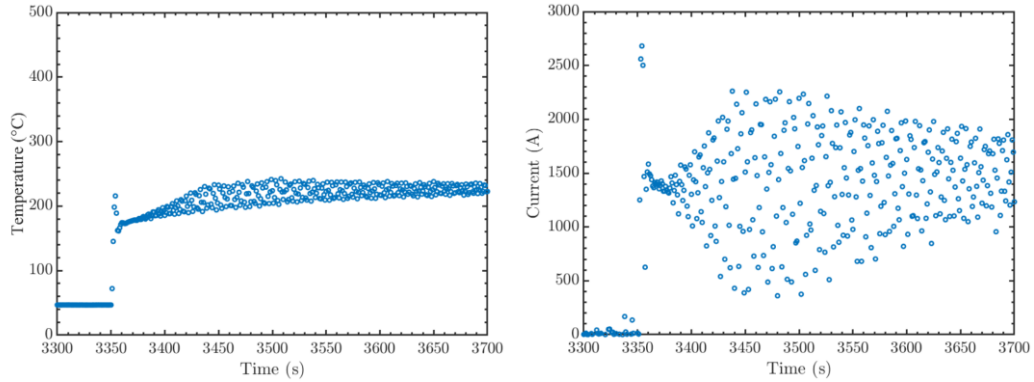


(a) Bottom notch temperture (b) DC current

Figure 3.10 Hot patch tests with $T_{notch}$= 230 °C

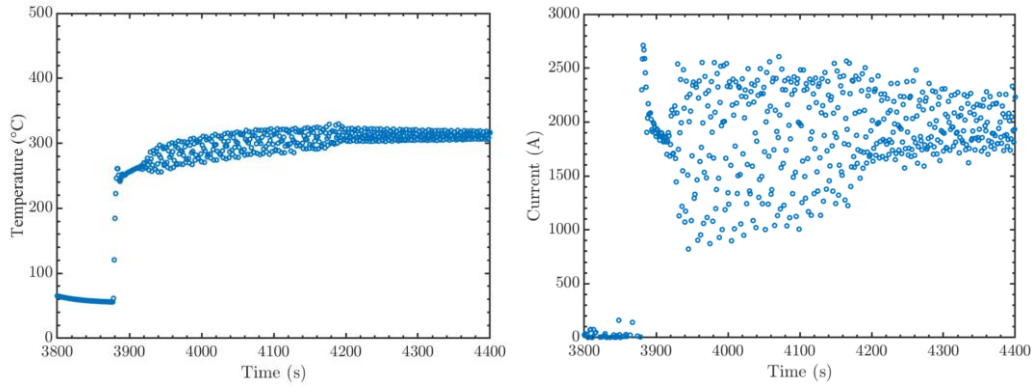


(a) Bottom notch temperture (b) DC current

Figure 3.11 Hot patch tests with $T_{notch}$ = 310 °C

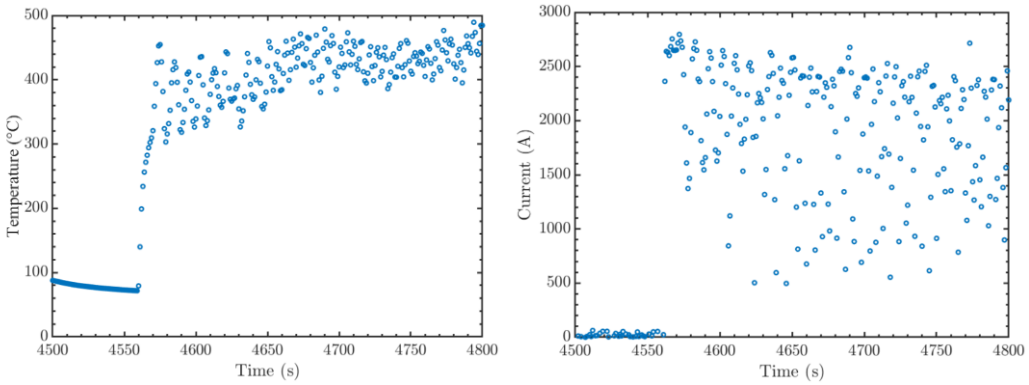


(a) Bottom notch temperture (b) DC current

Figure 3.12 Hot patch tests with $T_{notch}$ = 435 °C

Figure 3.13 and Figure 3.14 show the pressure drop and water flow rate through the test section. It can be seen that the pressure drop and flow rate fluctuate significantly when the bottom notch temperature was set at 435 °C, which is believed due to the flow regime transition from nucleate boiling to film boiling. From these results, we can conclude that the hot patch can induce the flow regime transition from nucleate boiling to film boiling.

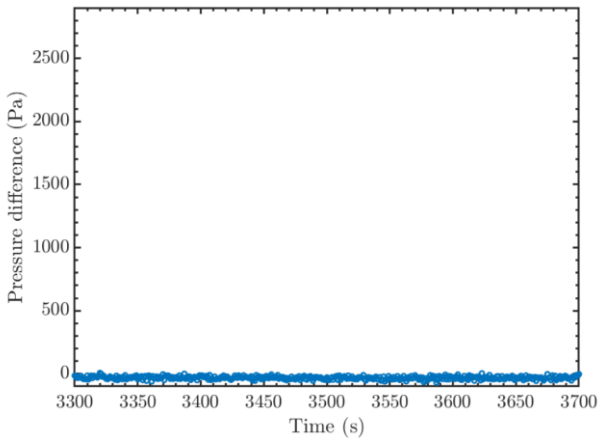


(a) $T_{notch}$ = 230 °C

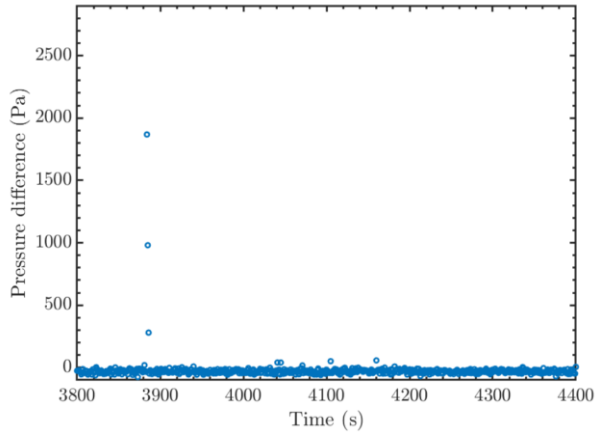


(b) $T_{notch}$ = 310 °C

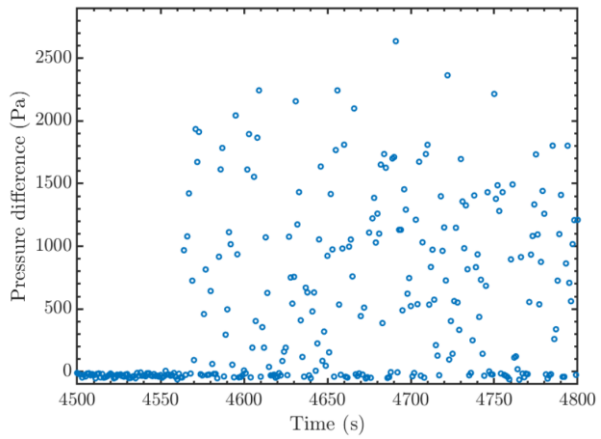


(c) $T_{notch}$ = 435 °C

Figure 3.13 Measured pressure drop across the test section

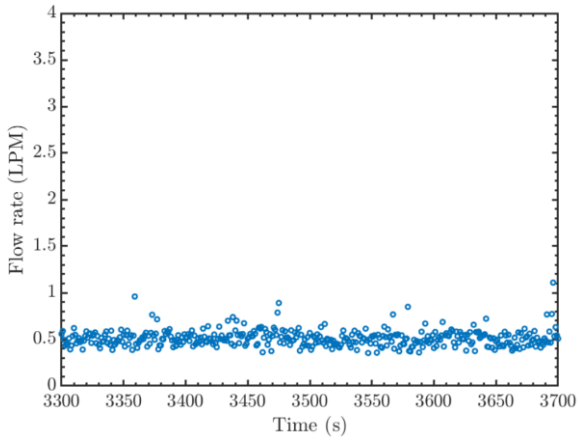


(a) $T_{notch}$= 230 °C

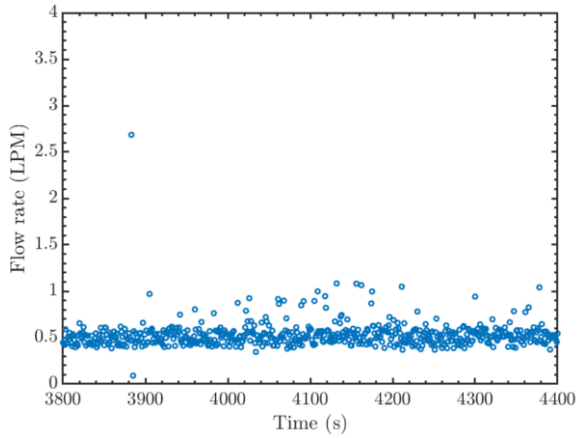


(b) $T_{notch}$= 310 °C

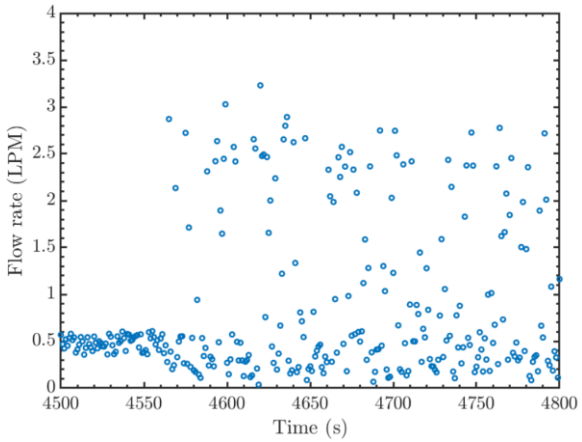


(c) $T_{notch}$= 435 °C

Figure 3.14 Measured water flow rate through the test section

## 3.4 Gamma Densitometer Tests

A number of gamma densitometer tests have been performed in the PCHT test facility. Before measuring the void fraction in two-phase flows, two calibration tests need to be performed, i.e., with the test section full of water and full of air or steam. Four cases are performed for the calibration points as follows. The time constant of the gamma densitometer in these four cases is set as 60 s. Table 3.2 shows the measurement results of the gamma densitometer.

Case#1: without thermal insulation, water and air, without collimator

Case #2: without thermal insulation, water and air, with collimator

Case #3: with thermal insulation, water and air, without collimator

Case #4: with thermal insulation, water and steam, without collimator.

Table 3.2 Measurement results of the gamma densitometer

| Case # | T.S. full of air (cps) | T.S. full of water (cps) | $R_{air}$-$R_{water}$ (cps) | $\sigma_R$ (cps) | $\sigma_\alpha$ (%) |
|---|---|---|---|---|---|
| 1 | 77,576 | 75,169 | 2,407 | 25 | 1.06 |
| 2 | 37,591 | 34,993 | 2,598 | 17 | 0.68 |
| 3 | 68,079 | 65,686 | 2,393 | 24 | 1.00 |
| 4 | 78,821 (steam) | 78,500 | 321 | 26 | 7.98 |

From the measured results, it can be seen that the standard deviation of the void fraction in Case #4 is much larger than those in the other three cases. The reason is that when Case #4 was performed, the test section was filled with a mixture of the water and steam instead of pure steam, which made a significant effect on the measurement of the count rate. Comparing. Cases#1 with 2, it can be seen that the collimator has slightly helped reduce the standard deviation of the void fraction measurements. In summary, air is more practical than steam for calibration tests, and the collimator can be used for the gamma densitometer. Figure 3.15 shows the void fraction

measurement using the gamma densitometer in the subcooled boiling. The system pressure is 18 psia, mass flux is 350 kg/m$^2$-s and the inlet subcooling is 35 ºC. It can be seen that the void fraction is almost constant along the test section for the heat flux of 175 kW/m$^2$ and increases for the heat flux of 220 kW/m$^2$.

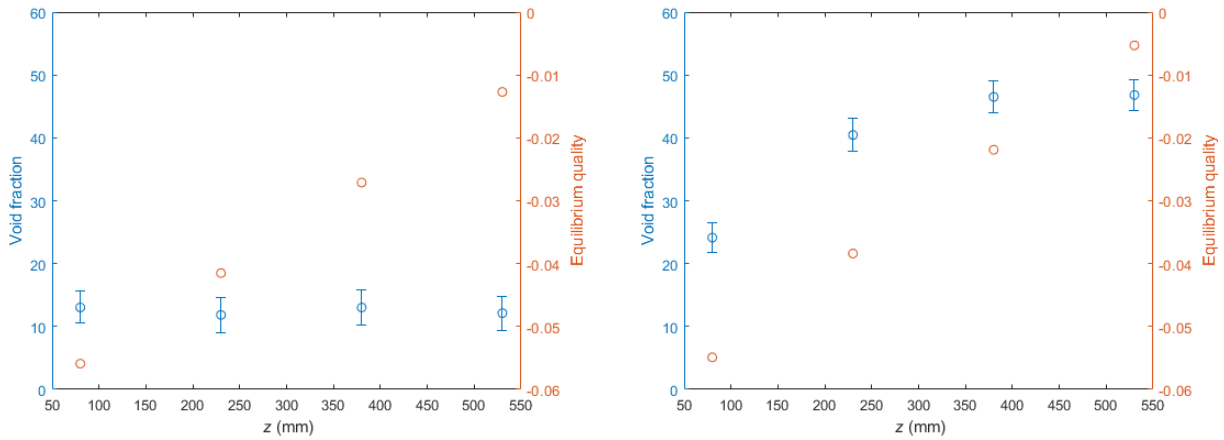


(a) Heat flux: 175 kW/m$^2$ (b) Heat flux: 220 kW/m$^2$

Figure 3.15 Void fraction measurement using gamma densitometer

## 3.5 X-ray Radiography System Tests

### 3.5.1 Parameters selection

The performance of the X-ray radiography system is affected by a few parameters, such as voltage, current, focal spot size, etc. In this section, these parameters are studied to optimize the performance of the X-ray radiography system. Figure 3.16 shows an image from the X-ray radiography system with the test section full of water, from which the test section wall location can be established. To quantitatively define the test section wall in the image, an analysis of the count rate profile is performed as shown in Figure 3.17 and Figure 3.18. It can be seen that there

are two valleys in the count rate profiles in Figure 3.18, which are corresponding to the positions of B and C in Figure 3.17. B and C represent the inner surface of the test section. Based on these two valleys, the inner surface of test section wall can be quantitatively defined in the X-ray image. In addition, the scaling from pixel sizes on the image to the actual sizes of materials in the test section can be determined based on the inner diameter of the test section and pixel sizes between these two valleys.

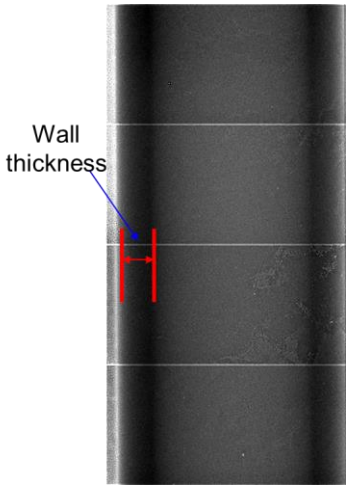


Figure 3.16 An image of the test section with full of water from X-ray radiography system

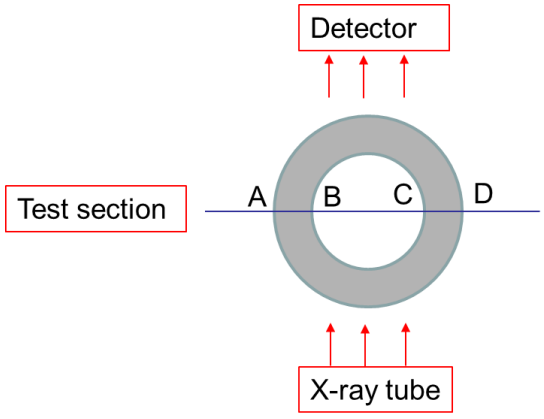


Figure 3.17 Schematic of the X-ray radiography system and test section tube

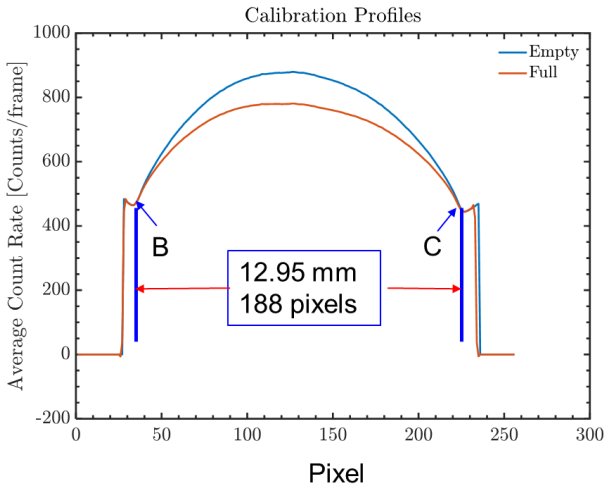


Figure 3.18 Profile of the count rates in the X-ray image for test section full of water and air

The performance of the X-ray radiography system is related to the focal spot size, voltage, and current of the X-ray tube. Considering that the test section tube is thick, i.e., 0.12”-thick, the voltage of the X-ray tube is set at the maximum value, i.e., 150 kV. There are two focal spot sizes, i.e., 0.6 and 1.2 mm. The current is set at 500 A for large focal spot and 200 A for small focal spot, which are the maximum values for the specific focal spot size. To prevent the saturation of the count rates on the detector, a copper shielding may be used in front of the X-ray tube to reduce the photon flux as shown in the blue circle in Figure 3.19(a). Three cases in Table 3.3 are performed to study the performance of the X-ray radiography system with the test section full of air and full of water.

(a) X-ray tube


(b) Detector

Figure 3.19 X-ray tube and detector

Table 3.3 Case study for parameter selection of the X-ray radiography system

| Case # | Focal spot size (mm) | With shielding | Voltage (kV) | Current (mA) | Exposure time (ms) |
|---|---|---|---|---|---|
| 1 | 1.2 (Large) | Yes | 150 | 500 | 0.5 |
| 2 | 0.6 (Small) | | | 200 | 1.0 |
| 3 | | No | | | |

Figure 3.20 shows the difference of the count rates for test section full of air and water for different frequencies of the detector. It can be seen that the difference increases as the frequency decreases. For the same frequency, Case # 1 has the largest difference and Case #2 has the smallest difference.

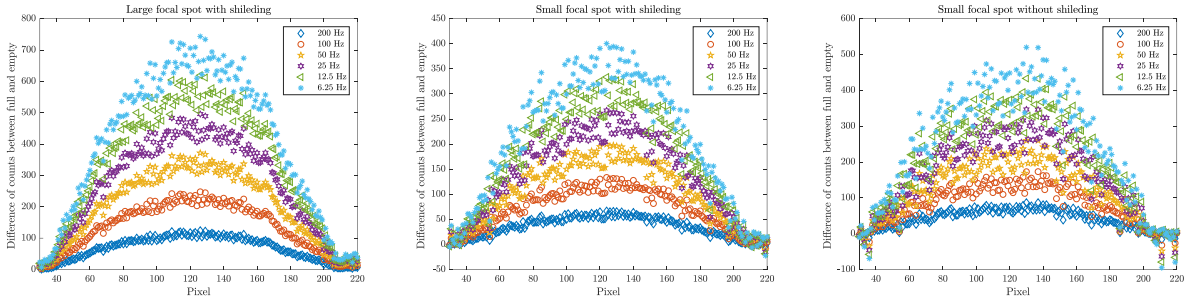


(a) Case #1 (b) Case #2 (c) Case #3

Figure 3.20 Difference of the count rate for test section full of air and water for different frequencies

Figure 3.21 show the standard deviation of the void fraction for different frequencies. It can be seen that the standard deviation increases from the central region to the inner surface of the test section for all the three cases. The standard deviation increases as the frequency increases. For the same frequency, Case # 1 has the smallest standard deviation and Case #2 has the largest standard deviation. However, the standard deviation of the void fraction in the central region for Case #1 is still very larger, up to 15% for 6.25 Hz and 40% for 200 Hz.

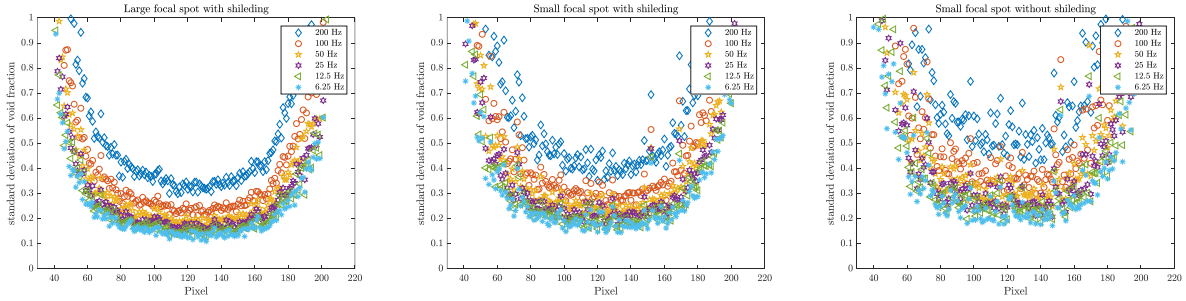


(a) Case #1 (b) Case #2 (c) Case #3

Figure 3.21 Standard deviation of the void fraction for different frequencies

The spatial resolution of the detector is 0.1 mm and the void fraction is calculated in a 0.1 mm × 0.1 mm area as shown in Figure 3.22(a). To reduce the standard deviation of the void fraction, the sampling size needs to be increased but to reduce the spatial resolution for the void fraction calculation. The standard deviation of the void fraction is calculated for areas of 0.1 mm × 0.5 mm, 0.1 mm × 1.0 mm, 0.1 mm × 1.5 mm, and 0.1 mm × 5.0 mm corresponding to spatial resolution of 0.5, 1.0, 1.5 and 5.0 mm as shown in Figure 3.23 to Figure 3.27. The standard deviation for spatial resolution of 0.1 mm is shown in Figure 3.21. It can be seen that the standard deviation of the void fraction decreases as the spatial resolution increases for the same frequency and same case. At the spatial resolution of 5.0 mm, the standard deviation of the void fraction in the central region for Case #1 is about 2% for 6.25 Hz and 5% for 200 Hz. Based on the study, the X-ray radiography system has the optimal performance with the parameters in Case #1.

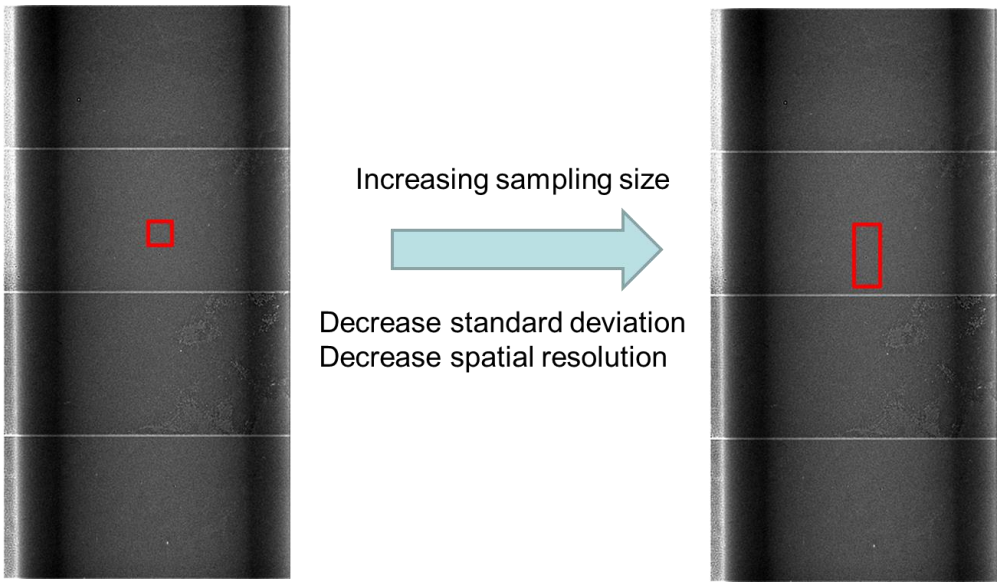


(a) (b)

Figure 3.22 Sampling size for the void fraction calculation

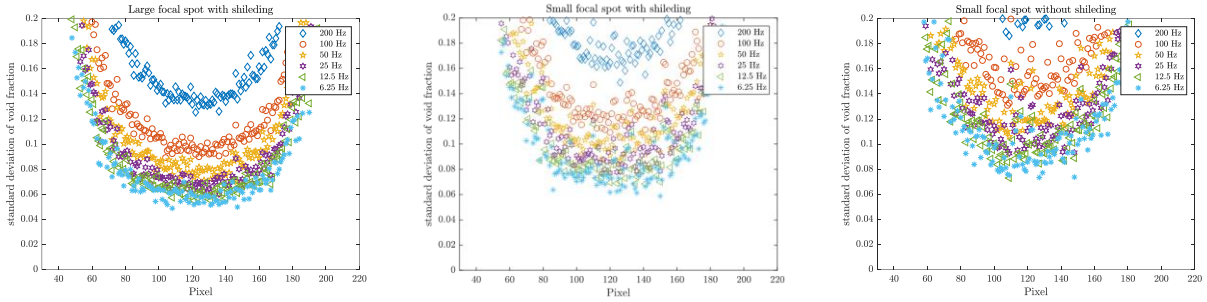


(a) Case #1 (b) Case #2 (c) Case #3

Figure 3.23 Standard deviation of the void fraction spatial resolution of 0.5 mm for different frequencies

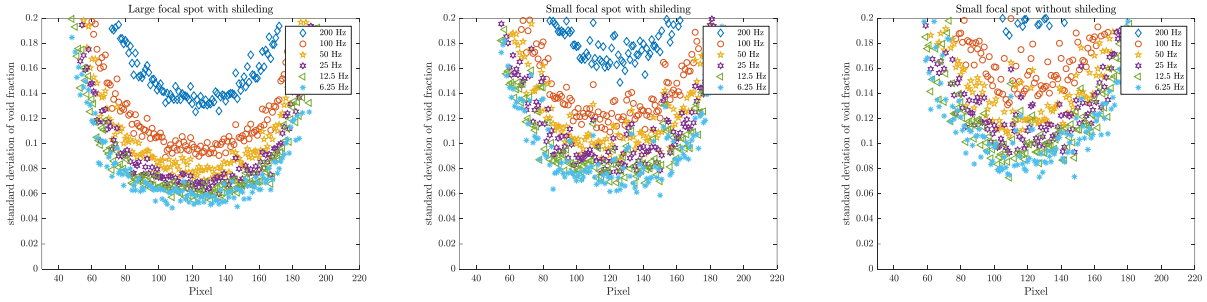


(a) Case #1 (b) Case #2 (c) Case #3

Figure 3.24 Standard deviation of the void fraction spatial resolution of 0.5 mm for different frequencies

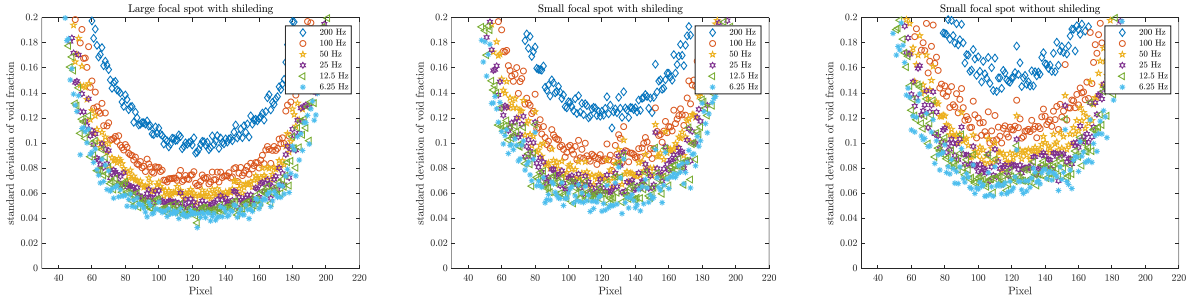


(a) Case #1 (b) Case #2 (c) Case #3

Figure 3.25 Standard deviation of the void fraction spatial resolution of 1.0 mm for different frequencies

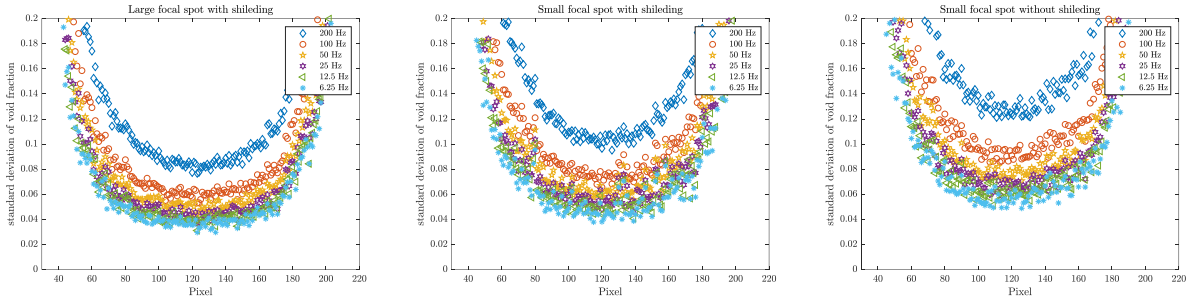


(a) Case #1 (b) Case #2 (c) Case #3

Figure 3.26 Standard deviation of the void fraction spatial resolution of 1.5 mm for different frequencies

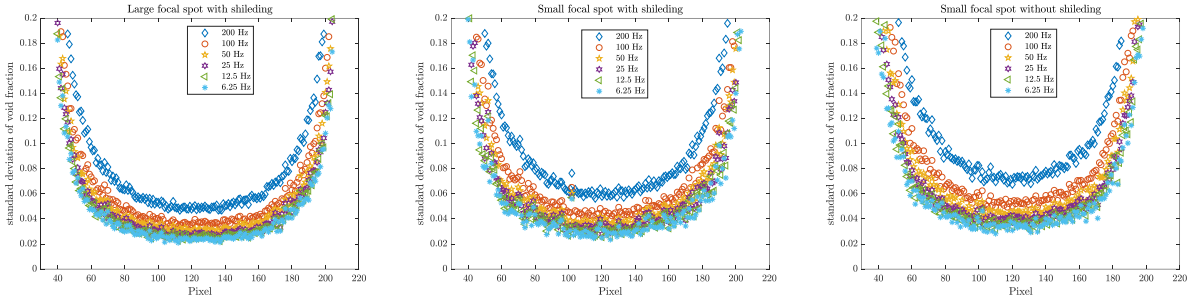


(a) Case #1 (b) Case #2 (c) Case #3

Figure 3.27 Standard deviation of the void fraction spatial resolution of 5.0 mm for different frequencies

### 3.5.2 Natural convection boiling tests

The X-ray radiography system was tested in the natural convection boiling. In the tests, the test section is filled with liquid water at about 20 ºC. The system pressure measured at the outlet of the test section is about 18 psia and the water is not flowing. As the water is heated by a DC power supply, boiling can occur, which is captured by the X-ray radiography system. The frame rate of the detector is 200 Hz. Two different flow regimes, i.e., bubbly flow and slug flow, are captured

by the X-ray radiography system as shown in Figure 3.28. Figure 3.29 shows the liquid core temperature near the end of the heated length (5.0 mm from the bottom edge of the top notch). At about 25 s, the liquid core temperature increases rapidly, which means that the bubble is produced in the flow. At this time, the X-ray radiography system was turned on to capture the images of the bubbles. The heat flux for these four cases in Figure 3.28 is the same, i.e., 11 $kW/m^2$ but with different liquid core temperatures, i.e., 65 ºC for (a), 80 ºC for (b), 100 ºC for (c) and (d).

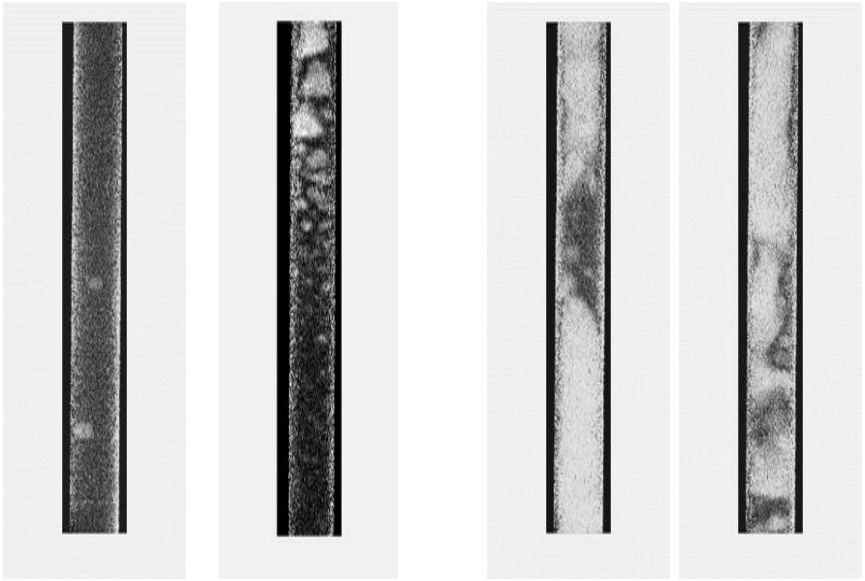

(a) (b) (c) (d)

Figure 3.28 X-ray images of bubbly flow ((a) and (b)) and slug flow ((c) and (d))

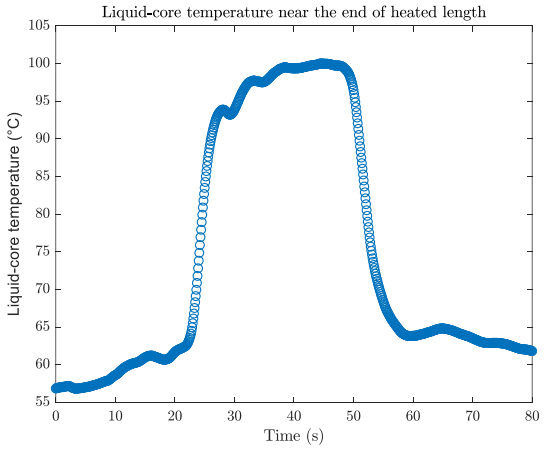


Figure 3.29 Liquid core temperature near the end of the heated length

To get the bubble sizes, five image process steps (Keplinger et al., 2017) are performed in Figure 3.30 as follows: (1) An raw image cut from the full field, (2) Image with subtracted a mean reference image with test section full of water, (3) Gaussian filter is applied to the images to reduce the noise signal, (4) Images are converted to binary images, and (5) Bubbles are extracted with interface.

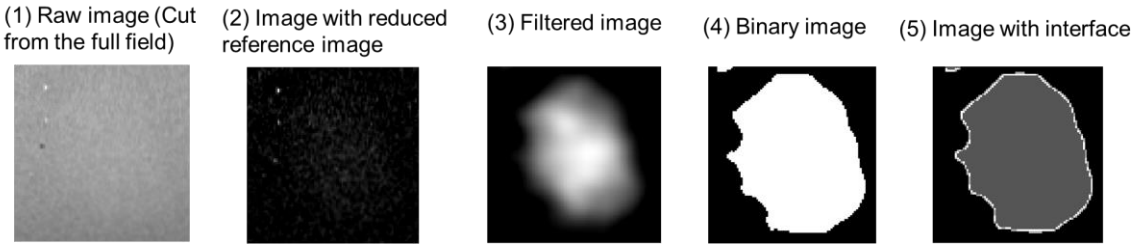


Figure 3.30 Image process steps

Figure 3.31 shows the intensity along the line “A”. It can be seen that in the bubble region, the intensity is larger, which is due to that the vapor has less attenuation on the photon beam than

liquid. The average bubble diameter in bubble flow in Figure 3.28(a) is calculated, i.e., 6 mm, and velocity is about 117 mm/s.

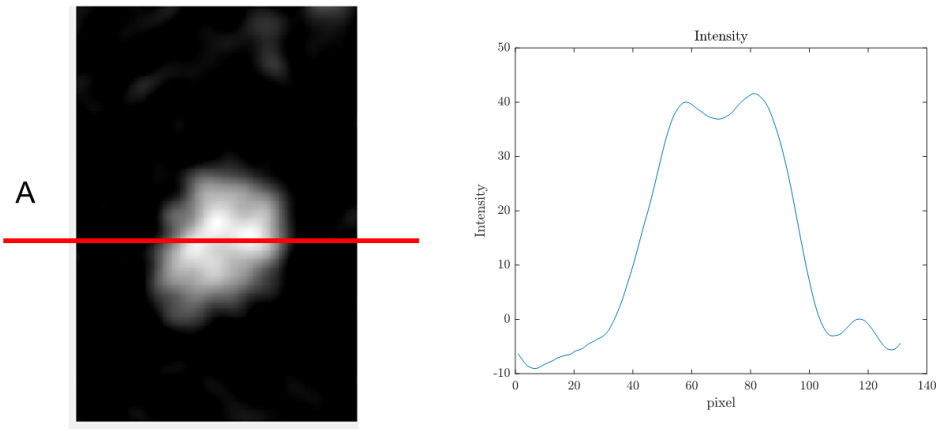


Figure 3.31 Intensity of X-ray image along line “A”

Figure 3.32 shows the cross-sectional-averaged void fraction calculated based on Eq. (12) with time at one location in the slug flow. It can be seen that the void fraction increases when bubbles pass the location and then decreases when liquid water passes the location.

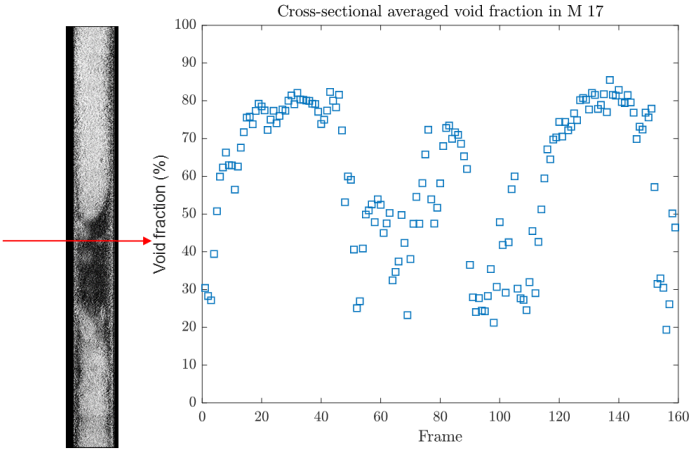


Figure 3.32 Cross-sectional-averaged void fraction in the slug flow

### 3.5.3 Subcooled flow boiling

To test the X-ray radiography system under quasi-steady-state conditions, subcooled flow boiling tests are performed in the PCHT test facility. The system pressure was kept at 17 psia, mass flux at 420 kg/m$^2$-s, and inlet subcooling at 20 ºC. The frame rate of the X-ray radiography system is 200 Hz. Figure 3.33 shows the convergence study of count rate in subcooled flow boiling. It can be seen that the mean count rate and the sample standard deviation of count rate converge to constant values.

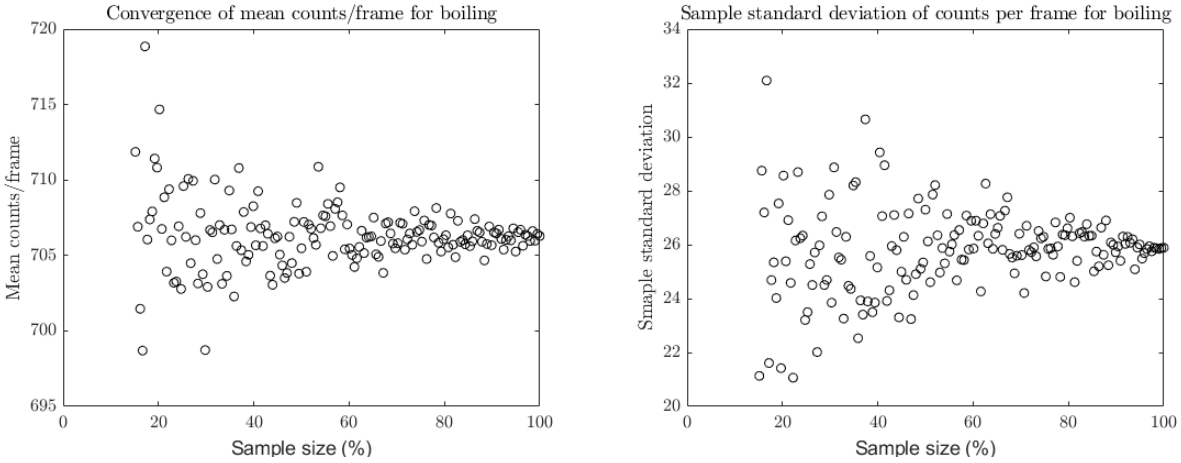


(a) Mean count rate (b) Sample standard deviation of count rate

Figure 3.33 Convergence study of count rate in subcooled flow boiling

Figure 3.34 shows the cross-sectional-averaged void fraction with frame for two different heat flux values. It can be seen that the void fraction is relative constant with time and the mean value is 20% and 25% for the heat flux of 170 and 200 kW/m$^2$, respectively. The statistical uncertainty of the cross-sectional-averaged void fraction is 5% at 95% confidence level as calculated by Eq. (2-10).

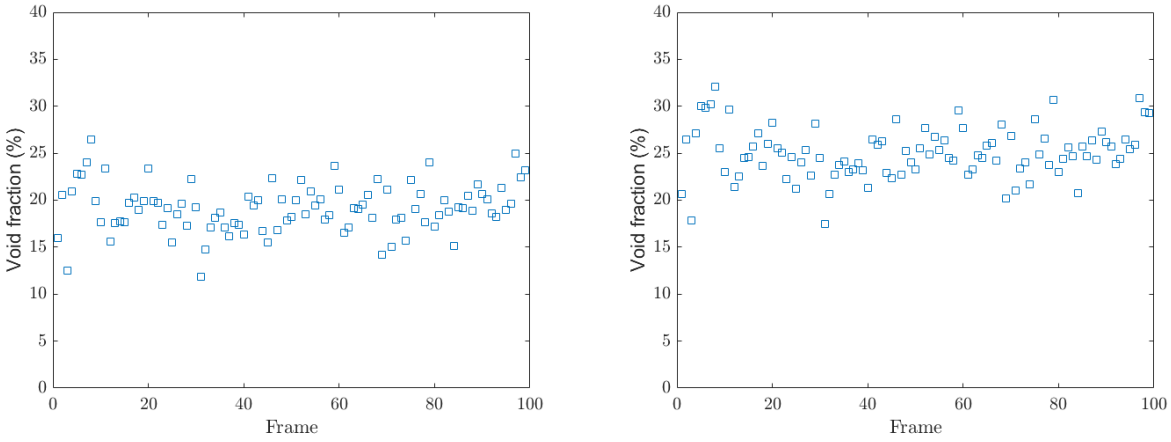


(a) Heat flux: 170 kW/m$^2$ (b) 200 kW/m$^2$

Figure 3.34 Cross-sectional-averaged void fraction with frame

# Chapter 4 Post-CHF Heat Transfer Experiments

## 4.1 Experimental Methods

### 4.1.1 Experimental procedure

To study the heat transfer characteristics in the post-CHF regimes, reflooding and dry patch tests were performed in the tubular test section in the PCHT test facility. In the reflooding test, the test section was initially heated to between 300 and 600 ºC by DC Power Supply #2 in Figure 2.5 at the atmospheric pressure without water flowing through the test section but through a bypass, and then subcooled water (Inlet subcooling of 20 ºC) was diverted from the bypass to the bottom of the test section to quench the test section, during which the mass flux increased from 0 to 400 kg/m$^2$-s. The wall temperatures were recorded and stored in the computer.

In the dry patch tests, DC Power Supplies #1 and 2 in Figure 2.5 are turned on but DC Power Supply #3 is off. Subcooled water with inlet subcooling of 30 ºC flows through the test section at a mass flux of 150 kg/m$^2$-s at 22 psia. The power of DC Power Supply #1 is controlled by a PID controller, and the power of DC Power Supply #2 is increased from 0 to 18 kW until the dry patch is observed from the profile of the wall temperature.

4.1.2 Data reduction

Based on the experimental data, the heat flux, heat transfer coefficients, heating rate and cooling rate of the test section, and temperature gradient of the test section are studied in the post-CHF regimes. The local heat flux to the fluid is calculated based on an energy balance of the test section from the measured wall temperatures and the heating power of the DC power supply to the test section, with the axial heat conduction considered in the calculation, as:

$$q''_{in} = \frac{P_{DC} - \dot{Q}_{loss}}{\pi L d_i} + \frac{\partial}{\partial z}\left( k_w \frac{\partial \bar{T}_w}{\partial z} \right) \frac{d_o^{\,2} - d_i^{\,2}}{4 d_i} - \rho_w c_w \frac{\partial \bar{T}_w}{\partial t} \frac{d_o^{\,2} - d_i^{\,2}}{4 d_i}, \quad (4\text{-}1)$$

where $q''_{in}$ is the heat flux from the test section to the fluid based on the inner surface area of the test section (W/m$^2$); $P_{\mathrm{DC}}$ the heating power to the test section from the DC power supply (W); $\dot{Q}_{loss}$ the heat losses from the test section to the ambient (W); $\bar{T}_w$ the cross-sectional area-averaged wall temperature of the test section (K); $k_w$ the thermal conductivity of the test section wall (W/m-K); $\rho_w$ the density of the test section wall (kg/m$^3$); $c_w$ the specific heat capacity of the test section (J/kg-K); $d_o$ the outer diameter of the test section (m); $d_i$ the inner diameter of the test section (m); $L$ the heated length of the test section (m); $z$ the elevation of the test section (m); and $t$ time (s).

The heating power is assumed uniform along the test section length. The second term on the right-hand side of Eq. (4-1) represents the axial heat conduction in the test section due to the axial temperature gradient. The third term on the right-hand side of Eq. (4-1) corresponds to the rate of heat released from the test section. In the experiments, only the outer surface temperatures of the test section wall are measured. To make certain that the attached thermocouples work properly, a

benchmark test is performed as described in Section 2.5.2. The inner surface temperature is derived from the outer surface temperature and the heat flux as:

$$T_{w,in} = T_{w,out} - \frac{q''_{in} d_i}{\left(d_o^2 - d_i^2\right)k}\left[\frac{d_o^2}{2}\ln\left(\frac{d_o}{d_i}\right) - \frac{d_o^2 - d_i^2}{4}\right], \tag{4-2}$$

where $T_{w,in}$ is the inner surface temperature of the test section (K) and $T_{w,out}$ the outer surface temperature of the test section (K). The cross-sectional area-averaged wall temperature is calculated as:

$$\bar{T}_w = \frac{4}{\pi\left(d_o{}^2 - d_i{}^2\right)}\int_{d_i/2}^{d_o/2} T_w \cdot 2\pi r \mathrm{d}r \,. \tag{4-3}$$

Equations (4-1) to (4-3) are solved through iteration to obtain the inner surface temperature and heat flux to the fluid. The heating power to the test section, $P_{\mathrm{DC}}$, is calculated as:

$$P_{DC} = UI\,, \tag{4-4}$$

where $U$ is the measured voltage drop across the test section (V) and $I$ the DC current recorded from the DC power supply (A). The heat losses from the test section to the ambient are calculated as:

$$\dot{Q}_{loss} = \frac{2\pi k_{ins} L\left(T_{w,out} - T_{ins}\right)}{\ln\left(d_o/d_i\right)}\,, \tag{4-5}$$

where $k_{ins}$ is the thermal conductivity of the insulation (W/m-K) and $T_{\mathrm{ins}}$ the outer surface temperature of the insulation on the test section (K). The convective heat transfer coefficient, $h_c$, is calculated based on the saturation temperature of the fluid and inner surface temperature of the test section as:

$$h_c = \frac{q''_{in} - q''_{rad}}{T_{w,in} - T_{sat}}, \tag{4-6}$$

where $q''_{rad}$ is the radiative heat flux from the test section to the fluid (W/m$^2$) and $T_{\mathrm{sat}}$ the saturation temperature of the fluid (K). The radiative heat flux $q''_{rad}$ is calculated as:

$$q''_{rad} = \frac{\sigma_{SB}\left(T^4_{w,in} - T^4_{sat}\right)}{\frac{1}{\varepsilon_l} + \left(\frac{1}{\varepsilon_w} - 1\right)}, \tag{4-7}$$

where $\sigma_{SB}$ is Stefan-Boltzmann constant, 5.670367 × 10$^{-8}$ (kg/s$^3$-K$^4$); $\varepsilon_l$ the emissivity of the liquid water; and $\varepsilon_w$ the emissivity of the heated wall inner surface.

### 4.1.3 Uncertainty analysis

From Eqs. (4-1) to (4-7), it can be seen that a number of sources contribute to the uncertainty in the convective heat transfer coefficient, including uncertainties in the temperature measurements by the thermocouples, the voltage and current measurements, thermophysical properties of the test section wall material, and calculation of the heat losses, etc. The thermocouples have an accuracy of 1.1°C or 0.4% of the reading at 95% confidence level, depending on which is greater, reported by the manufacturer. The voltage and current measurements have measurement inaccuracies of 0.004 V and 0.45 A both at 95% confidence level, respectively, reported by the manufacturer. The heat losses from the insulation surface is less than 2% of the total heating power. The uncertainty in calculating the heat transfer coefficient is mainly contributed by the wall temperature and heating power measurements, including the voltage and current measurements. In addition to the

measurement accuracies reported by the manufacturers, the statistical uncertainty at 95% confident level (twice of sample standard deviation) in the measurement is also considered in the uncertainty calculation. The uncertainty of each component is calculated as:

$$\delta X = \sqrt{\delta X_{ins}{}^2 + \delta X_{stat}{}^2}\,, \tag{4-8}$$

where $\delta X$ is the uncertainty of quantity $X$; $\delta X_{ins}$ the instrument uncertainty as reported by the manufacturer; and $\delta X_{stat}$ the statistical uncertainty (twice of sample standard deviation) calculated from the measurement results. The uncertainty in calculating the heat transfer coefficient can be obtained based on the uncertainty propagation principle as:

$$\delta h_c = \sqrt{\left(\frac{\partial h_c}{\partial U}\right)^2 \delta U^2 + \left(\frac{\partial h_c}{\partial I}\right)^2 \delta I^2 + \left(\frac{\partial h_c}{\partial T_{w,in}}\right)^2 \delta T_{w,in}{}^2}\,, \tag{4-9}$$

where $\delta h_c$ is the uncertainty of the convective heat transfer coefficient (W/m$^2$-K); $\delta U$ the uncertainty of the measured voltage across the test section (V); $\delta I$ the uncertainty of the measured current on the test section (A); $\delta T_{w,in}$ the uncertainty of the inner surface temperature of the test section (°C). By considering the instrument uncertainty and statistical uncertainty in the measurements, the relative uncertainty of the convective heat transfer coefficient, $\delta h_c / h_c$, is less than 10% in the film boiling region at 95% confidence level.

## 4.2 Reflooding Test

### 4.2.1 Wall temperature

In the reflooding test, the test section was initially heated to higher temperatures, i.e., 300 to 600 ºC at different elevations, at the atmospheric pressure without water flowing through the test section but through a bypass, and then subcooled water (Inlet subcooling of 20 ºC) was diverted from the bypass to the bottom of the test section to quench the test section. The wall temperatures were recorded and stored in the computer. Figure 4.1 shows the outer surface temperature profile of the test section in the reflooding test. It can be seen that the wall temperatures initially stay relatively constant until about 5 s after initiation of reflooding, and then decrease slowly due to precursory cooling by the steam or two-phase mixture in dispersed flow film boiling (DFFB) regime (Edelman et al., 1985), indicating the onset of entrainment (Yu, 1978). At a given elevation, the decrease of the wall temperature continues until the tubular test section quenches. The wall temperature then gradually approaches a steady value. Near the quench front region within a short distance, the heat transfer pattern changes from film boiling via transition boiling into nucleate boiling.

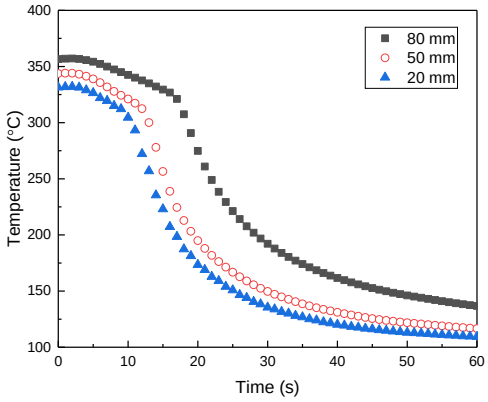


(a)

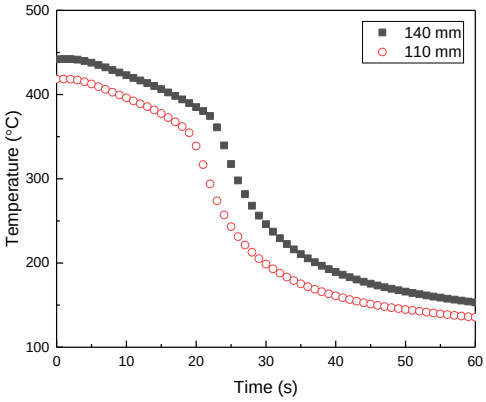


(b)

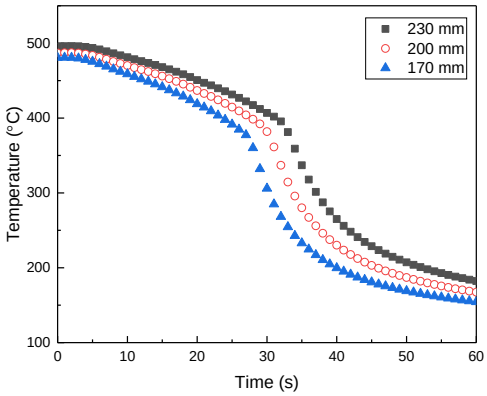


(c)

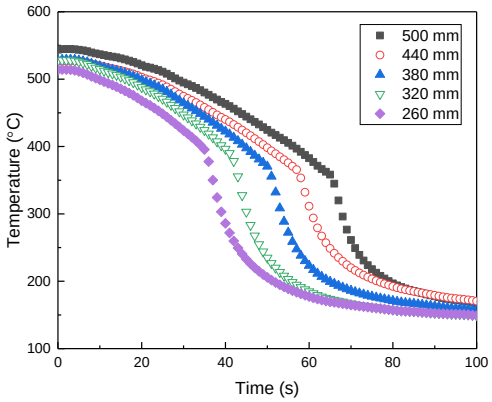


(d)

Figure 4.1 Outer surface temperature profile of the test section in the reflooding test

Figure 4.2 shows the outer surface temperature of the test section and its first order derivative at different elevations. The first order derivative of the wall temperature represents the cooling rate of the test section. The quench temperature is assumed to occur at the minimum value in the profile of the first order derivative of the wall temperature in Figure 4.2. Near the quench region (the region near the maximum cooling rate), the heat transfer characteristics are complicated, including film boiling, transition boiling, and nucleate boiling in a short time period and narrow region.

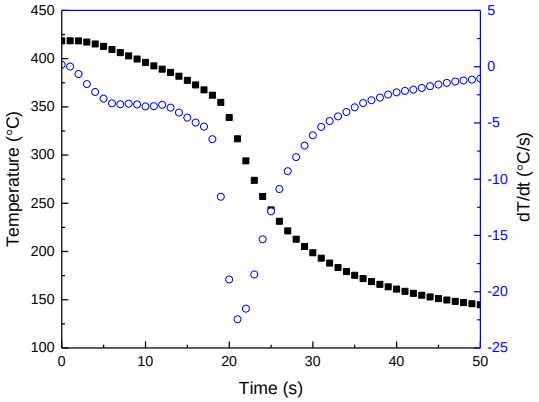


(a) $z$ = 110 mm

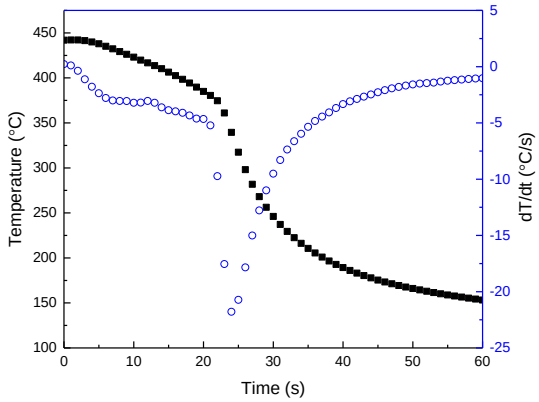


(b) $z$ = 140 mm

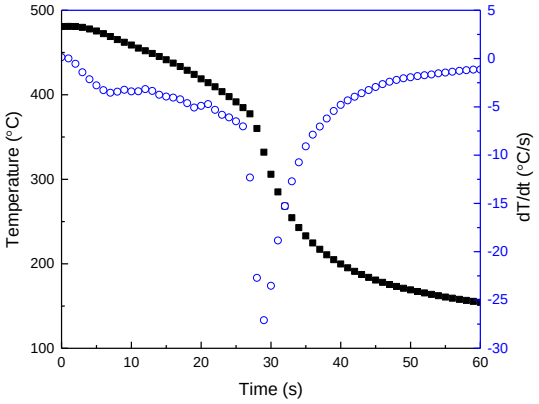


(c) $z$ = 170 mm

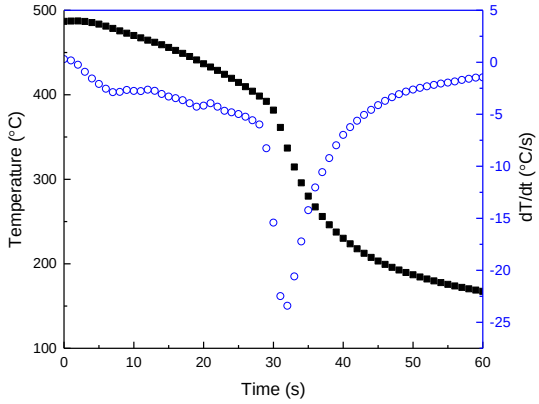


(d) $z$ = 200 mm

Figure 4.2 The outer surface temperature of the test section and its first order derivative at different elevations

Figure 4.3 shows the wall temperatures at different elevations of the test section with different times. It can be seen that at $t$ = 0 s, the wall temperature near $z$ = 0 mm is smaller, which is due to the heat conduction from the heated section of the test section to the unheated section. As the liquid water is injected into the test section, the wall temperature decreases gradually, and the test section is quenched progressively along the test section.

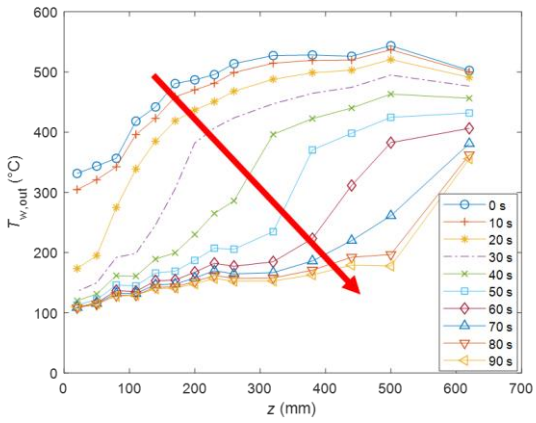


Figure 4.3 Wall temperatures at different elevations

Figure 4.4 shows the quench front location and quench time predicted from the profile of the first order derivative of the wall temperatures. It can be seen that the quench front is moving at an approximately constant rate of 8.8 mm/s.

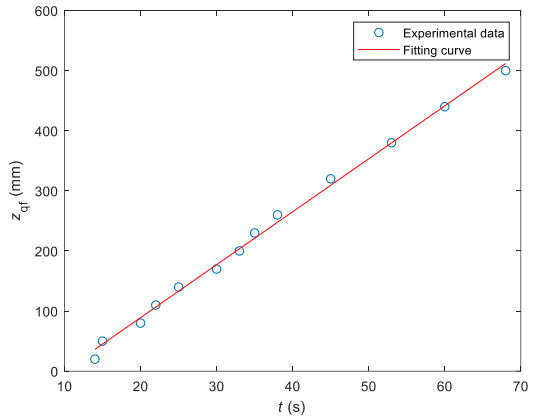


Figure 4.4 Quench front location and quench time

4.2.2 Heat flux

Figure 4.5 shows the total heat flux to fluid and heat flux to fluid due to heat release from test section calculated based on Eq. (2-1) at $z$ = 110 mm. From Figure 4.5, it can be seen that the total heat flux to fluid has a heat flux peak, which is due to the heat release from the test section. The heat release from the test section due to quenching plays a significant role in the total heat flux to fluid.

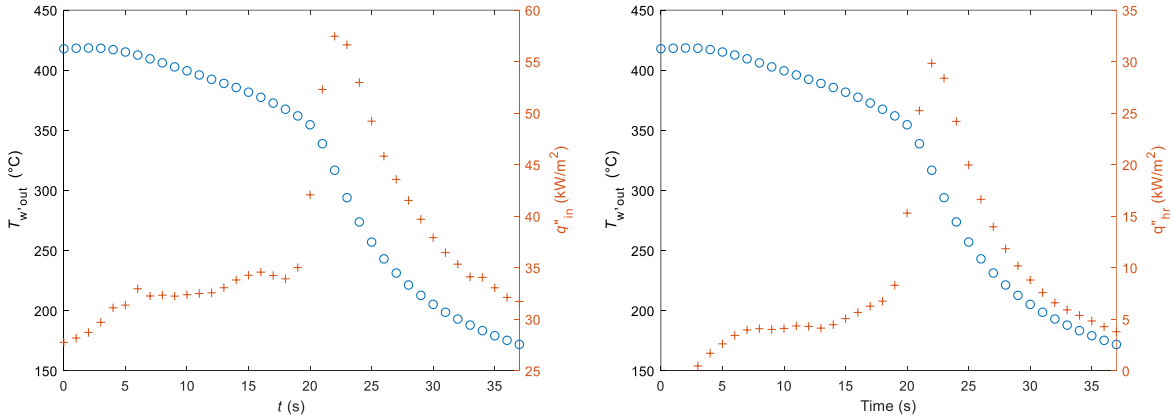


(a) (b)

Figure 4.5 (a) Total heat flux to fluid and (b) heat flux to fluid due to heat release from test section at $z$ =110 mm

### 4.2.3 Heat transfer coefficient

Figure 4.6 and Figure 4.7 show the wall temperature, convective heat transfer coefficient, and the first order derivative of the wall temperature at $z$ =110 mm. It can be seen that there is a sudden increase of the convective heat transfer coefficient. Comparing the profile of the convective heat transfer coefficient and the first order derivative of the wall temperature in Figure 4.7, the quench region occurs in a narrow region, where the convective heat transfer coefficient has a sudden

increase, corresponding to the time period between the onset of the fast cooling and the maximum cooling rate. In the quench region, the heat release from the test section is huge as shown in Figure 4.5(b) and the heat transfer mechanism is complex, including film boiling, transition boiling and nucleate boiling.

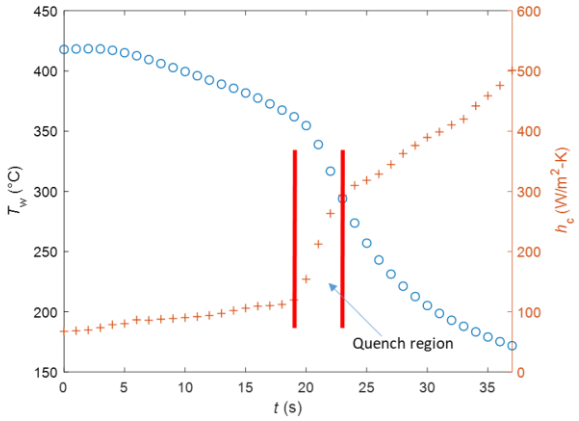


Figure 4.6 Wall temperature and convective heat transfer coefficient at $z$ =110 mm

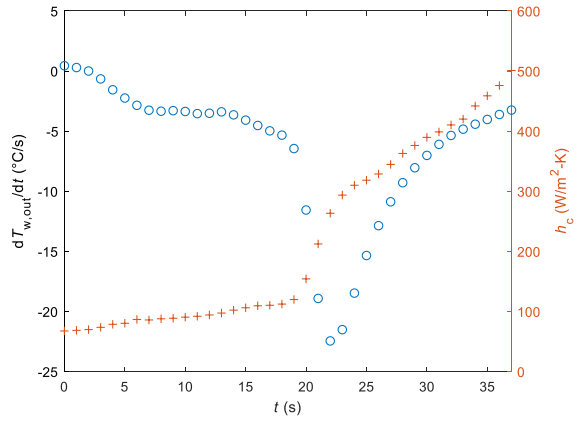


Figure 4.7 The first order of derivative of the wall temperature and convective heat transfer coefficient at $z$ =110 mm

In the reflooding test, the quench front is moving, and the location of the quench front is indicated from the wall temperature profiles. Figure 4.8 shows the convective heat transfer efficient

downstream of the quench front. It can be seen from Figure 4.8 that downstream of the quench front, the convective heat transfer coefficient decreases first and then increases. It is believed that just downstream of the quench front, the flow regime is IAFB regime. The region near the turning point of the convective heat transfer coefficient is the ISFB regime. Farther downstream of the quench front, the regime is DFFB regime where the convective heat transfer coefficient has a slight increase.

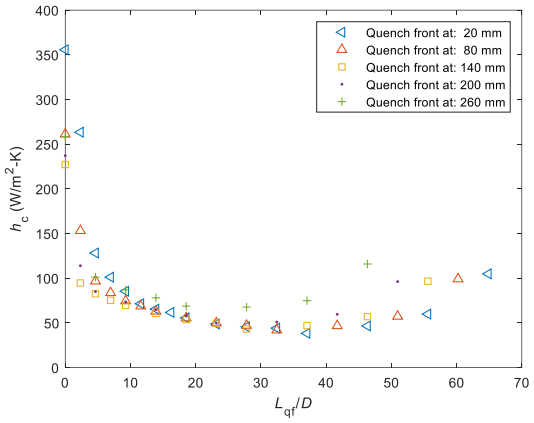


Figure 4.8 Convective heat transfer coefficient downstream of the quench front

Figure 4.9 shows the comparison of the total heat transfer coefficient between our experimental data and Yu's experimental data (Yu, 1978). Both the experimental data show that the total heat transfer coefficient decreases just downstream of the quench front. However, in Yu's experimental data, no flow regime transition is indicated from the heat transfer coefficient profile.

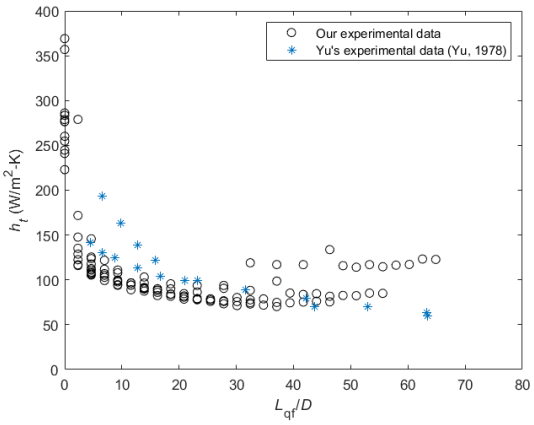


Figure 4.9 Comparison of our experimental data with Yu's experimental data (Yu, 1978)

Figure 4.10 shows the comparison of the convective heat transfer coefficient between our experimental data with Bromley's model (Bromley, 1950), i.e., Eq. (1-1). The heat transfer coefficient resulting from the Bromley's model is almost constant with the distance from the quench front. The Bromley's model results in film boiling heat transfer coefficient values about 200 W/m$^2$-K while the convective heat transfer coefficient in our experimental data decreases from 350 to 40 W/m$^2$-K and then increases to 100 W/m$^2$-K due to the flow regime transition.

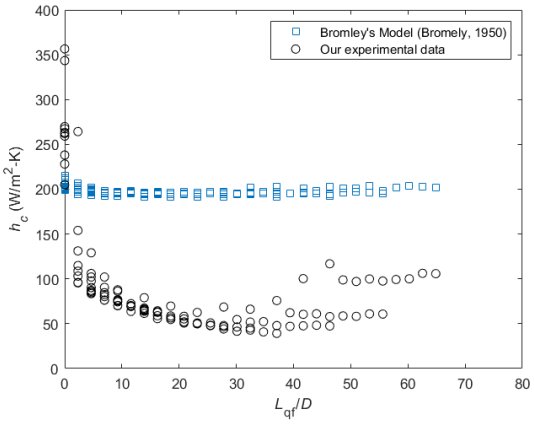


Figure 4.10 Comparison of our experimental data with Bromley's model

## 4.3 Dry Patch Tests

### 4.3.1 Wall temperature with time

During the dry patch tests, DC Power Supplies #1 and 2 are turned on but DC Power Supply #3 is off. Subcooled water with inlet subcooling of 30 ºC flows through the test section at a mass flux of 150 kg/m$^2$-s at 22 psia. The power of DC Power Supply #1 is controlled by a PID controller, and the power of DC Power Supply #2 is increased from 0 to 18 kW until the dry patch is observed. Figure 4.11 shows the variation of outer surface temperature of the test section with time at different elevations of the test section in the dry patch tests. The legend in Figure 4.11 shows the distance of each thermocouple from the top edge of the bottom notch. In Figure 4.11(a), at $t$ = 103 s, the wall temperature begins to increase at the distance of 20 mm from the top edge of the bottom notch and the measured outer surface temperature of the test section is up to 1,100 ºC. Changes in the slope, i.e., the time rate of change, of the wall temperature histories may indicate flow regime transitions. At a certain time, the wall temperature measured by one thermocouple increases rapidly to a maximum value and then decreases rapidly, corresponding to the formation and collapse of a dry patch. The profiles of the wall temperature indicate that, in general, the dry patches propagate from the bottom to the top in the test section, which leads to large temperature gradients in the axial direction of the test section (To be discussed in Section 4.3.2).

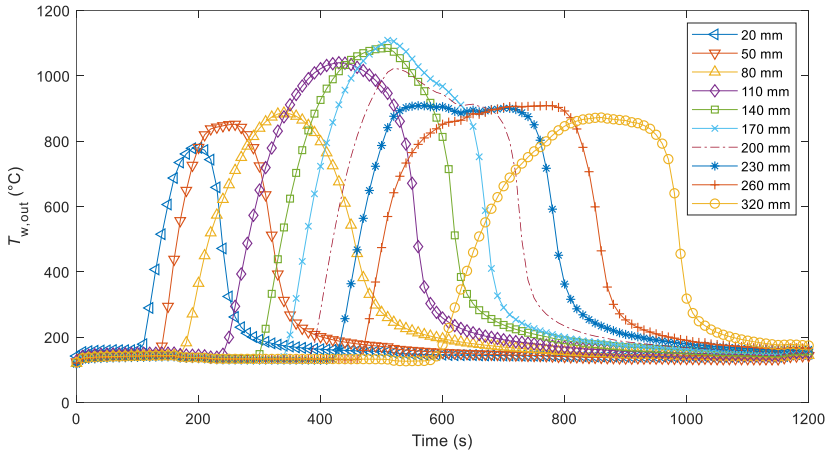


Figure 4.11 Wall temperature with time at different elevations of the test section in the dry patch tests

Figure 4.12 shows the wall temperatures and their first-order derivatives with respect to time at four elevations, 50, 110, 230 and 260 mm above the bottom notch, which have very similar trends. To explain the process of the formation and collapse of the dry patches, the wall temperature, and its first-order derivative with respect to time at the distance of 50 mm are described as follows. Before the time reaches 130 s, the wall temperature is relatively constant, and the flow is in nucleate boiling. After 130 s, the generation of the bubbles become faster than the departure of bubbles, causing the wall temperature and its first-order derivative to increase rapidly. Initially, the bubbles partially cover the inner surface of the test section wall around the elevation of the thermocouple, corresponding to the transition boiling or partial film boiling. At about 150 s, the first-order derivative of the wall temperature reaches its maximum value and the bubbles form a vapor film, covering the inner surface of the test section near the elevation of the thermocouple, which indicates a dry patch has formed and the local flow regime has transitioned from nucleate boiling to film boiling. As the thickness of the vapor film increases, the wall temperature continues

to increase until around 210 s and then maintains a relatively stable temperature value from 210 to 280 s. Then, the wall temperature begins to decrease, so does the thickness of the vapor film, due to the axial heat conduction in the test section. At about 320 s, the first-order derivative of the wall temperature reaches the smallest value, corresponding to the largest cooling rate, when the dry patch collapses. The two peaks (One peak and one valley) in the profile of the first-order derivatives of the wall superheat correspond to the largest heating rate and largest cooling rate of the test section wall, respectively. These two temperatures are named as the dry temperature, i.e., $T_{\mathrm{d}}$, and quench temperature, $T_{\mathrm{q}}$, respectively.

Based on the above discussion, the process of the formation and collapse of dry patches can be divided into seven regions as shown in Figure 4.13. In Region I, the flow is under nucleate boiling with no presence of a vapor film. In Region II, the wall temperature increases rapidly, and a vapor film partially covers the inner surface of the test section wall, corresponding to the transition boiling. In Region III, the vapor film fully covers, locally, the inner surface of the test section wall and continues to grow in its thickness. In Region IV, the vapor film is relatively stable in its thickness but grows in its area covering the test section surface. In Region V, the thickness of the vapor film decreases but still fully covers the inner surface of the test section wall until collapses. In Region VI, the vapor film partially covers the inner surface of the test section wall, similar to Region II, but the wall temperature decreases. In Region VII, the vapor film collapses and disappears. Table 4.1 summarizes the flow patterns and dominant heat transfer modes in these seven regions.

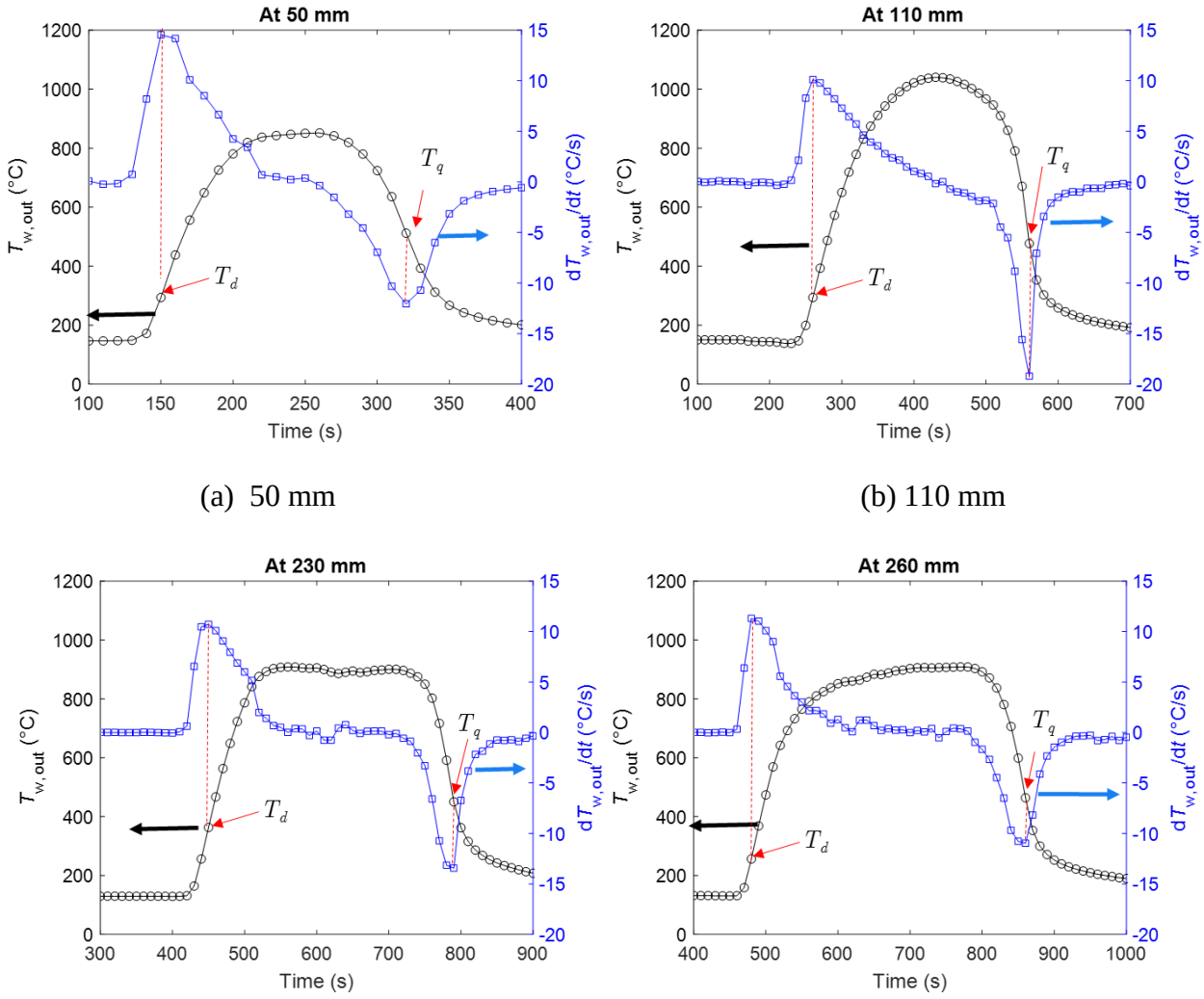


(a) 50 mm

(b) 110 mm

(c) 230 mm

(d) 260 mm

Figure 4.12 Wall superheat and its first-order derivative with respect to time at different elevations above the bottom notch

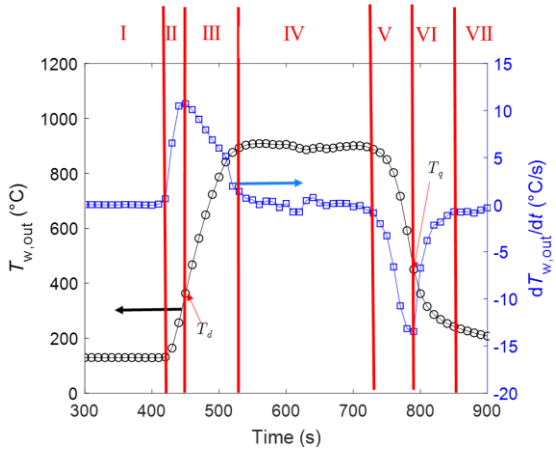


Figure 4.13 Seven regions based on the measured wall temperatures

Table 4.1 Flow patterns and heat transfer regions in the process of dry patch formation and collapse

| **Region** | **Flow pattern** | **Heat transfer mode** |
|---|---|---|
| I | No vapor film | Nucleate boiling |
| II | Partial vapor film | Transition boiling |
| III | Vapor film growth | Film boiling |
| IV | Stable vapor film | Steady-state film boiling |
| V | Vapor film shrinking | Film boiling |
| VI | Partial vapor film | Transition boiling |
| VII | Vapor film collapse | Nucleate boiling |

Figure 4.14 shows the dry temperature, quench temperature, and maximum wall temperature at different elevations along the test section. The three temperatures have similar trends, and the dry

and quench temperatures increase as the maximum temperature increases. The dry temperature is smaller than the quench temperature. Based on the above analysis of the process of formation and collapses of dry patches, the dry temperature $T_{\mathrm{d}}$ is close to the critical heat flux temperature $T_{\mathrm{CHF}}$ while the quench temperature $T_{\mathrm{q}}$ is close to the minimum film boiling temperature $T_{\mathrm{MFB}}$.

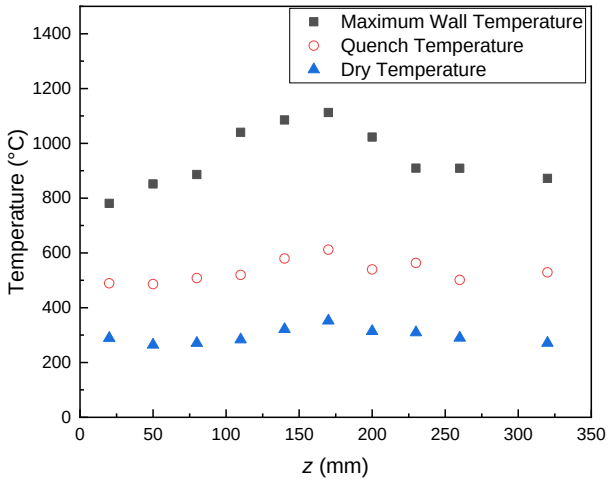


Figure 4.14 Dry temperatures, quench temperatures, and maximum wall temperatures

The dry patches propagate along the axial direction of the test section as shown in Figure 4.11. Figure 4.15 shows the time and elevation at which $T_{\mathrm{d}}$ occurs, corresponding to the formation of the dry patch. The correlation between a fitted linear curve and data points is 0.9935 and the slope is 0.6 (mm/s), which indicates that the dry patch propagates in the test section at a constant speed of 0.6 mm/s. Figure 4.16 shows the duration time of the dry patch at different elevations. The duration time is defined as the period between the times when $T_{\mathrm{d}}$ and $T_{\mathrm{q}}$ occur. It can be seen that

the duration time of the dry patch, in general, increases along the flow direction, which indicates that the dry patch grows as it moves upward.

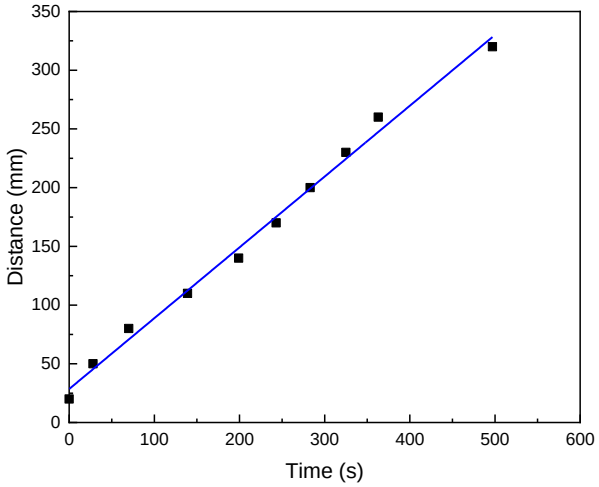


Figure 4.15 The time and elevation at which $T_{\mathrm{d}}$ occurs

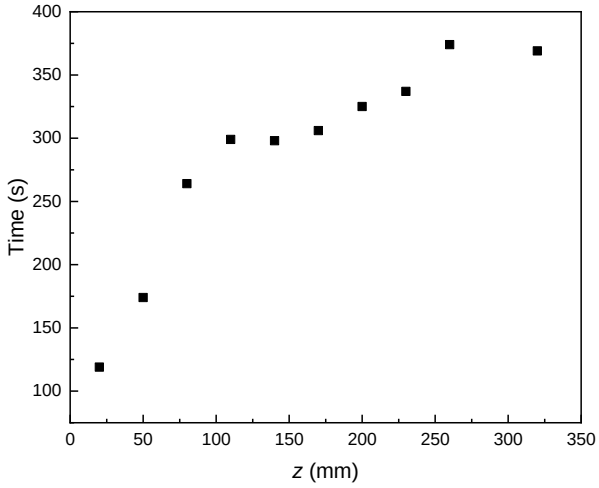


Figure 4.16 Duration time of the dry patch at different elevations

4.3.2 Wall temperature gradient along the axial direction of the test section

Figure 4.17 shows the measured wall temperatures along the axial direction of the test section at seven different times from the transient initiation. To explain temperature variations at a specific elevation clearly, the wall superheat at the distance of 110 mm is described as follows. At 100 and 144 s, the wall superheat is small and almost constant. At 254 s, the wall temperature increases until it reaches the maximum value at 425 s, corresponding to the growth of the dry patch. Due to the axial heat conduction, the wall temperature becomes smaller at 509 s, which indicates that the thickness of the vapor layer has decreased. At 725 and 854 s, the wall temperatures are lower than 200 °C and the dry patch has collapsed. From the profiles in Figure 4.17, it can be seen that the temperatures at different elevations do not increase or decrease in a synchronized manner, which results in large temperature gradients along the test section wall.

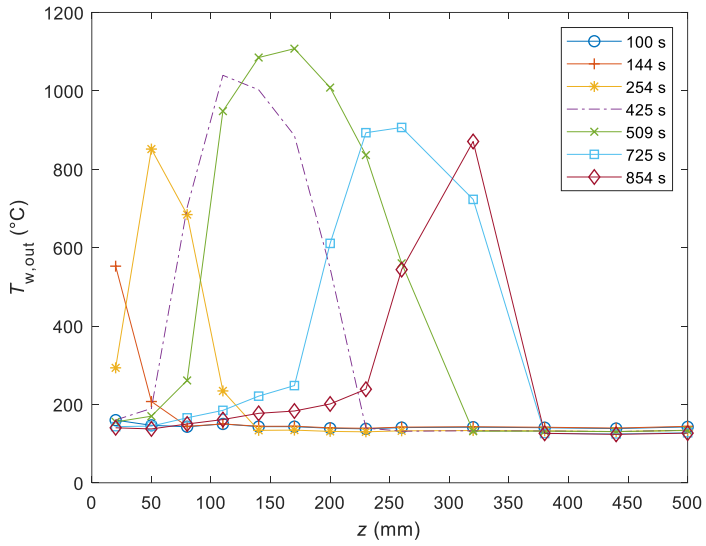


Figure 4.17 Wall temperature along the axial direction of the test section at different times

Figure 4.18 shows the axial temperature gradient along the test section at four different times into the transient. It can be seen that the maximum temperature gradient reaches 15 °C/mm, which may cause large thermal stresses in the test section. The profiles of the axial temperature gradient have two peaks (One peak and one valley) at each specific time, corresponding to the largest and smallest temperature gradients, respectively. As can be seen from Figure 4.18, these two peaks move along the axial direction of the test section over time.

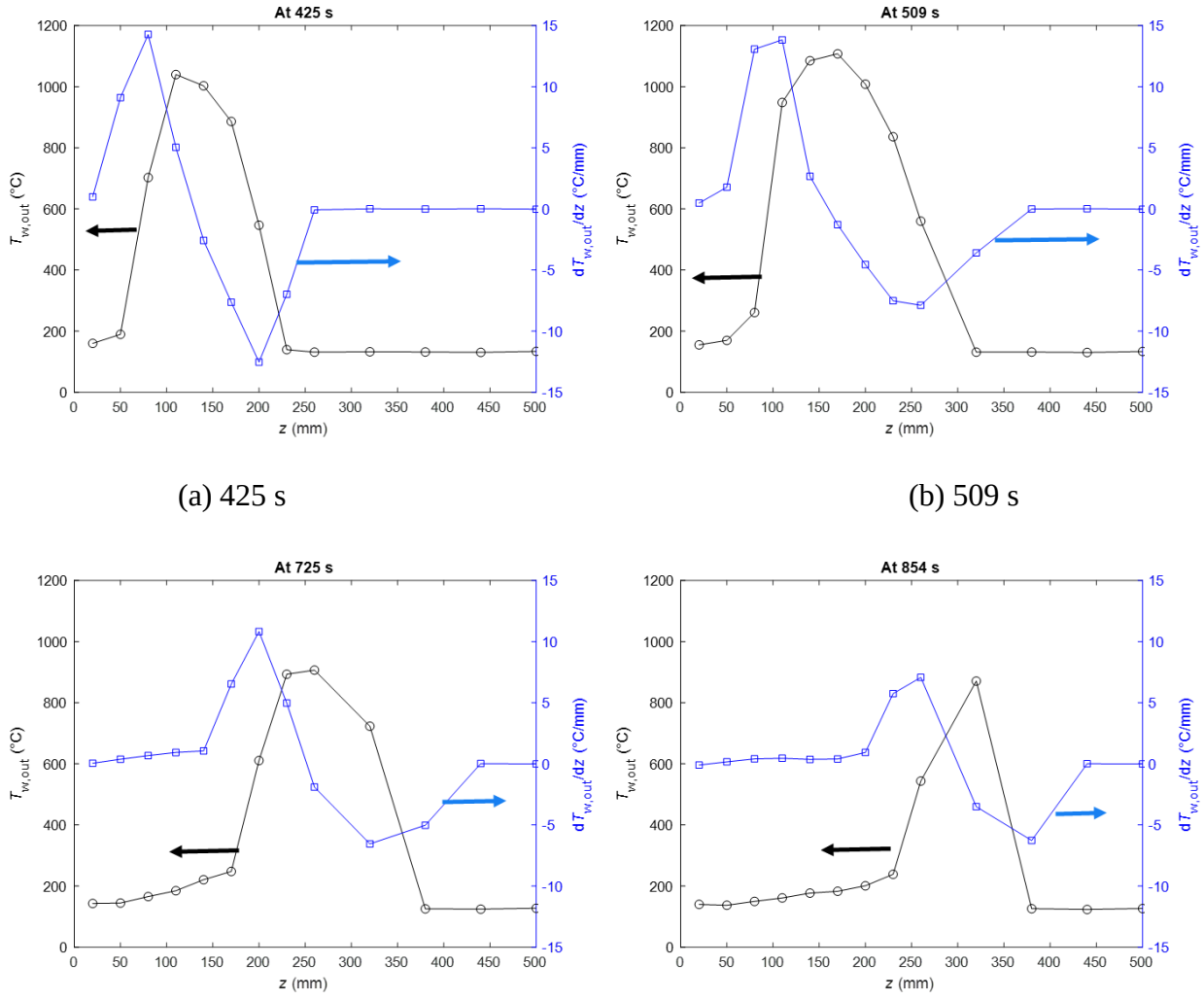


(a) 425 s

(b) 509 s

(c) 725 s

(d) 854 s

Figure 4.18 Wall temperatures and computed wall temperature gradients

### 4.3.3 Convective heat transfer coefficients and wall superheats

For the dry patches, there exist three heat transfer mechanisms, convective heat transfer, radiative heat transfer, and heat conduction due to the axial temperature gradient in the test section. Figure 4.19 shows the wall superheats (defined as the wall inner surface temperature minus the water saturation temperature) and convective heat transfer coefficients, calculated per Eq. (4-6), at different elevations. Before the dry patch forms, the convective heat transfer coefficient values are large, and the corresponding flow regime is in nucleate boiling. At a certain time, the convective heat transfer coefficient decreases rapidly, which indicates the formation of a dry patch. Then the convective heat transfer coefficient value keeps approximately constant for a certain period of time, corresponding to the stable dry patch, i.e., Region IV in Figure 4.13 and Table 4.1, where the convective heat transfer coefficient is small, less than 1,000 $W/m^2$-K, until the dry patch collapses and the convective heat transfer coefficient increases. Prior to the formation or after the collapse of the dry patch, the convective heat transfer coefficient is relatively large, which is due to the small thickness of the vapor film and the disturbance of the growth and shrinkage of the vapor film. After the dry patch collapses, the convective heat transfer coefficient increases as the flow transitions back to nucleate boiling.

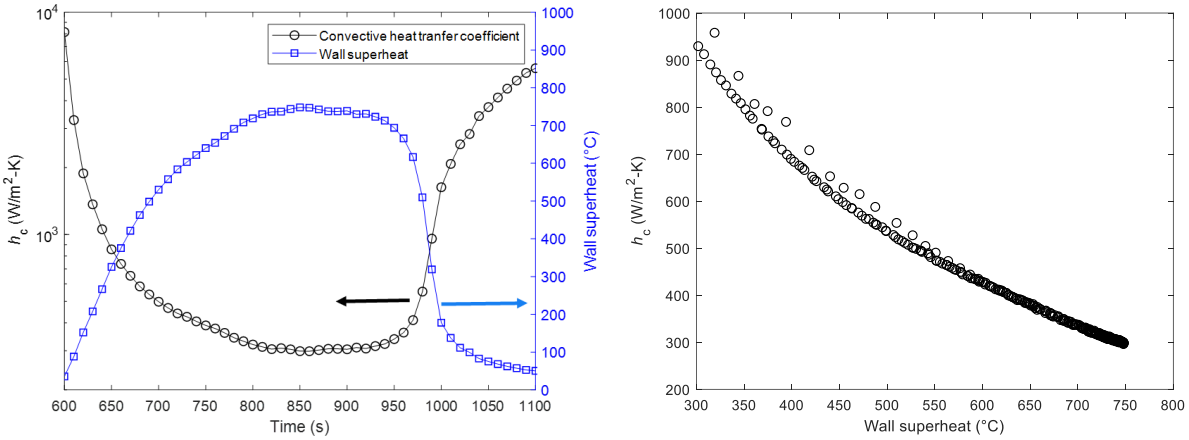


(a) (b)

Figure 4.19 Wall superheats and convective heat transfer coefficients at 320 mm

4.3.4 Comparison with correlations

Based on the convective heat transfer coefficients presented in Figure 4.19, the flow pattern has a stable period when the flow is in the stable dry patch region, i.e., Region IV in Table 4.1. The computed convective heat transfer coefficient values in the stable film boiling region are compared with Bromley's correlation (Bromley, 1950), Berenson's correlation (Berenson, 1961), and the correlation in the nuclear reactor thermal hydraulics analysis code COBRA-TF or CTF (Salko et al., 2017).

Figure 4.20 shows a comparison of the convective heat transfer coefficient in film boiling between our experimental data and these three correlations. It can be seen that the convective heat transfer coefficients calculated from these three correlations are not strong functions of the wall superheats, i.e., relatively constant for the wall superheat span from about 400 to 1,000 ºC, while the heat transfer coefficient values obtained from the experiments increase as the wall superheats decrease.

In our experiments, the wall temperatures are not uniform at different elevations as shown in Figure 4.11 as the dry patches propagate downstream, which causes some disturbance and improves the convective heat transfer. The thickness of the vapor film changes as the wall temperature changes with time. The growth and shrinkage of the vapor film as well as the temperature gradients along the axial direction in the test section wall result in some disturbance, which enhances the convective heat transfer. At high wall superheats, the vapor film is more stable, and the effect of the disturbance is relatively small. As the wall superheat decreases, the effect of the disturbance becomes more significant. Therefore, the differences between the convective heat transfer coefficients calculated using our experimental data presented in this research and these three correlations become larger as the wall superheat decreases. As the wall temperature increases, radiative heat transfer becomes more significant and the thickness of the vapor film increases, which reduces the convective heat transfer coefficient. The comparison of the experimental data with the heat transfer correlations shows that the motion of the dry patch will enhance the heat transfer.

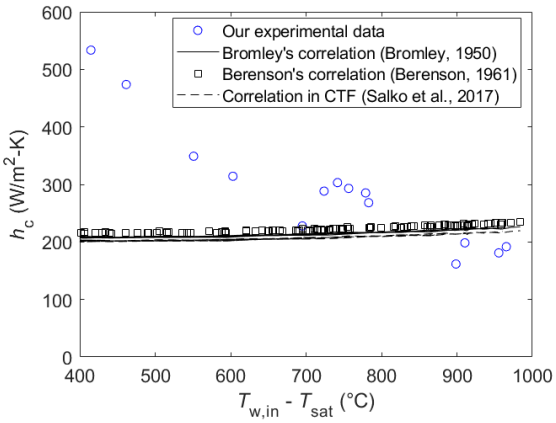


Figure 4.20 Comparison of the convective heat transfer coefficients between the current experiments and three correlations

# Chapter 5 Two-Fluid Modeling of the IAFB Regime

## 5.1 1D Two-Fluid Model

Due to the existence of thermal non-equilibrium conditions in the IAFB regime, the two-fluid model, which is well suited for weakly coupled two-phase flow problems, is selected to predict the wall temperature and void fraction. Heat transfer and hydrodynamic characteristics in the IAFB regime have been intensively studied using the two-fluid model (Analytis and Yadigaroglu, 1987; Wang et al., 1988; Cachard, 1996; Hammouda et al., 1997; El Nakla et al., 2010), which contains the conservation equations for the liquid and vapor phases coupled with a series of closure models, including the wall heat transfer and friction/shear, and interfacial heat transfer and friction/shear. It is principally the closure models that determine the accuracy of the predictions by the two-fluid model. Currently, most of the models for the interfacial friction in the IAFB regime are obtained from the annular two-phase flow experimental data instead of the IAFB experimental data due to the difficulties of obtaining the phasic velocities in the IAFB experiments, especially with water as the working fluid. Due to lack of the information for the liquid-core temperature in the IAFB regime, most of the existing models for the interfacial heat transfer are ad hoc and subject to considerable uncertainties. Therefore, the existing correlations/models used for the interfacial friction factor and interfacial heat transfer in the IAFB regime need to be evaluated and/or potentially improved by experimental data in the IAFB regime. For the flow regime transition from IAFB to ISFB regimes, void fraction is usually used as a criterion for the termination of the IAFB

regime, such as 0.3, 0.4, 0.5, or 0.6. Physics-based criteria for the flow regime transition therefore need to be developed.

In this Chapter, the conservation equations of the 1-D two-fluid model for the IAFB regime are presented and the closure models are benchmarked and improved with the experimental data in the IAFB regime. In the 1-D two-fluid modeling of the IAFB regime, the following assumptions are applied:

(1) The flow is at a steady state.

(2) The pressures in the vapor and liquid phases are the same at the same flow cross section.

(3) No liquid droplets are entrained in the vapor film and no vapor bubbles are entrained in the liquid core.

(4) There is no direct liquid-wall contact.

(5) The vapor-liquid interface is at saturation.

(6) The vapor-liquid interface is smooth.

(7) Liquid is in the center of the flow channel and vapor covers the heated surface.

The mass equations, momentum equations, and energy equations for the 1-D two-fluid model in the IAFB regime are summarized as follows:

$$\frac{\mathrm{d}}{\mathrm{d}z}(\rho_v v_v \alpha) = \Gamma''', \tag{5-1}$$

$$\frac{\mathrm{d}}{\mathrm{d}z}\left[\rho_l v_l (1-\alpha)\right] = -\Gamma''', \tag{5-2}$$

$$\frac{d}{dz}(\rho_v v_v v_v \alpha) = \Gamma''' v_l - \alpha \frac{dp}{dz} - \frac{\tau_w P_w}{A} - \frac{\tau_i P_i}{A} - \rho_v g \alpha\,, \tag{5-3}$$

$$\frac{\mathrm{d}}{\mathrm{d}z}\left[\rho_l v_l v_l (1-\alpha)\right] = -\Gamma''' v_l - (1-\alpha)\frac{\mathrm{d}p}{\mathrm{d}z} + \frac{\tau_i P_i}{A} - \rho_l g (1-\alpha)\,, \tag{5-4}$$

$$\frac{\mathrm{d}}{\mathrm{d}z}\left(\rho_v v_v h_v \alpha\right) = \Gamma''' h_v + \frac{q''_{wv} P_w - q''_{vi} P_i}{A}\,, \tag{5-5}$$

$$\frac{\mathrm{d}}{\mathrm{d}z}\left[\rho_l v_l (1-\alpha) h_l\right] = \frac{q''_{li} P_i}{A} - \Gamma''' h_l, \tag{5-6}$$

where $\alpha$ is the void fraction; $\rho_k$ the density of the k$^{th}$ phase (kg/m$^3$); $v_k$ the velocity of k$^{th}$ phase (m/s); $\Gamma'''$ the vapor generation rate per volume (kg/m$^3$-s); $p$ the pressure (pa); $\tau_w$ the wall friction (Pa); $\tau_i$ the interfacial friction (Pa); $P_w$ the perimeter of the flow channel (m); $P_i$ the perimeter of the liquid-vapor interface (m); $A$ the cross section area (m$^2$); $g$ the gravitational acceleration (m/s$^2$); $h_k$ the enthalpy of the k$^{th}$ phase (kJ/kg); $q''_{wv}$ the heat flux from wall to vapor (kW/m$^2$); $q''_{vi}$ the heat flux from vapor to liquid-vapor interface (kW/m$^2$); $q''_{li}$ the heat flux from liquid-vapor interface to liquid (kW/m$^2$). As can be seen from the above conservation equations, the closure models include wall heat transfer, interfacial heat transfer, wall friction, and interfacial friction. Another closure model is the flow regime transition criteria, which is to determine the termination of the IAFB regime. This Chapter focuses on the study of the liquid-side interfacial heat transfer, interfacial friction, and flow regime transition criteria.

## 5.2 Liquid-side Interfacial Heat Transfer

### 5.2.1 Data reduction method

The liquid-side interfacial heat transfer is necessary to model the IAFB regime using the 1-D two-fluid model. In the previous 1-D two-fluid models used by Analytis and Yadigaroglu (1987) and Hammouda et al. (1997), the Dittus-Boelter correlation was used for the liquid-side interfacial heat

transfer calculation. In the current study, a new correlation is developed for the liquid-side Nusselt number based on Stewart's experimental data (Stewart, 1981). The liquid-side Nusselt number in the IAFB regime is defined as (Kelly, 2015):

$$\mathrm{Nu}_{li} = \frac{q''_{li} D_c}{\Delta T_{sub} k_l}, \tag{5-7}$$

where $D_c$ is the liquid core diameter in the IAFB regime (m); $k_l$ the thermal conductivity of the liquid (W/m-K); and $\Delta T_{sub}$ the liquid subcooling (°C). Here, the liquid core is assumed to have a cylindrical shape with a diameter $D_c$.

To solve Eq. (5-7), Kelly (2015) made two assumptions to analyze experimental data since neither the liquid-side heat flux nor the liquid subcooling was measured in the existing experiments: (1) The interfacial heat flux was approximated by the wall heat flux and (2) the liquid subcooling was calculated from the equilibrium quality. In the current study, the liquid-side heat flux is calculated without these two assumptions. Instead, the vapor temperature is assumed to be the arithmetic mean of the wall temperature and water saturation temperature, and the liquid temperature is obtained by solving Eq. (5-8) as:

$$q''_w = \left[ \Gamma'''\left(h_v - h_l\right) + G_v c_{p,v} \frac{\mathrm{d}T_v}{\mathrm{d}z} + G_l c_{p,l} \frac{\mathrm{d}T_l}{\mathrm{d}z} \right] \frac{A_c}{P_w}, \tag{5-8}$$

where $q''_w$ is the total wall heat flux (W/m$^2$); $c_{p,v}$ the specific heat capacity of the vapor (J/kg-K); $T_v$ the temperature of the vapor phase (°C); $A_c$ the cross-sectional area of the test section tube, i.e., $\pi d^2/4$ (m$^2$); and $P_w$ the heated wall perimeter, i.e., $\pi d$ (m). In solving Eq. (5-8), $G_l$ is calculated by $G_l = (1-x)\,G$, where $G$ is the total mass flux, which is an input from the experiments, and $x$

is the flow quality. $x$ is calculated by $x = \frac{h_{mix} - h_l}{h_v - h_l}$, where $h_{mix}$ is the total enthalpy of the mixture of the steam and water, which can be obtained from the wall heat flux, mass flux and inlet subcooling. $h_v$ is the vapor enthalpy, which is based on the system pressure and vapor temperature. The local pressure can be obtained from the pressure transducer at the inlet and differential pressure transducer measurements across the test section assuming a linear pressure profile from the inlet to the outlet of the test section. The vapor temperature is assumed to be the mean value of the inner wall temperature and saturation temperature (based on the local pressure). The inner wall temperature is calculated from the measured outer wall temperature in the experiments based on the heat conduction in the test section. $h_l$ is the local average liquid water enthalpy, which is based on the pressure and liquid temperature. The local pressure in the liquid phase is the same as the local vapor pressure as explained earlier. $\Gamma''' = \frac{\mathrm{d}G_v}{\mathrm{d}z}$ is applied and the measured $q_w''$ from the experiments is used. $T_l$ is the only unknown parameter and can be solved by iteration. The liquid-side heat flux can be calculated by:

$$q_{li}'' = G_l c_{p,l} \frac{\mathrm{d}T_l}{\mathrm{d}z} \frac{A_c}{P_i} = q_w'' \frac{P_w}{P_i} - \left[ \Gamma''' \left( h_v - h_l \right) + G_v c_{p,v} \frac{\mathrm{d}T_v}{\mathrm{d}z} \right] \frac{A_c}{P_i}. \tag{5-9}$$

5.2.2 Results and discussion

Stewart's experimental data (Stewart, 1981) obtained under high pressure conditions, up to 9 MPa, are reduced to calculate the liquid-side Nusselt number in the IAFB regime. The parametric effects, including the wall heat flux, mass flux, inlet subcooling, and system pressure, on the liquid-side

Nusselt number in the IAFB regime are studied and the results are shown in Figure 5.1 to Figure 5.4. As the (computed) local liquid subcooling decreases, the interface between the liquid core and vapor film gradually becomes wavy and the liquid core becomes oscillatory, leading to a significant increase of the liquid-side heat transfer coefficient. From the analysis results presented in those figures, we can conclude that no significant effects of the wall heat flux, mass flux, inlet subcooling, and system pressure are observed on the predicted liquid-side Nusselt number in the IAFB regime. It should be noted however that the numerical values of the system pressure, mass flux, and inlet subcooling in Figure 5.1 to Figure 5.4 are nominal values.

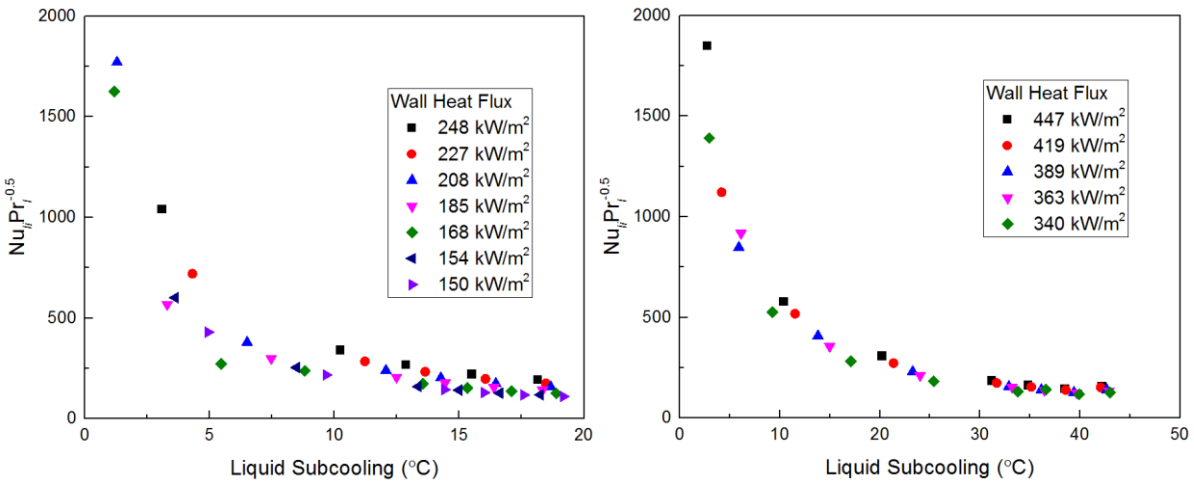


(a) (b)

Figure 5.1 Effects of the wall heat flux on the liquid-side Nusselt number in the IAFB regime under the flow conditions of (a) pressure of 2 MPa, mass flux of 923 kg/m$^2$-s, and inlet subcooling of 22 °C and (b) pressure of 8 MPa, mass flux of 923 kg/m$^2$-s, and inlet subcooling of 50 °C

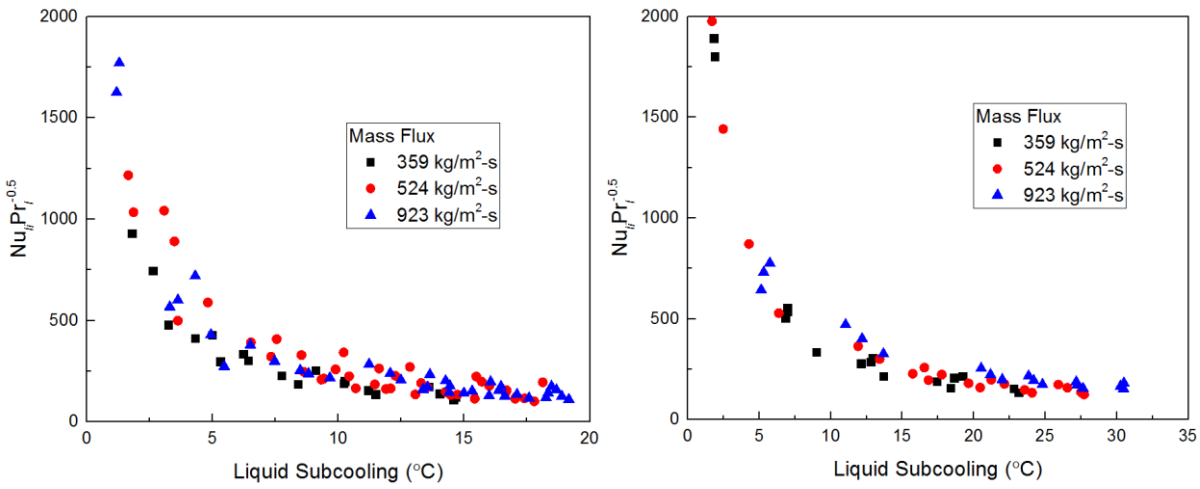


(a) (b)

Figure 5.2 Effects of the mass flux on the liquid-side Nusselt number in the IAFB regime under the flow conditions of (a) pressure of 2 MPa and inlet subcooling of 22 °C and (b) pressure of 6 MPa and inlet subcooling of 35 °C

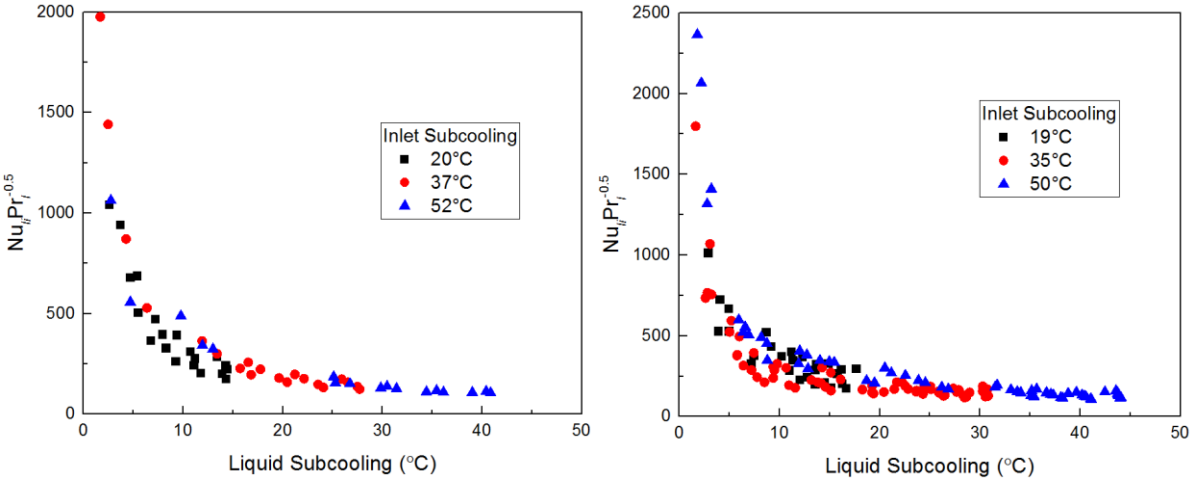


(a) (b)

Figure 5.3 Effects of the inlet subcooling on the liquid-side Nusselt number in the IAFB regime under the flow conditions of (a) pressure of 6 MPa and mass flux of 524 kg/m$^2$-s and (b) pressure of 8 MPa and mass flux of 923 kg/m$^2$-s

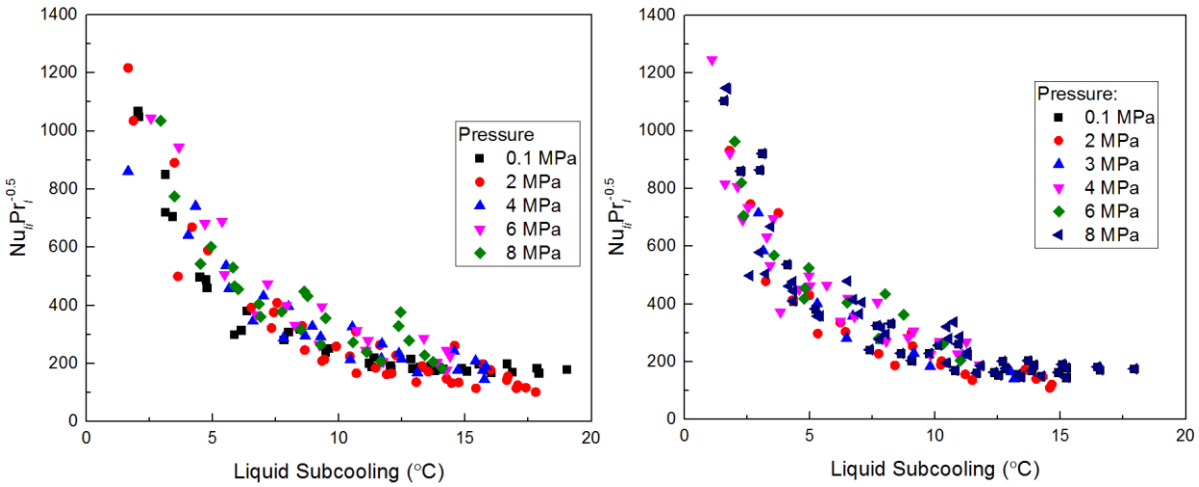


(a) (b)

Figure 5.4 Effects of the system pressure on the liquid-side Nusselt number in the IAFB regime under the flow conditions of (a) mass flux of 524 kg/m$^2$-s and inlet subcooling of about 20 °C and (b) mass flux of 359 kg/m$^2$-s and inlet subcooling of about 20 °C

Figure 5.5 shows the computed liquid-side Nusselt number vs. the computed local liquid subcooling based on Stewart's 838 experimental data points (Stewart, 1981). For the high local liquid subcooling conditions ($\Delta T_{sub} \geq\sim 20°C$), the interface between the liquid core and the vapor film is considered relatively smooth and the calculated value of $\mathrm{Nu}_{li}\,\mathrm{Pr}_l^{-0.5}$ is almost independent on the local liquid subcooling, approaching an asymptotic value of 144 with a sample standard deviation of 37 based on the 838 experimental data points, as:

$$\mathrm{Nu}_{li} = 144\sqrt{\mathrm{Pr}_l}\,, \tag{5-10}$$

where $\mathrm{Pr}_l$ is the liquid Prandtl number evaluated at the liquid local temperature. Equation (5-10) would only be applicable to the smooth IAFB regime, not the rough-wavy IAFB regime.

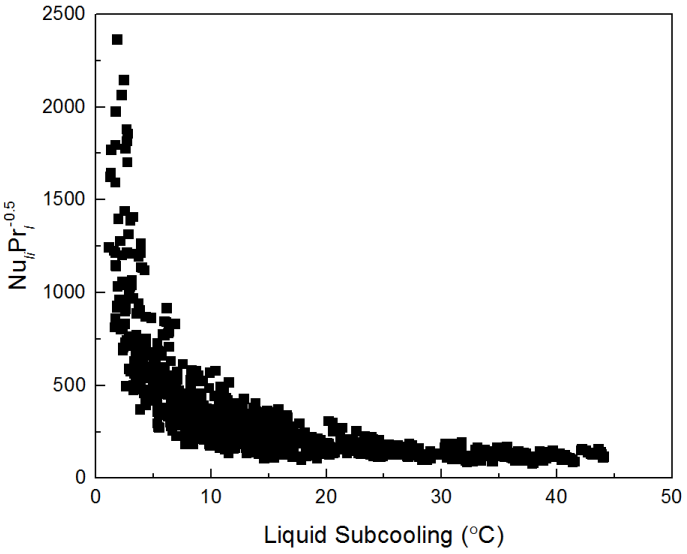


Figure 5.5 Computed liquid-side Nusselt number as a function of the computed local liquid subcooling

The computed liquid-side Nusselt is plotted as a function of the void fraction based on Fung's experimental data (Fung, 1981) as shown in Figure 5.6. When the void fraction is smaller than about 0.4, the value of $\mathrm{Nu}_{li}\,\mathrm{Pr}_l^{-0.5}$ remains to be fairly constant, which may correspond to the smooth IAFB regime. When the void fraction is between 0.4 and about 0.6, $\mathrm{Nu}_{li}\,\mathrm{Pr}_l^{-0.5}$ increases as the void fraction increases but the data points are considerably scattered. This regime may correspond to the rough-wavy IAFB regime. In this flow regime, the interface between the liquid core and the vapor film is no longer cylindrical, and wrinkles and waviness can be observed at the interface. The assumption of a cylindrical interface model again under-predicts the interfacial area concentration in the rough-wavy IAFB, thereby artificially over-predicts the value of $\mathrm{Nu}_{li}\,\mathrm{Pr}_l^{-0.5}$. When the void fraction is larger than 0.6, the flow regime may transition to the ISFB or even DFFB regime. The data points are significantly scattered as shown in Figure 5.6 and are incorrect since the IAFB model used in the DF-FB code is no longer valid when the void fraction is larger than

0.6. From the trend of the computed liquid-side Nusselt number with the void fraction, the flow regime transitions from the smooth IAFB to wavy-rough IAFB regimes and from the wavy-rough IAFB to ISFB regimes could occur at the void fraction of about 0.4 and 0.6, respectively.

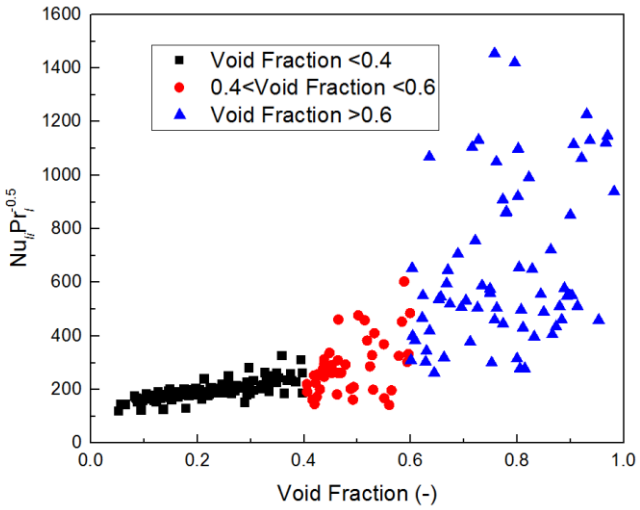


Figure 5.6 Liquid-side Nusselt number vs. the measured void fraction

## 5.3 Interfacial Friction

A laminar vapor film model for the interfacial friction factor is derived based on a laminar flow model for the vapor film in the IAFB regime. Experimental data obtained in the steady-state subcooled and low-quality film boiling experiments in the literature, specifically those by Fung (1981) and Savage et al. (1989), in which the void fraction was measured by a gamma densitometer, are reduced to calculate the interfacial friction factor by solving 1D two-fluid momentum equations. The dominant mechanisms contributing to the interfacial friction/shear are analyzed for the smooth and wavy IAFB regimes based on the experimental data. The laminar

vapor film model and nine existing correlations used in the IAFB regime are evaluated by the experimental data.

### 5.3.1 Laminar vapor film model

Heat transfer characteristics in IAFB have been studied by developing physical models based on the laminar flow assumption for the vapor phase (Fung and Groeneveld, 1982; Mosaad, 1988). In this section, a mathematical model for the interfacial friction factor is derived for the smooth IAFB regime, which is limited to laminar flow in the vapor film. The actual IAFB flow regime is quite complicated, so it is essential to simplify mathematic equations to obtain an analytic model. A schematic of the vapor film and liquid flow is shown in Figure 5.7. The mathematical model is based on the following assumptions besides the assumptions in Section 5.1:

(1) The vapor film flow is in fully developed laminar flow.

(2) The fluid thermophysical properties are constant.

(3) The vapor film thickness is small enough so that the vapor can be assumed to be between a flat wall and a flat vapor-liquid interface.

(4) The change of the vapor momentum is negligible. In the highly subcooled IAFB regime, most of heat is used to heat the liquid core to reduce the subcooling therefore the vapor generation rate is negligible (Kelly, 2015).

(5) The liquid velocity is assumed to be uniform in its flow cross section, i.e., the area-averaged liquid velocity.

(6) The vapor velocity at the interface is the same as the liquid velocity (no-slip at the interface).

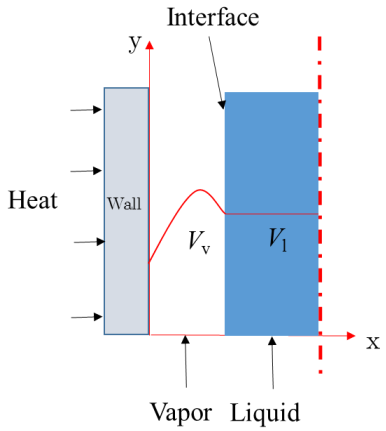


Figure 5.7. Schematic of the vapor film and liquid flow in the IAFB regime

Based on the above assumptions, the momentum equation in the vapor film is reduced as:

$$\mu_v\left(\frac{\mathrm{d}^2V_v}{\mathrm{d}x^2}\right)=\frac{\mathrm{d}p}{\mathrm{d}y}+\rho_v g\,. \tag{5-11}$$

where *p* is the pressure, Pa. The boundary conditions are as follows:

$$x=0, V_v=0$$
$$x=\delta, V_v=\bar{V}_l$$

By solving the momentum equation in the vapor film, i.e., Eq. (5-11), with the boundary conditions, the vapor velocity is obtained as:

$$V_v\ x\ =\frac{1}{2\mu_v}\left(\frac{\mathrm{d}p}{\mathrm{d}y}+\rho_v g\right)x^2+\frac{\mu_v V_l-\frac{1}{2}\left(\frac{\mathrm{d}p}{\mathrm{d}y}+\rho_v g\right)\delta^2}{\delta\mu_v}x\,. \tag{5-12}$$

The vapor velocity distribution is parabolic, but the location of the maximum vapor velocity is not at the location of $\delta/2$. In fact, it is closer to the vapor-liquid interface due to the nonzero liquid velocity as shown in Figure 5.7. The area-averaged vapor velocity, $\bar{V}_v$, over the cross section is calculated as:

$$\bar{V}_v = \frac{1}{\delta}\int_0^{\delta} V_v \ x \ \mathrm{d}x = -\frac{1}{12\mu_v}\left(\frac{\mathrm{d}p}{\mathrm{d}y} + \rho_v g\right)\delta^2 + \frac{\bar{V}_l}{2}. \tag{5-13}$$

According to the Newton's law of viscosity, the shear stress at the vapor-liquid interface can be determined as:

$$\tau_i = -\mu_v \frac{\mathrm{d}V_v}{\mathrm{d}x}\Big|_{\delta} = -\left[\frac{\mu_v V_l}{\delta} + \frac{1}{2}\left(\frac{\mathrm{d}p}{\mathrm{d}y} + \rho_v g\right)\delta\right]. \tag{5-14}$$

Substituting Eq. (5-10) into Eq. (5-11), one has:

$$\tau_i = \frac{2\mu_v}{\delta}\left(3\bar{V}_v - 2V_l\right). \tag{5-15}$$

In Ref. (Stewart, 1981), the slip ratio in the IAFB regime is $1.822\left(\frac{\rho_f}{\rho_g}\right)^{0.2}$. Therefore, it is reasonable to assume $\bar{V}_l/\bar{V}_v \approx 0$ at relativley low system pressure. Based on the definition of the interfacial friction factor in Eq. (1-16), we have:

$$f_{i,\mathrm{Laminar}} = \frac{4\mu_v}{\delta\rho_v}\frac{3\bar{V}_v - 2V_l}{\left(\bar{V}_v - V_l\right)^2} = \frac{24\mu_v}{\rho_v\left(\bar{V}_v - V_l\right)2\delta}\frac{1 - \frac{2}{3}V_l/\bar{V}_v}{1 - V_l/\bar{V}_v} \approx \frac{24}{\mathrm{Re}_v}, \tag{5-16}$$

which has the same form as the Fanning factor for single-phase flows between two parallel plates, but the characteristic velocity in the definition of the Reynolds number is different for these two cases. The characteristic velocity is the fluid mean velocity in the Reynolds number in single-phase flows while the relative velocity between the gas and liquid phases is used in the derived Laminar vapor film model for the IAFB regime. The interfacial friction factor for the smooth IAFB regime in our model shown in Eq. (5-16) is related to the gas Reynolds number in fully developed laminar flow.

5.3.2 Data reduction method

Fung (1981) and Savage et al. (1989) performed steady-state film boiling experiments with water as the working fluid under subcooled and low-quality conditions. In this section, a data reduction method to obtain the interfacial friction factor based on 1-D two-fluid momentum equations is described from the experimental data. The void fraction, wall temperature, inlet subcooling, and mass flow rate were measured in these experiments, which are the inputs to the data reduction procedure. The results obtained based on the experimental data will be compared with the laminar vapor film model and nine correlations from the literature in Section 5.4.3. The 1-D momentum equations for the vapor and liquid phases are shown in Eqs. (5-3) and (5-4). Eliminating the pressure gradient term yields:

$$(1-\alpha)\frac{\mathrm{d}}{\mathrm{d}z}(G_v V_v) - \alpha\frac{\mathrm{d}}{\mathrm{d}z}(G_l V_l) = \alpha(1-\alpha)\Delta\rho g - (1-\alpha)\frac{\tau_{wv} P_w}{A} - \frac{\tau_i P_i}{A} + \Gamma''' V_l . \quad (5\text{-}17)$$

Based on the definition of the interfacial friction factor in Eq. (1-16), the interfacial factor can be calculated by:

$$f_i = 2\left[\alpha\frac{\mathrm{d}(G_l V_l)}{\mathrm{d}z} - (1-\alpha)\frac{\mathrm{d}(G_v V_v)}{\mathrm{d}z} + \alpha(1-\alpha)\Delta\rho g - (1-\alpha)\frac{\tau_{wv} P_w}{A} + \Gamma''' V_l\right]\frac{A}{P_i \rho_v \left(V_v - V_l\right)^2}, \quad (5\text{-}18)$$

where $\Delta\rho$ is the density difference between the liquid and vapor, kg/m$^3$. The model for the wall drag force adopted in TRACE V5.0 (U.S. NRC, 2010) are used to solve Eq. (5-18). In solving Eq. (5-18), the vapor temperature, liquid temperature, vapor mass flux, and liquid mass flux are required to be calculated, which is described as follows.

The vapor temperature is assumed to be the arithmetic mean of the wall temperature and water saturation temperature in the current model. The subcooled liquid temperature is calculated from an energy balance using the liquid-side interfacial heat transfer rate by:

$$G_l c_{p,l} \frac{\mathrm{d}T_l}{\mathrm{d}z} = Nu_{li} \frac{4k_l}{D^2}\left(T_{sat} - T_l\right), \tag{5-19}$$

where $c_{p,l}$ is the specific heat capacity of the liquid, J/kg-K; $T_l$ the liquid core average temperature, °C; $k_l$ the thermal conductivity of the liquid water, W/m-K; $T_{sat}$ the liquid saturation temperature, °C; and $Nu_{li}$ the liquid-side Nusselt number at the liquid-vapor interface. The liquid-side Nusselt number is assumed to be constant value in the IAFB regime, i.e., 144. In the IAFB regime, the flow quality (thermal non-equilibrium quality) is calculated using:

$$x = \frac{h_{mix} - h_l}{h_v - h_l}, \tag{5-20}$$

where $x$ is the thermal non-equilibrium flow quality; $h_{mix}$ the mixture enthalpy, J/kg, which can be obtained from the wall heat flux, mass flux and inlet subcooling; $h_v$ the vapor enthalpy, which is based on the system pressure and vapor temperature. The local pressure can be obtained from the pressure transducer at the inlet and differential pressure transducer measurements across the test section assuming a linear pressure profile from the inlet to the outlet of the test section. The vapor temperature is assumed to be the mean value of the inner wall temperature and saturation temperature (based on the local pressure). $h_l$ the local average liquid water enthalpy, which is based on the pressure and liquid temperature. The local pressure in the liquid phase is the same as the local vapor pressure as explained earlier. $G_l$ is calculated by $G_l = \left(1 - x\right) G$, where $G$ is the total mass flux and obtained from the experimental data. $\Gamma''' = \frac{\mathrm{d}G_v}{\mathrm{d}z}$ is applied in Eq. (5-18).

### 5.3.3 Results and discussion

In this section, the interfacial friction factor calculated from the experimental data in literature (Fung, 1981; Savage et al. 1989) using Eq. (5-18) is discussed for the smooth and wavy IAFB regions. Figure 5.8 shows the relationship of the interfacial friction factor and the measured void fraction. As the void fraction increases, the interfacial friction factor decreases first and then increases, which indicates a possible flow regime transition from the smooth region to the wavy region. In the smooth IAFB regime, the vapor-liquid interface is smooth and has almost no waves as shown schematically in Figure 1.2. In this region, as the void fraction increases, the vapor Reynolds number increases, and the interfacial friction factor decreases. The trend is consistent with the laminar vapor film model derived in Section 5.4.1. The interfacial friction factor is primarily dependent on the Reynolds number, which is similar to that in laminar single-phase flows where the friction factor is dependent on the Reynolds number but not on the pipe roughness.

Above a critical void fraction value, significant interfacial waves start to be generated on the liquid-vapor interface due to the evaporation at the interface thus the increased relative velocity between the two phases, oscillations of the liquid core, and turbulence of the vapor phase, causing the interfacial friction factor to rise rapidly, where the flow transitions to wavy IAFB regime before the liquid-core breaks up. At even higher vapor velocities, liquid droplets are sheared off from interfacial wave and entrained by the vapor flow, which leads to an increase in the friction factor. In this region, the interfacial friction factor is significantly affected by the amplitudes of the interfacial waves, which is similar to that in the turbulent single-phase flows where the friction factor is affected by the pipe roughness. Figure 5.9 shows the interfacial friction factor and thermal

equilibrium quality. It can be seen that the regime transitions at the thermal equilibrium quality of -0.015 to -0.010, where the flow is still subcooled.

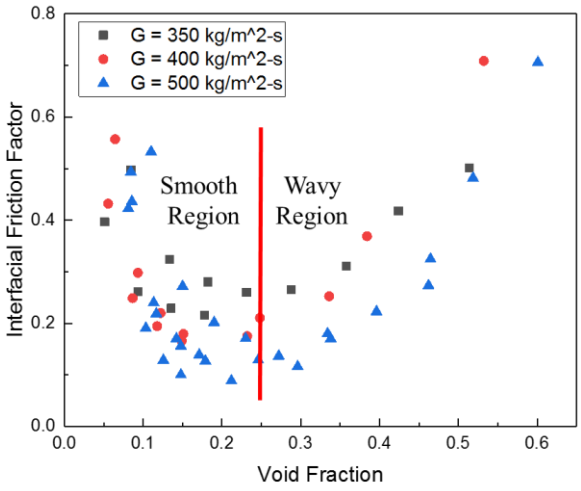


Figure 5.8 Interfacial friction factor calculated using Eq. (5-18) vs. the measured void fraction from Fung's experiments (Fung, 1981)

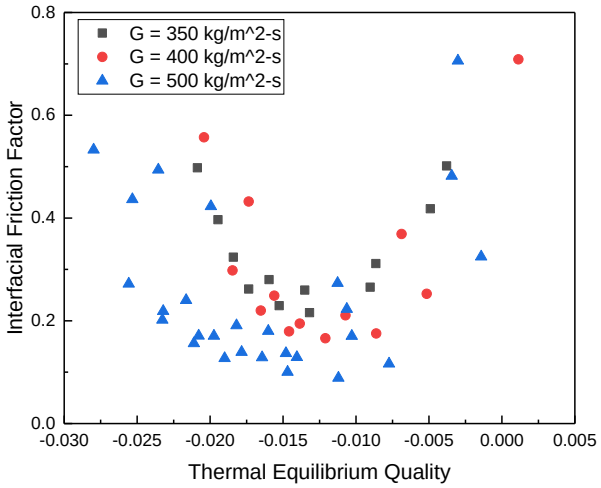


Figure 5.9 Interfacial friction factor and thermal equilibrium quality calculated from Fung's experiments (Fung, 1981)

Currently, there is no consensus on the transition criterion for the transition from the smooth to the wavy regions in the IAFB regime. Savage et al. (1992) suggested that the regime transition occurred at the void fraction of 0.15 to 0.35 in TRAC. Based on the study of the liquid-side heat transfer in Section 5.2, the regime transitions at the void fraction of about 0.4. In the current study, the interfacial friction factor implies the regime transitions from the smooth to the wavy regions at the void fraction of 0.2 to 0.4 as shown in Figure 5.10.

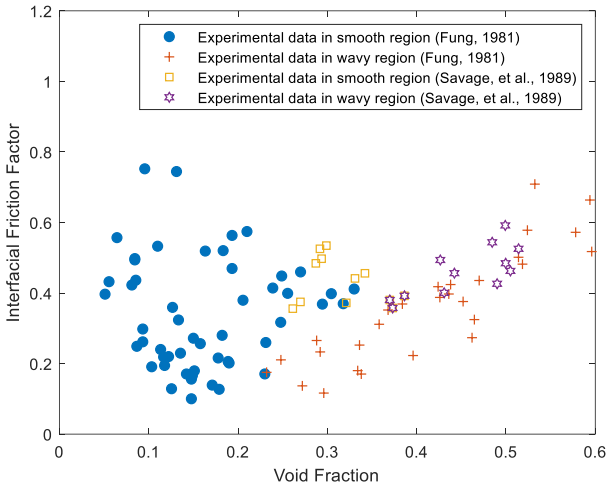


Figure 5.10 Void fraction and interfacial friction factor in smooth and way regions

The laminar vapor film model and nine correlations for the interfacial friction factor in Table 5.1, i.e., Wallis (1970), Moeck (1970), Fung and Groeneveld (1982), Analytis and Yadigaroglu (1987), Wang et al. (1988), Aritomi et al. (1990), Cachard (1996), TRACE (U.S. NRC, 2010), and CTF (Salko et al., 2017), are compared with the results calculated from the experimental data (Fung, 1981; Savage et al., 1989).

Table 5.1 Summary of interfacial friction factor correlations in the IAFB regime

| No. | Reference | Correlation |
|---|---|---|
| 1 | Wallis (1970) | $f_{\text{Wallis}} = 0.005\left(1 + 300\dfrac{\delta}{D}\right)$ |
| 2 | Moeck (1970) | $f_{\text{Moeck}} = 0.005\left[1 + 1458\left(\dfrac{\delta}{D}\right)^{1.42}\right]$ |
| 3 | Fung and Groeneveld (1982) | $f_{\text{Fung}} = 1.5 f_{\text{Wallis}}\left(e^{\frac{\phi}{2 f_{\text{Wallis}}}} - \dfrac{\phi}{f_{\text{Wallis}}}\right)$ |
| 4 | Analytis and Yadigaroglu (1987) | $f_{\text{Analytis}} = 0.085\,\text{Re}_v^{\,-0.25}\left(1 + 300\dfrac{\delta}{D}\right)$ |
| 5 | Wang et al. (1988) | $f_{\text{Wang}} = \dfrac{0.0791}{\text{Re}_i^{\,0.25}}\left(1 + 90.9\dfrac{\delta}{D_c}\right)$ |
| 6 | Aritomi et al. (1990) | $f_{\text{Aritomi}} = \dfrac{8.5}{\text{Re}_i^{\,0.25}}\dfrac{\delta}{D_c}$ |
| 7 | Salko et al. (2017) | $f_{\text{CTF}} = 0.025\left(1 + 300\dfrac{\delta}{D}\right)$ |
| 8 | Cachard (1996) | $f_{\text{Cachard}} = \lambda_{fv}\dfrac{24}{\text{Re}_v}$ |
| 9 | U.S. NRC (2010) | $f_{\text{TRACE}} = \sqrt{\left(\dfrac{144}{\delta^{*3}}\right)^2 + \left(0.35\left(\dfrac{\delta}{La}\right)^{0.72}\right)^2}$ |
| 10 | Laminar vapor film model (Eq. (25)) | $f_{i,\text{Laminar}} \approx \dfrac{24}{\text{Re}_v}$ |

Considering that Cachard's model (1996) is an improvement of the laminar vapor film model shown in Eq. (5-16), a comparison of the laminar vapor film model and Cachard's correlation (1996) with Fung's experimental data (1981) is first shown in Figure 5.8. The results predicted by the laminar vapor film model is smaller than the experimental data calculated by Eq. (5-18) but the trend of the results predicted by the laminar vapor film model matches with the experimental

data in the smooth region. The laminar vapor film model appears to be the lower bound of the interfacial friction factor in the smooth region. But in the wavy region, the laminar vapor film model performs poorly because the interfacial waves have a significant effect on the interfacial friction factor. The results predicted for the wavy region by the Cachard's correlation, which includes an enhancement parameter to improve the laminar vapor film model, has a similar trend to the experimental data but over-predicts. Both the laminar vapor film model and Cachard correlation have no indication of the regime transition from the smooth to the wavy regions.

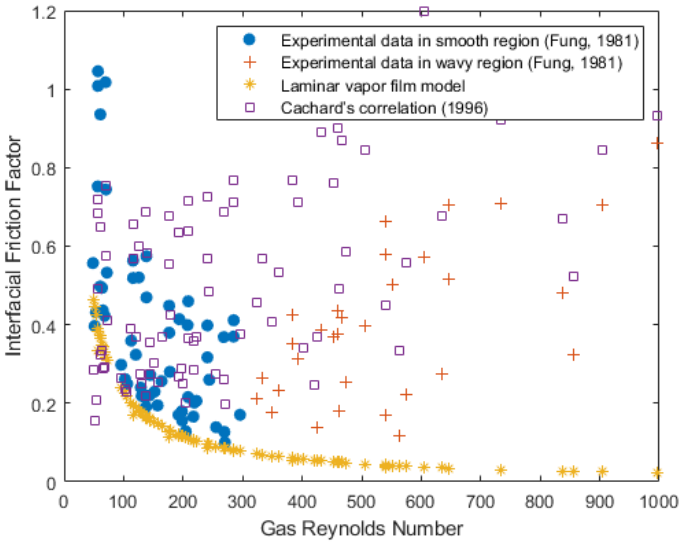


Figure 5.11 Comparison of the laminar vapor film model and Cachard's correlation (1996) with the results calculated from Fung's experimental data (Fung, 1981)

From Figure 5.11, it can be seen that the transition from the smooth to the wavy regions occur at the gas Reynolds number of about 300. Based on the interfacial friction model in TRACE (U.S. NRC, 2010), this transition occurs at the gas Reynolds number of about 350. In Hsu and Westwater's analysis (Hsu and Westwater, 1960), it was claimed that the vapor flow transitions from to turbulent flow at the gas Reynolds number of about 100. It should be noted that the

definitions of the Reynolds number in Hsu and Westwater's work and this study are different. In Hsu and Westwater's definition, the characteristic length is the vapor film thickness but twice of the vapor film thickness is used in the current definition. In addition, the vapor velocity is used as the characteristic velocity in Hsu and Westwater's paper but the relative velocity between the vapor and liquid phases is adopted in this study. It appears that the transition from the smooth to the wavy regions have some relationship with the transition from the laminar to the turbulent flow of the vapor phase. To further support this hypothesis, experimental data at the liquid-vapor interface and in the vapor phase are required.

Figure 5.12 shows comparisons of the correlations by Wallis (1970), Moeck (1970), Fung and Groeneveld (1982), Analytis and Yadigaroglu (1987), Wang et al. (1988), Aritomi et al. (1990), and CTF (Salko et al., 2017) with the experimental data (Fung, 1981; Savage et al., 1989) calculated by Eq. (5-18). All of these correlations are developed based on the interfacial waves and the trends of the correlations match well with the experimental data in the wavy region but not in smooth region, which is consistent with the assumption that the interfacial friction factor is related to the interfacial waves in the wavy region. The correlations by Wallis (1970), Fung and Groeneveld (1982), Wang et al. (1988), and Aritomi et al. (1990) under-predict the experimental data in the wavy region, while correlations in Analytis and Yadigaroglu (1987) and CTF (Salko et al., 2017) over-predicts the experimental data in the wavy region. Moeck's correlation (1970) matches well with the experimental data in the wavy region.

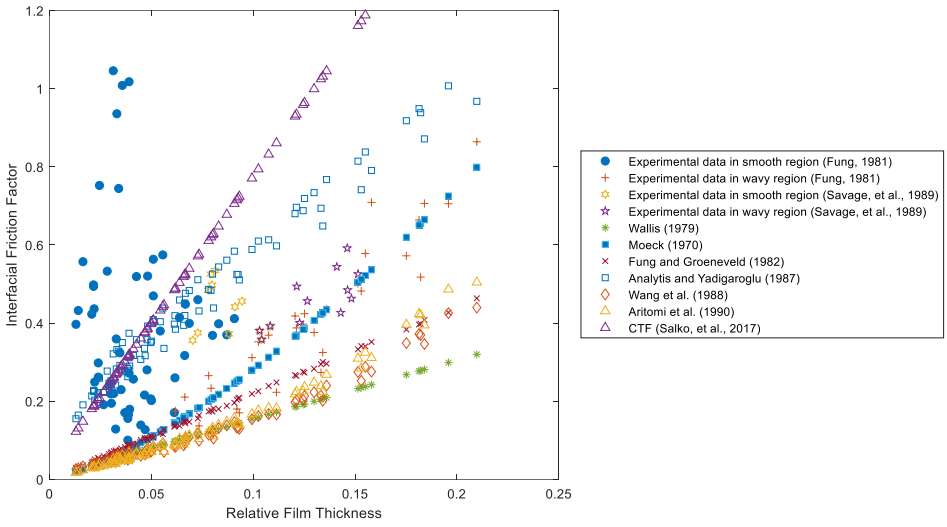


Figure 5.12. Comparison of the correlations of Wallis (1970), Moeck (1970), Fung and Groeneveld (1982), Analytis and Yadigaroglu (1987), Wang et al. (1988), Aritomi et al. (1990), and CTF (Salko et al., 2017) with the results calculated from experimental data (Fung, 1981; Savage et al., 1989)

Figure 5.13 shows a comparison of the correlation in TRACE V5.0 (U.S. NRC, 2010) with the experimental data. In TRACE V5.0, the correlation of the interfacial friction factor is a combination of two correlations, one is related to the gas Reynolds number and the other the relative film thickness. The trend of the results predicted by the correlation in TRACE matches with the experimental data and indicates a possible regime transition from the smooth to the wavy regions. However, the correlation under-predicts the experimental data in the wavy region.

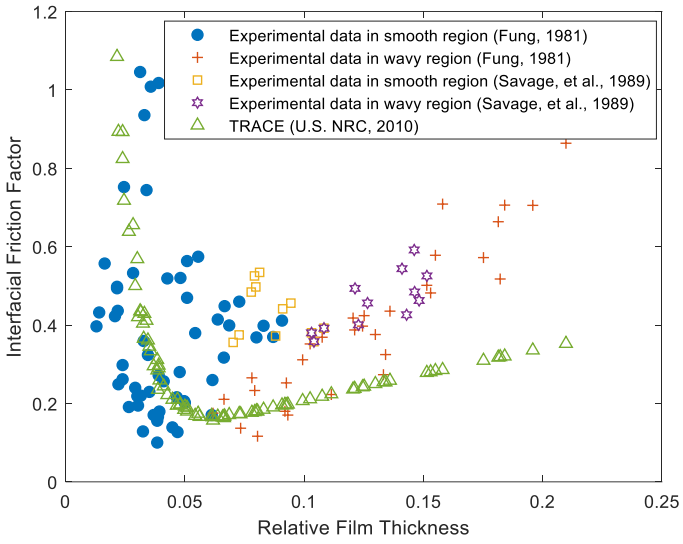


Figure 5.13 Comparison of the correlation in TRACE (2010) with the results calculated from experimental data (Fung, 1981; Savage et al., 1989)

Based on above evaluations, the trend of the results predicted by the laminar vapor film model (Eq. (5-16)) matches well with experimental data in the smooth region and the laminar vapor film model appears to be the lower bound of the interfacial friction factor in the smooth region. All of the correlations developed based on the interfacial waves can match well with the trend of the experimental data in the wavy region but not quantitatively. Moeck's correlation matches best with the experimental data in the wavy region and the correlation in TRACE can predict the trends of the interfacial friction factor in both the smooth and wavy regions. It can be concluded that the gas Reynolds number-based correlation is applicable to the smooth IAFB region and the relative vapor film thickness-based correlations is applicable to the wavy IAFB region. In the smooth region, the interface is relatively smooth and the interfacial friction is primarily controlled by the gas Reynolds number, while in the wavy region, the interfacial friction is significantly affected by the presence

of the interfacial waves, which play a more dominant role in affecting the interfacial friction than the gas Reynolds number.

To examine the experimental data further and capture the main mechanisms for the interfacial friction factor, the interfacial friction factor in the smooth IAFB region is correlated with $\mathrm{Re}_v\left(\frac{D_c}{2\delta}\right)$ and compared with the laminar vapor film model, i.e., Eq. (5-16), and Cachard correlation as shown in Figure 5.14. It can be seen that the interfacial friction factor in the smooth region reduced from Fung's data (1981) correlates well with $\mathrm{Re}_v\left(\frac{D_c}{2\delta}\right)$. The laminar vapor film model under-predicts and Cachard's correlation predicts well the interfacial friction factor in the smooth region. Comparing with the laminar vapor film model, Cachard's correlation added the effects of the interfacial disturbances and turbulence at the vapor-liquid interface on the interfacial friction factor, which indicates that the interfacial characteristics also affect interfacial friction factor in the smooth region besides the gas Reynolds number. Figure 5.15, a subset of Figure 5.12, shows the results calculated from the experimental data and Moeck's correlation in the wavy region. The Moeck's correlation matches well with the experimental data, which indicates that the interfacial friction factor in the wavy region is primarily dependent on the interfacial waves. Based on above analysis, Cachard's correlation and Moeck's correlation are recommended to be used in the smooth and wavy IAFB regions, respectively. To well apply the interfacial friction factor correlation in the IAFB modeling, physics-based flow transition criteria need to be further studied to predict the flow transition from the smooth to wavy IAFB regions.

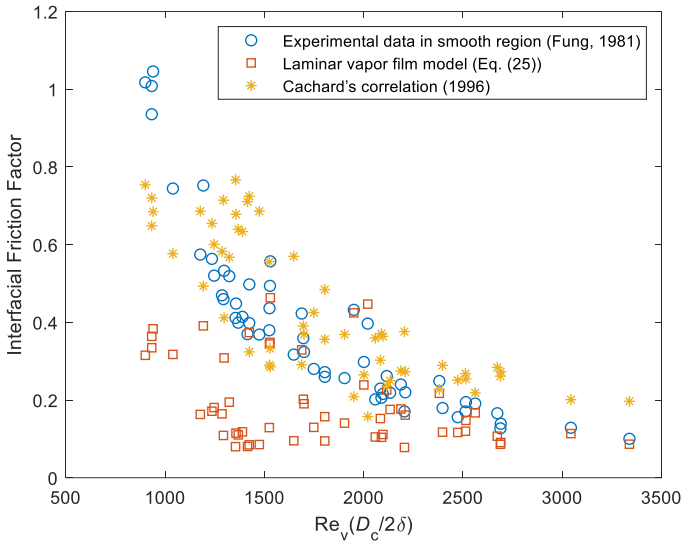


Figure 5.14. Results calculated from the experimental data in the smooth IAFB region (Fung, 1981)

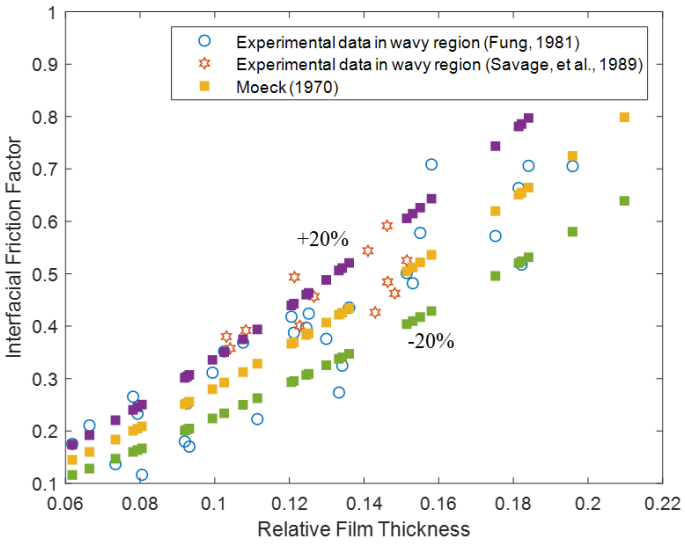


Figure 5.15. Results calculated from the experimental data in the wavy IAFB region (Fung, 1981; Savage et al., 1989) and Moeck's correlation (1970)

## 5.4 Flow Regime Transition

### 5.4.1 Data reduction

The breakup of the liquid-core represents the flow regime transition from IAFB to ISFB/AIAFB regimes, which can be predicted by the Weber number. The Weber number based on the vapor phase is calculated as:

$$\mathrm{We}_v = \frac{\rho_v \left(V_v - V_l\right)^2 D_c}{\sigma}, \tag{5-21}$$

where $\rho_v$ is the vapor density (kg/m$^3$); $V_v$ the vapor velocity (m/s); $V_l$ the liquid velocity (m/s); $D_c$ the liquid-core diameter (m); and $\sigma$ the surface tension (N/m$^2$). In the calculation, the vapor-liquid interface is assumed to be smooth. The liquid-core diameter, liquid velocity, and vapor velocity are calculated by a two-fluid film-boiling (TF-FB) code developed based on a 1-D two-fluid model in house.

Stewart (1981) performed steady-state film boiling experiments using indirectly heated hot patch technique in the vertical tubular test section with water from 2 to 9 MPa and obtained a database of the film boiling at the subcooled and low-quality conditions. The experimental data were reduced to calculate the Weber number to study the breakup of the liquid-core in the IAFB regime. Figure 5.16 shows the Weber number and thermal non-equilibrium calculated based on Stewart's experimental data (1981). It can be seen that the Weber number rises rapidly with distance from the inlet due to the increase of the vapor velocity and then drops. The reason for the decrease of the Weber number is that the IAFB regime is invalid after the breakup of the liquid-core and the

calculated Weber number is not accurate after the "red line" in Figure 5.16. The turning point shown by the "red line" in Figure 5.16 represents the value of the critical Weber number, i.e., $We_{v,cri}$, and the termination of the IAFB regime.

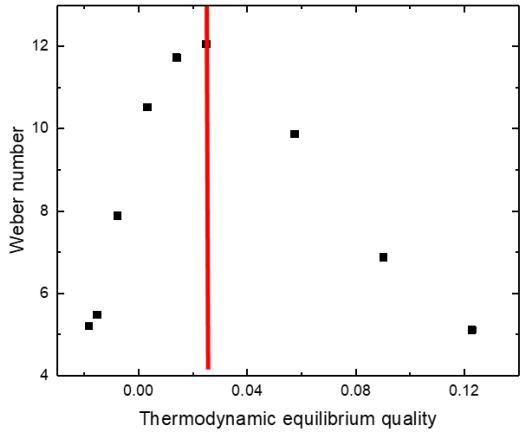


Figure 5.16 Weber number and thermodynamic equilibrium quality calculated based on Stewart's experimental data (1981) for $p$ = 2 MPa, $G$ = 215 kg/m$^2$-s, and $\Delta T_{sub,in}$ = 20 °C

5.4.2 Parametric effects

Figure 5.17 shows the effect of the mass flux on the values of the critical Weber number. It can be seen that for the same pressure and inlet subcooling, the value of the critical Weber number increases as the mass flux increases. Figure 5.18 shows the effect of the system pressure on the values of the critical Weber number. It can be seen that the value of the critical Weber number increases as the system pressure increases. Figure 5.19 shows the effect of the inlet subcooling on the values of the critical Weber number. It can be seen that the value of the critical Weber number decreases as the inlet subcooling increases. From a physical perspective, these three parameters,

mass flux, system pressure, and inlet subcooling, do have effects on the Weber number as defined in Eq. (5-21). The mass flux is related to the velocities in Eq. (5-21). The system pressure affects the ratio of the vapor and liquid density. The inlet subcooling affects the flow quality and further affects the velocities.

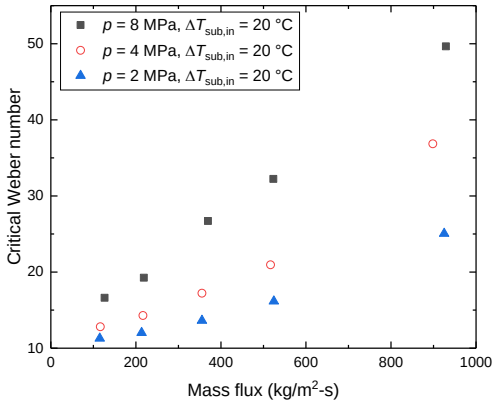


Figure 5.17 Effect of the mass flux on the values of the critical Weber number

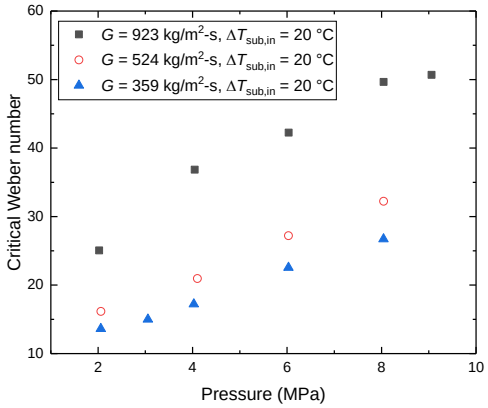


Figure 5.18 Effect of the system pressure on the values of the critical Weber number

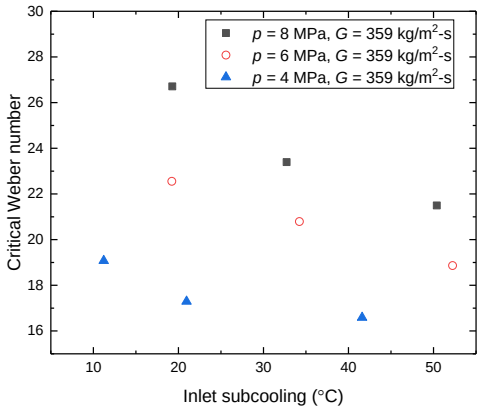


Figure 5.19 Effect of the inlet subcooling on the values of the critical Weber number

### 5.4.3 Model development

To validate, to some extent, the critical Weber number criterion, the wall heat transfer coefficients (based on the saturation temperature) in the post-CHF flow regimes are calculated to investigate the flow regime transition together with the critical Weber number in post-CHF flow regimes at subcooled and low-quality conditions. Figure 5.20 shows the profiles of the Weber number and the wall heat transfer coefficient for the mass fluxes of 359 and 120 kg/m$^2$-s and inlet subcooling of 20 ºC at the system pressure of 2 MPa. It can be seen that the maximum value of the heat transfer coefficient is corresponding to the maximum value of the Weber number, i.e., critical Weber number, indicating the flow regime transition from the IAFB to ISFB regime.

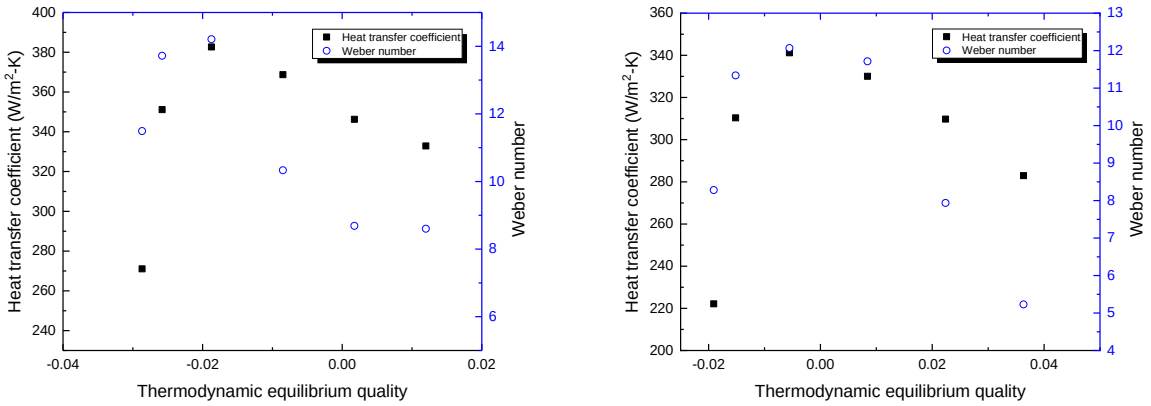


(a) $G = 359\,\mathrm{kg/m^2}$-s (b) $G = 215\,\mathrm{kg/m^2}$-s

Figure 5.20 Weber number and wall heat transfer coefficient for P =2 MPa and $\Delta T_{\mathrm{sub,in}} = 20^{\circ}\mathrm{C}$

The wall heat transfer characteristics in the post-CHF flow regimes at subcooled and low-quality conditions are a complex function of flow conditions (Stewart and Groeneveld, 1982). Due to the different flow patterns in the transition regime between IAFB and DFFB regimes, i.e., IAFB for low mass fluxes and AIAFB for high mass fluxes, the heat transfer coefficients have different trends. Figure 5.21 shows the heat transfer coefficients for different mass fluxes at the inlet subcooling of 20 ºC and system pressure of 2.0 MPa. It can be seen that the wall heat transfer coefficient decreases first and then increases for $G$ = 923 kg/m$^2$-s, but increases first and then decreases for $G \leq 524$ kg/m$^2$-s. In the IAFB regime, there are two opposite effects of the vapor on the wall heat transfer coefficient. As the vapor thickness increases, the thermal resistance due to the heat conduction mechanism across the vapor increases. However, high turbulence will be produced as the vapor velocity increases and the vapor-liquid interface becomes more agitated as the vapor thickness increases, which will enhance the convective heat transfer. The net effect of the vapor depends on the relative importance of these two effects on the heat transfer. For the high

mass flux, the flow quality is relatively small, and the vapor film is smooth and stable near the inlet of the test section. The heat conduction mechanism is dominant compared to the convective mechanism. Therefore, the wall heat transfer coefficient decreases as the thickness of the vapor film increases. After the liquid-core breaks up and the flow transitions to the AIAFB regime. In the AIAFB regime, the mass flux is high, and the breakup of the liquid-core can significantly increase the turbulence of the flow. Therefore, the wall heat transfer coefficients increase in the AIAFB regime. For the low mass flux, the flow quality is relatively high, and the vapor film may have some wavy configurations. The convective heat transfer mechanism is dominant compared to the heat conduction mechanism. As the void fraction increases, the wavy interface can produce significant turbulence and droplet entrainment, which can enhance the convective heat transfer. Therefore, as the flow quality increases, the heat transfer coefficient increases. After the liquid-core breaks up, the flow transitions to the ISFB regime. In the ISFB regime, the mass flux is relatively small. The increased void fraction reduces the wall heat transfer coefficient in the ISFB regime.

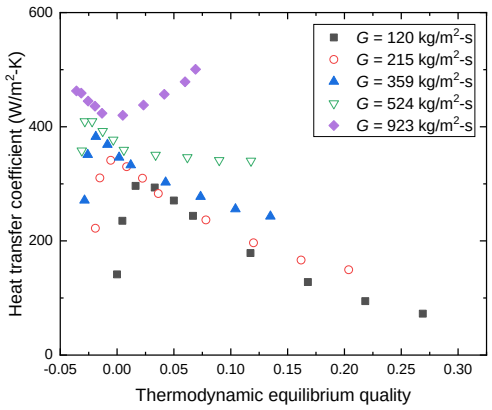


Figure 5.21 Heat transfer coefficient for different mass fluxes at the inlet subcooling of 20 ºC and system pressure of 2.0 MPa

From the above analysis, it can be seen that the heat transfer characteristics in the post-CHF regimes are complex for high and low mass fluxes due to different heat transfer mechanisms and transition regimes. Therefore, the discussion is split into two parts, i.e., high mass flux ($G$ = 923 kg/m$^2$-s) and low mass flux ($G \leq$ 524 kg/m$^2$-s). Based on the parametric study, the critical Weber number is related to the mass flux, system pressure, and inlet subcooling. Two non-dimensional parameters, i.e., Reynolds number and subcooling number, which are related to mass flux, system pressure, and inlet subcooling, are used in the model development for the critical Weber number. The experimental data are divided into two parts based on the mass flux, i.e., 1) mass flux of 120 to 524 kg/m$^2$-s and 2) mass flux of 923 kg/m$^2$-s. Figure 5.22 shows the critical Weber number for a pressure range of 2 to 9 MPa, mass flux range of 120 to 524 kg/m$^2$-s, and inlet subcooling range of 10 to 50 ºC. The critical Weber number is correlated to the Reynolds number (Based on the inlet flow condition) and subcooling number using the regression method.

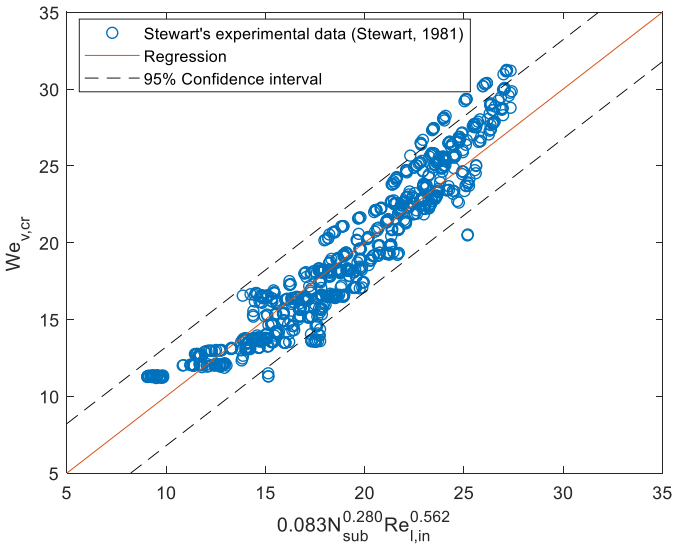


Figure 5.22 Critical Weber number for the pressure range of 2 to 9 MPa, mass flux range of 120 to 524 kg/m$^2$-s, and inlet subcooling range of 10 to 50 ºC

A correlation for the critical Weber number is proposed for the pressure range of 2 to 9 MPa, mass flux range of 120 to 524 kg/m$^2$-s, and inlet subcooling rang of 10 to 50 ºC as:

$$\mathrm{We}_{\mathrm{v,cr}} = \max\ \left[0.083\mathrm{N}_{sub}^{\ 0.280}\ \mathrm{Re}_{l,in}^{\ 0.562},\ 11\right], \tag{5-22}$$

$$\mathrm{Re}_{\mathrm{l,in}} = \frac{\rho_{l,in} V_{l,in} D}{\mu_{l,in}}, \tag{5-23}$$

$$N_{sub} = \frac{\dot{m} c_p \Delta T_{sub,in}}{q'' \pi D L}, \tag{5-24}$$

where $\mathrm{Re}_{l,in}$ is the liquid Reynolds number calculated based on the inlet flow condition; $\mathrm{N}_{sub}$ the subcooling number, $\rho_g$ the density of saturated vapor, kg/m$^3$; $\rho_f$ the density of saturated liquid, kg/m$^3$; $\rho_{l,in}$ the density of the liquid at the inlet of the test section, kg/m$^3$; $V_{l,in}$ the liquid velocity at the inlet of the test section, m/s; $\mu_{l,in}$ the liquid dynamic viscosity evaluated based on the inlet condition, kg/m-s; $D$ the hydraulic diameter of the test section, m; $\dot{m}$ the mass flow rate, kg/s; $c_p$ the specific heat capacity J/kg-K; $\Delta T_{sub,in}$ the inlet subcooling, ºC; $q''$ heat flux from wall to fluid, W/m$^2$; and $L$ the length of the heated section, m. In Figure 5.22, it can be seen that the trend of the critical Weber number becomes flat as the critical Weber number decreases to about 11. Therefore, a minimum value of 11 is applied to Eq. (5-22). Equation (5-22) is applicable to the flow conditions for the pressure range of 2.0 to 9.0 MPa, mass flux range of 120 to 524 kg/m$^2$-s, and inlet subcooling rang of 10 to 50 ºC. The correlation coefficient is 0.945 and 98% of the experimental data fall within the 95% confidence interval of the prediction.

To benchmark the proposed regime transition criterion, i.e., Eq. (5-22), the critical Weber number calculated based on Chen et al.'s experiment data (1989) is compared with Eq. (5-22) as shown in Figure 5.23. The predicted data fall within the ±20% error bands.

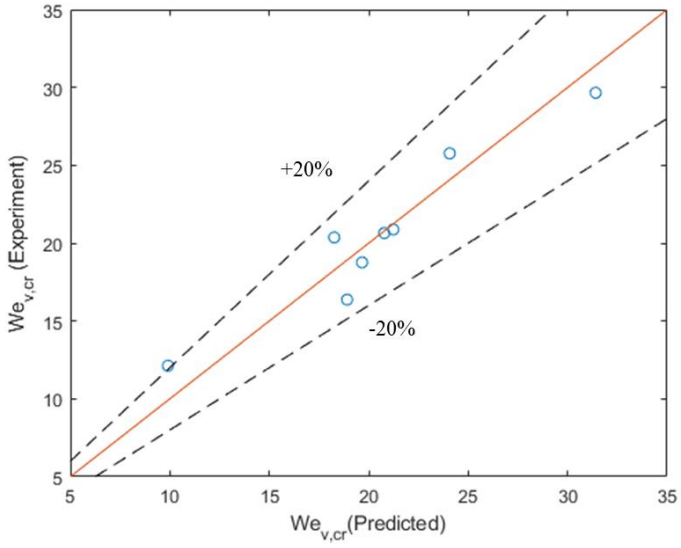


Figure 5.23 Comparison of the critical Weber number calculated based on Chen et al.'s experimental data (1989) with Eq. (5-22)

Figure 5.24 shows the critical Weber number for the pressure range of 2.0 to 9.0 MPa, mass flux of 923 kg/m$^2$-s, and inlet subcooling rang of 10 to 50 ºC calculated based on Stewart's experimental data (1981). It can be seen that the critical Weber number is well correlated with the Reynolds number and subcooling number. The correlation coefficient is 0.951. No model improvement is proposed for the mass flux of 923 kg/m$^2$-s since the data used only have one mass flux value.

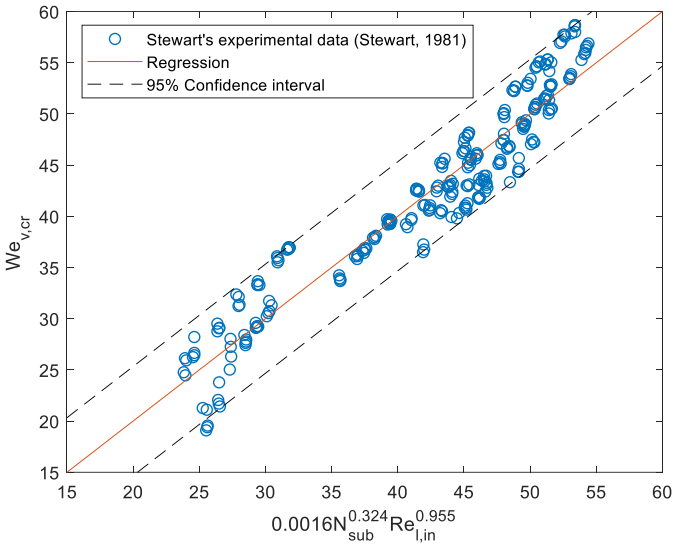


Figure 5.24 Critical Weber number for the pressure range of 2.0 to 9.0 MPa, mass flux of 923 kg/m$^2$-s, and inlet subcooling rang of 10 to 50 ºC

## 5.5 Void Fraction Prediction

To benchmark the closure models, a TF-FB code is developed based on the 1D two-fluid model to calculate the void fraction in the IAFB regime. Fung's experimental data (Fung 1981) are used to benchmark the TF-FB code. The accuracy of the void fraction measurements in Fung's experiments was reported to vary from 3 to 6% (in absolute void fraction value) depending on whether the void fraction measured is near the upper (100%) or lower (0%) end values in Fung's experiments. Figure 5.25 shows the comparisons of the experimental data with the predicted void fractions by the TF-FB code. The error bars on the measured void fractions represent ±6% absolute (not relative) void fraction. The average relative difference between the predicted void fractions using the new correlation is less than 20%. In Figure 5.25, the calculated void fraction values approach an asymptotic value, about 0.9, near the end of the test section tube, which appears to be

smaller than the measured values. With the void fraction being larger than about 0.9, the flow would have transitioned to the DFFB regime, where the physics and phenomena are significantly different from those in the IAFB regime. Therefore, the TF-FB code is only applicable when the void fraction is less than about 60% or even lower (only smooth IAFB regime).

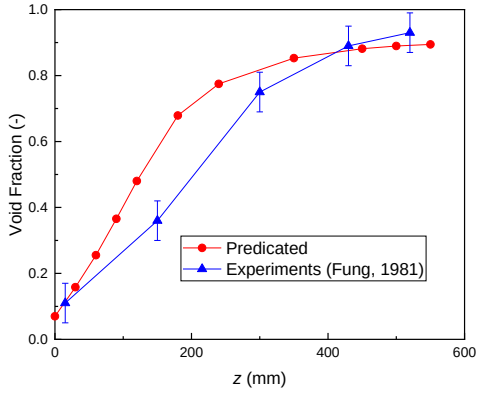


(a) $G$ = 400 kg/m$^2$-s and $\Delta T_{sub,in}$ = 20 ºC

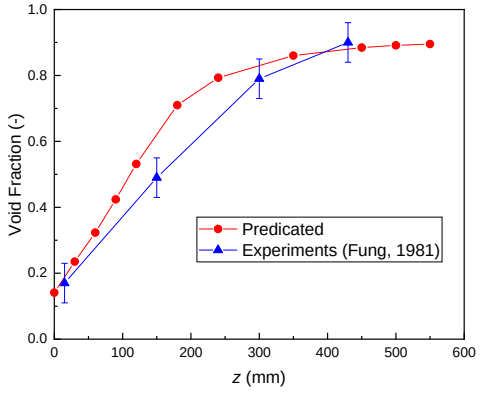


(b) $G$ = 300 kg/m$^2$-s and $\Delta T_{sub,in}$ = 10 ºC

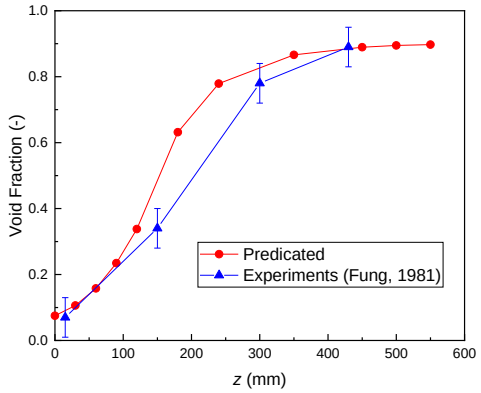


(c) $G$ = 200 kg/m$^2$-s and $\Delta T_{sub,in}$ = 20 ºC

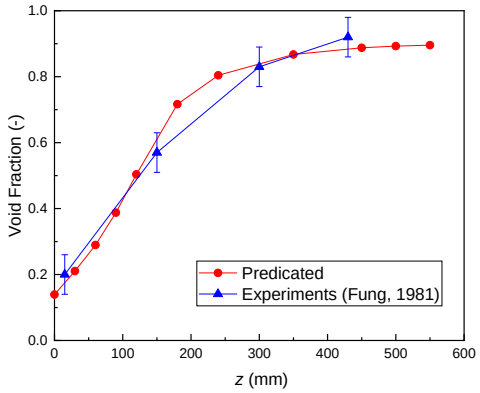


(d) $G$ = 200 kg/m$^2$-s and $\Delta T_{sub,in}$ = 10 ºC

Figure 5.25 Comparisons of the experimental and predicted void fractions by the TF-FB code

# Chapter 6 Conclusions and Future Work

## 6.1 Summary and Conclusions

This research presents a number of original contributions to the field. The PCHT test facility with its unique test capabilities brings many benefits to the community and can assist in further nuclear reactor safety improvement. The improved post-CHF closure models could be used in reactor system analysis to improve the IAFB modeling. The summaries and major conclusions are listed as follows:

(1) A PCHT test facility is designed and constructed with a tubular test section for high-pressure, high-flow, and high inlet subcooling conditions (up to 6.8 MPa pressure, 2,000 kg/m$^2$-s mass flux, and 50 ºC inlet subcooling). Hydrostatic leak tests are performed, up to 1,000 psig at the room temperature, per the ASME code to ensure the reliability and leak tightness of the test facility. Subcooled boiling tests are performed to test the gamma densitometer and X-ray radiography system, which will be used for the void fraction and flow topology measurements in the post-CHF flow regimes.

(2) Reflooding tests are performed in this test facility to study the heat transfer characteristics during the quenching process. During the quenching process, the heat release from the test section plays a significant role in the total heat flux to fluid. Based on the profile of the convective heat

transfer coefficient, the flow regime transition from IAFB to DFFB regimes can be observed downstream of the quench front.

(3) Dry patch experiments are performed in the PCHT test facility to study the wall heat transfer characteristics during the process of formation, growth, and collapse of dry patches. The computed convective heat transfer coefficients in the stable film boiling region from the current experiment data are larger than the calculated results from Bromley's correlation (1950), Berenson's correlation (1961), and the corresponding correlation in CTF (Salko et al., 2017) at relatively low wall superheats, which indicates that the motion of the dry patch will enhance the heat transfer.

(4) The liquid-side Nusselt number is strongly dependent on the local liquid subcooling, but with little dependence on the wall heat flux, mass flux, inlet subcooling, and system pressure. A correlation for the liquid-side interfacial Nusselt number is developed for the IAFB regime.

(5) The laminar vapor film model derived based on laminar vapor flow assumption and nine existing correlations for interfacial friction factor are evaluated by the results calculated from the experimental data. Cachard's correlation matches best with the results in the smooth region and Moeck's correlation matches best with the results in the wavy region. The results calculated from the experimental data suggest that the interfacial friction factor in the smooth region is primarily dependent on the gas Reynold number and the vapor film thickness and that it in the wavy region is dominantly affected by the presence of the interfacial waves.

(6) Based on the trend of the Weber number, the critical Weber number is obtained to predict the breakup of the liquid core in the IAFB regime, i.e., the flow regime transition from IAFB to ISFB/AIAFB regimes. A parametric study discovers that the critical Weber number is dependent on the mass flux, system pressure, and inlet subcooling. A correlation for the critical Weber number is proposed for low mass fluxes as a function of two non-dimensional parameters, i.e., the Reynolds number and subcooling number.

In this research, many contributions have been obtained for post-CHF heat transfer experiments and modeling. The reflooding and dry patch tests provide important data for film boiling modeling that is essential for thermal applications such as LOCAs in LWRs. The PCHT test facility will assist in further nuclear reactor safety improvement. The improved post-CHF closure models including liquid-side Nusselt number, interfacial friction factor, and flow regime transition criteria could be used in reactor system analysis to improve the IAFB modeling.

## 6.2 Future Work

In the PCHT test facility, steady-state film boiling experiments, including IAFB, ISFB, and DFFB tests, will be performed to measure the wall temperature, void fraction, liquid/vapor temperature, and flow topology to form a database covering wide flow and pressure ranges and further benchmark and improve the closure models in these flow regimes. The future work for the IAFB experiments and modeling is proposed as follows:

(1) Steady-state IAFB experiments need to be performed to fill the gap of the existing database especially at high-pressure and high-flow conditions and provide a complete database including the wall temperature, void fraction, liquid/vapor temperature, and flow topology.

(2) The interfacial characteristics in the IAFB regime are important for the interfacial heat and mass transfer. The flow topology in the IAFB regime, such as the interfacial waves, need to be measured and incorporated into the closure models to account for the enhancement effects on the heat and mass transfer.

(3) The liquid core temperature in the IAFB regime need be measured to further benchmark the liquid-side interfacial heat transfer models and the flow information at the liquid core breakup location in the IAFB regime will be used to benchmark and improve the flow regime transition criteria from IAFB to ISFB/AIAFB regimes. Physics-based flow transition criteria from the smooth to wavy IAFB regions need to be developed.

(4) Currently, all the wall heat transfer models are developed based on the fluid saturation temperature in the IAFB regime. If the bulk vapor temperature can be measured or evaluated with qualified uncertainties, the wall heat transfer model can be developed based on the bulk vapor temperature instead of saturation temperature, which can provide deep insights into the wall heat transfer characteristics in the IAFB regime.

(5) Considering the complication of post-CHF heat transfer and hydrodynamic characteristics, physics-based data-driven model can be developed using machining learning methods to study the heat transfer and flow regime transition in the post-CHF flow regimes.

## Bibliography


Adams R., Petrov, V., Manera, A., "Advanced high-resolution radiation-based measurement techniques for detailed void-fraction measurements in fuel bundles and high-pressure test sections", Proc. of the 17th Int. Topical Mtg. on Nuclear Reactor Thermal Hydraulics (NURETH-17), Xi'an, China, Sep 3 – Sept 9, 2017.

American Society of Mechanical Engineers, "Power Piping Code, ASME, B31.1," New York, 2007.

American Society of Mechanical Engineers, "Boiler and Pressure Vessel Code, ASME, Section II, Part D: Properties," New York, 2010.

Analytis, G.T. and Yadigaroglu, G., "Analytical modeling of inverted annular film boiling," Nuclear Engineering and Design, 99, 201-212, 1987.

Andritsos, N. and Hanratty, T.J., "Influence of interfacial waves in stratified gas-liquid flows," AIChE journal, 33(3), 444-454, 1987.

Aritomi, M., Inoue, A., Aoki, S., and Hanawa, K., "Thermo-hydraulic behavior of inverted annular flow," Nuclear Engineering and Design, 120(2-3), 281-291, 1990.

Arrieta L. and Yadigaroglu, G. "Analytical model for bottom reflooding heat transfer in light water reactors (the UCFLOOD code)," EPRI-NP-756, 1978.

Babelli, I., Revankar, S.T., and Ishii, M., "Flow visualization study of post-critical heat flux in inverted flow," Nuclear Engineering and Design, 146(1-3), 15-24, 1994.

Barnea, Y., Elias, E., and Shai, I., "Flow and heat transfer regimes during quenching of hot surfaces," International Journal of Heat and Mass Transfer, 37(10), 1441-1453, 1994.

Berenson, P.J., "Film boiling heat transfer from a horizontal surface," Journal of Heat Transfer, 83(3), 351-356, 1961.

Bromley, L.A., "Heat transfer in stable film boiling," Chemical Engineering Progress, 46(5), 221-228, 1950.

Bromley, L.A., LeRoy, N.R., and Robbers, J.A., "Heat transfer in forced convection film boiling," Industrial & Engineering Chemistry, 45(12), 2639-2646, 1953.

Cachard, F., “Development, implementation, and assessment of specific closure laws for inverted-annular film-boiling in a two-fluid model,” NUREG/IA-0133, Nuclear Regulatory Commission, Washington, DC, USA, 1996.

Cadek, F.F., Dominicis, D.P., and Leyse, R.H., “PWR FLECHT: (Full length emergency cooling heat transfer). Final Report, No. WCAP-7665. Westinghouse Electric Corp., Pittsburgh, Pa. Nuclear Energy Systems Div. Idaho Nuclear Corp., Idaho Falls, 1971.

Chen, Y., “Experimental study of inverted annular flow film boiling heat transfer of water,” In: Wang, B.-X. (Ed.), Heat Transfer Science and Technology. Hemisphere Pub. Co., pp. 627–634, 1987.

Chen, Y., Fu, X., and Chen, S., “Experimental and analytical study of inverted annular film boiling of water,” In: Shah, R.K. et al. (Eds.), Experimental Heat Transfer Fluid Mechanics and Thermodynamics. Elsevier Sci. Publ., 1438–1443, 1988.

Chen Y. and Li, J., “Subcooled flow film boiling of water at atmospheric pressure,” in Two-phase Flow and Heat Transfer, X. J. Chen and T. N. Veziroglu, Hemisphere Pub. Co., ISBN 0-89116-432-4, 141-150, 1984.

Chen, Y., Cheng, P., Wang, J., and Yang, M., “Experimental studies of subcooled and low quality of film boiling heat transfer of water in vertical tubes at moderate pressure,” Proc. 4th Int. Topical Meeting on Nuclear Reactor Thermal-Hydraulics, Vol. 2, 1106-1110, 1989.

Chen, Y., Wang, J., Yang, M., and Fu, X., “Experimental measurement of the minimum film boiling temperature of flowing water,” Multiphase flow and heat transfer. In: 2nd Int. Symposium 1, pp. 393–400, 1989.

Chen, Y., Xu, H., and Chen, H., “Experimental results of steady-state film boiling of forced flow water,” 2nd Research Coordinated Meeting of IAEA, CRP on Thermalhydraulic Relationships for AWCR, Vienna, 1996.

Chen, Y., Yang, C., Zhao, M., Bi, K., Du, K., and Zhang, S., “Subcooled boiling critical heat flux of water flowing upward in a tube for lower flow and pressure up to 20 MPa,” The 14th International Topical Meeting on Nuclear Reactor Thermal hydraulics (NURETH-14), Hilton Toronto Hotel, Toronto, Ontario, Canada, September 25-29, 2011.

Costigan, G., Ralph, J.C., and Wade, C.D., “Steady state heat transfer measurements relevant to reactor reflood conditions, Part 1: upflow,” UKAEA report, AERE-R12561, 1987.

Dittus, F.W. and Boelter, L.M.K., “Heat transfer in automobile radiators of the tubular type,” Int. Comm. Heat Mass Transfer 12, 3-12, 1985.

Dougall, R.S., “Film boiling on the inside of vertical tubes with upward flow of the fluid at low qualities,” Ph.D. Thesis, Massachusetts Institute of Technology, Cambridge, Massachusetts, United States, 1963.

Denham, M.K., “Inverted annular film boiling and the bromley model,” Safety and Engineering Science Division, AEE Winfrith, Report No. AEEW-R 1590, 1983.

El Nakla, M., Groeneveld, D.C., and Cheng, S.C., “Experimental study of inverted annular film boiling in a vertical tube cooled by R-134a,” International Journal of Multiphase Flow, 37(1), 67-75, 2011.

Edelman, Z., Elias, E., and Naot, D., “Inverted annular boiling in a stainless-steel tube with steady heat sources,” International Journal of Heat and Mass Transfer, 28(7), 1281-1292, 1985.

Forslund R.P. and Rohsenow, W.M., “Thermal non-equilibrium in dispersed flow film boiling in a vertical tube,” Department of Mechanical Engineering, Massachusetts Institute of Technology, Report No. 75312-44, 1966.

Forslund R.P. and Rohsenow, W.M., “Dispersed flow film boiling,” Journal of Heat Transfer, 90(4), 399-407, 1968.

Fung, K.K., “Subcooled and low quality film boiling of water in vertical flow at atmospheric pressure,” Ph.D. Thesis, University of Ottawa, Ottawa, Ontario, Canada, 1981.

Fung, K.K. and Groeneveld, D.C., “A physical model of subcooled and low quality film boiling of water in vertical flow at atmospheric pressure,” International Heat Transfer Conference 7, 6-10 September, Munich, Germany, pp. 381-386, 1982.

Goodman, J. and Elias, E., “Heat transfer in the inverted annular flow regime during reflooding,” Transaction of American Nuclear Society, 28, 397-399, 1978.

Groeneveld, D.C., “Effect of a heat flux spike on the downstream dryout behavior,” Journal of Heat Transfe, 96(2), 121-125, 1974.

Groeneveld, D.C., “Post-dryout heat transfer: physical mechanisms and a survey of prediction methods,” Nuclear Engineering and Design, 32(3), 283-294, 1975.

Groeneveld, D.C., “A review of inverted annular and low quality film boiling,” In Post-Dryout Heat Transfer, pp. 327-348, CRC Press, Inc., Boca Raton, Florida, 1992.

Groeneveld, D.C. and Gardiner, S.R.M., “A method of obtaining flow film boiling data for subcooled water,” International Journal of Heat and Mass Transfer, 21(5), 664-665, 1978.

Groeneveld, D.C., Leung, L.K.H., Guo, Y.J., and Cheng, S.C., “A Look-up table for fully developed film-boiling heat transfer,” Nuclear Engineering and Design, 225(1), 83-97, 2003.

Groeneveld, D.C., Leung, L.K.H., Kirillov, P. L., Bobkov, V.P., Smogalev, I.P., Vinogradov, V.N., Huang, X.C., and Royer, E., "The 1995 look-up table for critical heat flux in tubes," Nuclear Engineering and Design, 163(1), 1-23, 1996.

Groeneveld, D.C., Shan, J., Vasić, A.Z., Leung, L.K.H., Durmayaz, A., Yang, J., Cheng, S.C., and Tanase, A., "The 2006 CHF look-up table," Nuclear Engineering and Design, 237(15), 1909-1922, 2007.

Gunnerson, F. S. and Yackle, T.R., "Quenching and rewetting of nuclear fuel rods," Nuclear Technology, 54(1), 113-117, 1981.

Hammouda, N., Groeneveld, D.C., and Cheng, S.C., "An experimental study of subcooled film boiling of refrigerants in vertical up-flow," International Journal of Heat and Mass Transfer, 39(18), 3799-3812, 1996.

Hammouda, N., Groeneveld, D.C., and Cheng, S.C., "Two-fluid modelling of inverted annular film boiling," International Journal of Heat and Mass Transfer, 40(11), 2655-2670, 1997.

Hill W.S. and Rohsenow, W.M., "Dryout droplet distribution and dispersed flow film boiling," Department of Mechanical Engineering, Massachusetts Institute of Technology, Report No. 85694-105, 1982.

Hinze, J.O., "Fundamentals of the hydrodynamic mechanism of splitting in dispersion processes," AIChE Journal, 1(3), 289-295, 1955.

Hochreiter, L.E., Cheung, F.B., Lin, T.F., Ergun, S., Sridharan, A., Ireland, A., and Rosal, E.R., "RBHT reflood heat transfer experiments data and analysis," NUREG/CR-6980, 2012.

Holman, J.P., "Heat transfer," Sixth Edition, McGraw-Hill Book Inc., New York, 1986.

Howard, P.A., Linehan, J.H., and Grolmes, M.A., "Experimental study of the stationary boiling front in liquid film cooling of a vertical heated rod," In 15th National Heat Transfer Conference, Paper No. CSChE/CSME-75-HT-14, San Francisco, CA, 1975.

Hsu, Y.Y. and Westwater, J.W., "Approximate theory for film boiling on vertical surfaces," Chemical Engineering Progress Symposium Series, 56(30), 15-24, 1960.

Hynek, S.J., Rohsenow, W.M., and Bergles, A.E., "Forced-convection dispersed-flow film boiling," Department of Mechanical Engineering, Massachusetts Institute of Technology, Report No. DSR 70586-63, 1969.

Ishii, M. and Denten, J.P., "Two-phase flow characteristic of inverted bubbly, slug and annular flow in post-critical heat flux region," Nuclear Engineering and Design, 121(3), 349-366, 1990.

Ishii, M. and Jarlais, G.De, "Flow regime transition and interfacial characteristics of inverted annular flow," Nuclear Engineering and Design, 95, 171-184, 1986.

Ishii, M. and Jarlais, G.De, "Flow visualization study of inverted annular flow of post dryout heat transfer region," Nuclear Engineering and Design, 99, 187-199, 1987.

Jarlais, G.De, Ishii, M., and Linehan, J., "Hydrodynamic stability of inverted annular flow in an adiabatic simulation," Journal of Heat Transfer, 108(1), 84–92, 1986.

Kaufman, J.M., "Post critical heat flux heat transfer to water in a vertical tube," M.S. Thesis, Massachusetts Institute of Technology, Cambridge, Massachusetts, United States, 1976.

Kelly, J., "Liquid-side interfacial heat transfer in inverted annular film boiling," NURETH-16, Chicago, IL, August 30-September 4, 2015.

Kelly, J., "Post-CHF heat transfer at high pressure and flow conditions: Experimental support for TRACE model development, Attachment #2: Hot patch design study," Task Order #3, the U.S. Nuclear Regulatory Commission, 2015.

Keplinger, O., Shevchenko, N., and Eckert, S., "Validation of X-ray radiography for characterization of gas bubbles in liquid metals," In IOP Conference Series: Materials Science and Engineering, 228, 012009, 2017.

Laperriere, A., "An Analytical and experimental investigation of forced convective film boiling," M.S. Thesis, University of Ottawa, Ottawa, Ontario, Canada, 1983.

Laverty, W.F. and Rohsenow, W.M., "Film boiling of saturated nitrogen flowing in a vertical tube," Journal of Heat Transfer, 89(1), 90-98, 1967.

Meduri, P.K., "Wall heat flux partitioning during subcooled flow film boiling of water on a vertical surface," Ph.D. Thesis, University of California, Los Angeles, California, United States, 2007.

Moeck, E.O., "Annular-dispersed two-phase flow and critical heat flux," Ph.D. Thesis, McGill University, Montreal, Canada, 1970.

Mohanta, L., Riley, M.P., Cheung, F.B., Bajorek, S.M., Kelly, J.M., Tien, K., and Hoxie, C.L., "Experimental investigation of inverted annular film boiling in a rod bundle during reflood transient," Nuclear Technology, 190(3), 301-312, 2015.

Moose R.A. and Ganić, E.N., "On the calculation of wall temperatures in the post dryout heat transfer region," International Journal of Multiphase Flow, 8(5), 525-542, 1982.

Mosaad, M., "Subcooled film boiling heat transfer to flowing water in a vertical tube," Ph.D. Thesis, Technische Universitat Berlin, Berlin, Germany, 1988.

Mosaad, M. and Johannsen, K., "Experimental study of steady-state film boiling heat transfer of subcooled water flowing upwards in a vertical tube," Experimental Thermal and Fluid Science, 2(4), 477-493, 1989.

Obot, N.T. and Ishii, M., “Two-phase flow regime transition criteria in post-dryout region based on flow visualization experiments,” International Journal of Heat and Mass Transfer, 31(12), 2559-2570, 1988.

Ottosen, P., “An experimental and theoretical investigation of inverse annular film flow and dispersed droplet flow important under LOCA conditions,” Riso National Lab, Denmark, Report No. 424, 1982.

Salko, R., Wysocki, A., Avramova, M., Toptan, A., Porter, N., Blyth, T., Dances, C., Gomez, A., Jernigan, C., and Kelly, J., “CTF theory manual,” The North Carolina State University, Raleigh, NC, USA, 2017.

Savage, R.A., Archer, D., and Swinnerton, D., “Heat transfer and voidage measurements in steady state post-dryout at low quality and high pressure,” IChemE 3rd UK National Heat Transfer Conference, Birmingham, UK. 1, 607-615, 1992.

Savage, R.A., Archer, D., and Swinnerton, D., “Flow visualization, heat transfer, and voidage measurements in steady-state post-dryout at high pressure,” Proc. 6th Int. Topical Meeting on Nuclear Reactor Thermal-Hydraulics, 2, 1311-1318, 1993.

Savage, R.A., Swinnerton, D., and Pearson, K.G., “Heat transfer and voidage measurements in steady state post-dryout at low quality and meduim pressure,” UKAEA Report AEEW-R2486, 1989.

Sawan, M. E. and Carbon, M.W., “A review of spray-cooling and bottom-flooding work for LWR cores,” Nuclear Engineering and Design, 32(2), 191-207, 1975.

Smith, T.A., “Heat transfer and carryover of low pressure water in a heated vertical tube,” M.S. Thesis, Massachusetts Institute of Technology, Cambridge, Massachusetts, United States, 1976.

Spore, J.W., Giles, M.M., and Shumway, R.W., “Best estimate radiation heat transfer model developed for TRAC-BD1”, No. CONF-810804--20, EG&G Idaho, Inc., 1981.

Stewart, J.C., “Low quality film boiling at intermediate and elevated pressures,” M.S. Thesis, University of Ottawa, Ottawa, Ontario, Canada, 1981.

Stewart, J. C. and Groeneveld, D.C., “Low-quality and subcooled film boiling of water at elevated pressures,” Nuclear Engineering and Design, 67(2), 259-272., 1982.

Sudo, Y., “Film boiling heat transfer during reflood phase in postulated PWR loss-of-coolant accident,” Journal of Nuclear Science and Technology, 17(7), 516-530, 1980.

Swinnerton, D., Hood, M. L., and Pearson, K. G. “Steady state post-dryout experiments at low quality and medium pressure data report,” UKAEA Report AEEW-R2267, 1988.

Swinnerton, D., Pearson, K.G., and Hood, M.L., "Steady state post-dryout experiments at low quality and medium pressure," UKAEA Report AEEW-R2192, 1988.

Takenaka, N., Fujii, T., Akagawa, K., and Nishida, K., "Flow pattern transition and heat transfer of inverted annular flow," International Journal of Multiphase Flow. 15(5), 767-785, 1989.

Takenaka, N., Akagawa, K., Fujii, T., and Nishida, K., "Experimental study on flow pattern and heat transfer of inverted annular flow," Nuclear Engineering and Design, 120(2-3), 293-300, 1990.

Thurgood, M.J., Kelly, J.M., Guidotti, T.E., Kohrt, R.J., and Crowell, K.R., "COBRA/TRAC-A thermal-hydraulic code for transient analysis of nuclear reactor vessels and primary coolant systems," Pacific Northwest Laboratory, NUREG/CR-3046, Nuclear Regulatory Commission, Washington, DC, USA, 1983.

U.S. NRC, "TRACE V5.0 theory manual-field equations, solution methods, and physical models," US. Nuclear Regulatory Commission, Washington, DC, USA, 2010.

Vijaykumar, R. and Dhir, V.K., "An experimental study of subcooled film boiling on a vertical surface—hydrodynamic aspects," Journal of Heat Transfer, 114, 161-168, 1992.

Vijaykumar, R. and Dhir, V.K., "An experimental study of subcooled film boiling on a vertical surface—thermal aspects," Journal of Heat Transfer, 114, 169-178, 1992.

Wallis, G.B., "Annular two-phase flow—Part 1: A simple theory," Journal of Basic Engineering, 92(1), 59-72, 1970.

Wang, B. and Shi D., "A semi-empirical theory for forced-flow turbulent film boiling of subcooled liquid along a horizontal plate," International Journal of Heat and Mass Transfer, 28(8), 1499-1505, 1985.

Wang, K., Watanabe, T., and Hirano, M., "Analysis of inverted annular film boiling by the MINCS code using two-fluid model," Japan Atomic Energy Research Institute, JAERI-M-88-174, 1988.

Westwater, J.W. and Santangelo, J.G., "Photographic study of boiling," Industrial and Engineering Chemistry, 47(8), 1605-1610, 1955.

Yu, K.P., "An experimental investigation of the reflooding of a bare tubular test section," Ph.D. Thesis, University of California, Berkeley, California, United States, 1978.